



Electron transport in molecular junctions

Jin, Chengjun

Publication date:
2015

[Link back to DTU Orbit](#)

Citation (APA):
Jin, C. (2015). *Electron transport in molecular junctions*. Technical University of Denmark.

General rights

Copyright and moral rights for the publications made accessible in the public portal are retained by the authors and/or other copyright owners and it is a condition of accessing publications that users recognise and abide by the legal requirements associated with these rights.

- Users may download and print one copy of any publication from the public portal for the purpose of private study or research.
- You may not further distribute the material or use it for any profit-making activity or commercial gain
- You may freely distribute the URL identifying the publication in the public portal

If you believe that this document breaches copyright please contact us providing details, and we will remove access to the work immediately and investigate your claim.

Ph.D. Thesis

Electron transport in molecular junctions

Chengjun Jin

Supervisor: Kristian Sommer Thygesen

Center for Atomic-scale Materials Design, Department of Physics
Technical University of Denmark

May 2015

Preface

This thesis is submitted in candidacy for the Ph.D. degree from the Technical University of Denmark (DTU). It is based on the work carried out at the Center for Atomic-scale Materials Design (CAMd), Department of Physics at DTU from February 2012 to May 2015 under the supervision of Professor Kristian S. Thygesen. Financial support was provided by DTU.

Firstly, I would like to thank Kristian for giving me the opportunity to conduct my PhD in Denmark. During the last three years, his supervision is always efficient and effective. His insight and passion on physics details influence my thinking in science as well as life. It's really lucky for me to be his student.

Secondly, I would like to thank: Troels Markussen for the inspiring discussion on the transport theory; Mikkel Strange for his endless help on the GW transport code; Gemma C. Solomon for her hospitality during my external stay in the University of Copenhagen; Walther Schwarzacher and Richard J. Brooke from the University of Bristol for the nice collaboration on the work of molecular gating; Filip A. Rasmussen for the nice collaboration on the work of MoS₂/Gr contacts.

Thirdly, I would like to thank all the members in CAMd for providing such high standard research atmosphere. It is amazing that you can always find the answer to your question just a few walks away; Especially to Marianne Ærsøe for the supportive administration; Marcin Dulak and Ole H. Nielsen for the smooth computing support. Jens J. Mortensen for the effective helps on GPAW; Christopher Patrick and Simone Latini for the fruitful discussion on this thesis; Kristian B. Ørnsø for the generous help of the Danish abstract.

Additionally, I enjoy the fun during the lunch and coffee break with Christopher Patrick, Filip A. Rasmussen, Kirsten Andersen, Korina Kuhar, Manuel Šaric, Martin H. Hansen, Mohnish Pandey, Morten N. Gjerding, Niels B. Halck, Simone Latini.

Last but not least, I thank my parents, my wife Qian and my son Mingze for their support and understanding.

Lyngby, May 30, 2015
Chengjun Jin

Abstract

This thesis addresses the electron transport in molecular junctions, focusing on the energy level alignment and correlation effects. Various levels of theory have been applied to study the structural and electronic effects in different molecular junctions, starting from the single particle density functional theory (DFT) description over the semi-empirical DFT+ Σ , to the sophisticated fully self-consistent GW approach. We find that in order to obtain a quantitative description of the conductance and the thermopower, it is necessary to go beyond the single particle description.

The effect of side groups on the benzene-diamine (BDA) molecule has furthermore been studied and it is found that the correct energy level alignment for the BDA molecule in Au contacts is only captured by the GW approach. Consequently, the GW approach provides an accurate description for the conductance change resulting from the side groups. The failure of the DFT based description is due to the strong energy level pinning when the BDA molecule is in contact with Au contacts.

The effect of contact geometries on the conductance and the thermopower has also been addressed. It is found that both GW and the DFT+ Σ with a certain image charge position are in quantitative agreement with the experiments, while pure DFT is not. This is the consequence of the accurate energy level alignment, where the DFT+ Σ method corrects the self-interaction error in the standard DFT functional and uses a static image charge model to include the image charge effect on the energy level renormalization.

Additionally, the gating of the 4,4'-bipyridine (44BP) molecule contacted to either Ni or Au electrodes has been investigated. Here it is found that the

gating mechanism is conceptually different between two cases. In the case of Ni contacts where the lowest unoccupied molecular level (LUMO) of the 44BP molecule hybridizes strongly with Ni $3d$ orbitals, the gating is auxiliary by the so-called *spinterface*.

Finally, the correlation effect of the image charge beyond the energy level renormalization has been studied. It is shown that the finite response time of the electrodes to form image charge can suppress the conductance by a factor of 2. This correlation effect is only captured in the GW approach.

Resumé

Denne afhandling omhandler elektrontransport i molekulære kontakter, med fokus på energiniveauplaceringer og korrelationseffekter. Forskellige niveauer af teori er anvendt til at studere de strukturelle og elektroniske effekter i forskellige molekulære kontakter, fra enkeltpartikeltæthedsfunktionalteori (DFT) over den semi-empiriske $DFT+\Sigma$ metode, til den sofistikerede fuldt selvkonsistente GW metode. Konklusionen er her at det er nødvendigt at bruge den sofistikerede GW metode for at få en korrekt kvantitativ beskrivelse af ledningsevnen.

En undersøgelse af effekten af forskellige sidegrupper på benzen-diamin (BDA) molekylet viser yderligere at den korrekte energiniveauplacering i BDA-molekylet mellem Au kontakter kun opnås ved brug af GW metoden. Som følge af dette giver GW metoden derfor også en nøjagtig beskrivelse af ledningsevneforandringerne forårsaget af udbytningen af sidegrupper. Den DFT-baserede metode fejler her grundet den stærke påvirkning af energiniveauer når molekylet interagerer med guldkontakterne.

Effekten af kontakternes geometrier på ledningsevnen er yderligere blevet undersøgt. Her giver både GW metoden og $DFT+\Sigma$ metoden, med en given position for imagecharge planet, resultater i overensstemmelse med eksperimentielle data, mens den rene DFT metode fejler. Dette skyldes den præcise energiniveauplacering beregnet med $DFT+\Sigma$ metoden, som korrigerer selvinteraktionsproblemet i ordinær DFT og yderligere bruger en statisk imagecharge model til at inkludere imagechargeeffekterne i energiniveaurenemliseringen.

Herudover er gating af 4,4'-bipyridin (44BP) molekylet med Ni og Au kontakter også blevet undersøgt. Her vises det, at gatingmekanismen er fundamentalt forskellig mellem Ni kontakter og Au kontakter. I Ni kontakterne, hvor

det laveste ubesatte molekylære niveau (LUMO) i 44BP molekyle hybridiserer kraftigt med Ni $3d$ orbitalerne, er gatingen påvirket af det såkaldte *spinterface*.

Slutteligt er korrelationseffekterne på baggrund af imagechargeeffekten blevet undersøgt gående videre end blot effekten på energiniveauplaceringen. Her vises det at den endelige responstid af elektroderne for dannelse af imagecharges kan reducere ledningsevnen med en faktor 2. Denne korrelationseffekt er kun fanget ved brug af GW metoden.

List of Included Papers

Paper I

Energy level alignment and quantum conductance of functionalized metal-molecule junctions: Density functional theory versus GW calculations

C. Jin, M. Strange, T. Markussen, G. C. Solomon, K. S. Thygesen
The Journal of Chemical Physics **139**, 184307 (2013)

Paper II

Quantitatively accurate calculations of conductance and thermopower of molecular junctions

T. Markussen, C. Jin, K. S. Thygesen
Physica Status Solidi (b) **250**, 2394 (2013)

Paper III

Single-molecule electrochemical transistor utilizing a nickel-pyridyl spinterface

R. J. Brooke, C. Jin, D. Szumski, R. J. Nichols, B. Mao, K. S. Thygesen, W. Schwarzacher
Nano Letters **15**, 275 (2015)

Paper IV

Dynamical image-charge effect in molecular tunnel junctions: Beyond energy level alignment

C. Jin, K. S. Thygesen
Physical Review B **89**, 041102(R) (2014)

Paper V

Simultaneous description of conductance and thermopower in single-molecule junctions from many-body ab initio calculations

C. Jin, T. Markussen, K. S. Thygesen
Physical Review B **90**, 075115 (2014)

Contents

Preface	i
Abstract	iii
Resumé	v
List of Included Papers	vii
1 Introduction	1
2 Density functional theory	3
2.1 Born-Oppenheimer approximation	4
2.2 Hohenberg-Kohn theorem and Kohn-Sham formalism	4
2.3 Exchange-correlation functional	5
2.4 Projector-augmented wave method	6
2.5 Basis sets	6
2.6 Boundary conditions	7
3 Electron transport calculations	9
3.1 Transport setup	10
3.2 NEGF+DFT	11
3.3 NEGF+GW	12
3.4 DFT+ Σ	13
3.5 Conductance and thermopower	15
4 Energy level alignment	17
4.1 Functionalization of the benzene-diamine molecule	18
4.1.1 Motivation	18
4.1.2 Results and discussion	18

4.2	The effect of contact variation on conductance and thermopower	24
4.2.1	Motivation	24
4.2.2	Results and discussion	25
4.3	Electrochemical gating of nonredox molecules	29
4.3.1	Motivation	29
4.3.2	Results and discussion	30
5	Beyond energy level alignment	35
5.1	Dynamical image charge effect	36
5.1.1	Motivation	36
5.1.2	Results and discussion	36
5.2	Simultaneous description of conductance and thermopower . . .	41
5.2.1	Motivation	41
5.2.2	Results and discussion	41
	Bibliography	49
	Appendix A	59

Introduction

In 1965, the Moore's law[1] predicts that the number of transistors on an electronic circuit will double every two years. The transistor miniaturization leads to lower cost, lower power consumption and higher performance. In the conventional semiconductor technology, the transistor is fabricated by a top-down fashion, which limits the size of an transistor. Currently the size of an transistor is around 10 nm (around 50 atoms)[2]. To further benefit from the Moore's law, a bottom-up approach could potentially solve the problem[3]. In such scenario, an atomic-scale channel material (a few atoms) is required.

Since the molecular rectifier was proposed by *Arieh Aviram* and *Mark Ratner* in 1974[4], the field of the so-called *molecular electronics* booms. Benefiting from the large number of existing molecules (roughly 10^{60} for organic compounds with 15 atoms or fewer[5]), single molecular electronics could realize rich functionalities, for instance organic solar cell and thermoelectrics. Additionally a single molecule connected to two metals helps us to understand the electron transfer at the molecule-metal interface[6] and the electron transport across the molecule[7, 8]. Furthermore, the discrete molecule energy levels coupled to continuous metal levels form ideal model systems to explore the Kondo effect[9, 10], the quantum interference[11, 12, 13] and the giant magnetoresistance[14].

Break junction setups are typically used to fabricate two-terminal single molecular junctions, possibly with a gate. Specifically, a single molecule is caught

when breaking electrodes. During the past 40 years, many progresses have been made towards reproducible conductance measurements of single molecular junctions[15, 16, 17]. Recently, many single molecule experiments go beyond the conductance measurements[18]: mechanics[19, 20], optoelectronics[21, 22], thermoelectrics[23, 24, 25], spintronics and quantum interference[26, 13]. However breaking junction experiments present measurement variability because of the molecule-metal contact sensitivity at the atomic scale and the timescale mismatch between the instruments and molecular processes. Well-controlled experimental setup is needed to make realistic molecular junction applications.

In addition to technology challenges, a theoretical approach is needed to understand the quantum transport in these atomic scale systems. Clearly we need a fully quantum mechanical approach to describe such quantum systems. In this thesis, the non-equilibrium Green's function formalism (NEGF) combined with either density function theory (DFT) or many-body theory is applied to study the electron transport in molecular junctions. The focus of the thesis is on the energy level alignment and dynamical image charge effects.

The thesis is organized as:

Chapter 2 describes the basics of DFT and its practical implementation.

Chapter 3 illustrates the principle of electron transport calculations using the NEGF formalism and different approaches to include the electron-electron correlation.

Chapter 4 studies the effect of the energy level alignment on the electronic conductance and the thermopower in different molecular junctions.

Chapter 5 explores the dynamical image charge effect beyond the energy level alignment using model and *ab initio* calculations, and its effect on the conductance and thermopower.

Density functional theory

To understand the physical properties of a many-body system from atoms to molecules, then to solids, we need to solve the Schrödinger equation:

$$H\Psi = E\Psi, \quad (2.1)$$

where H , E , Ψ denote the Hamiltonian, the total energy and the many-body wave function of the system. The Hamiltonian H is composed of the nuclei kinetic energy T_n , the nucleus-nucleus interaction V_{nn} , the electrons kinetic energy T_e , the electron-electron interaction V_{ee} and the electron-nucleus interaction V_{en} , namely

$$\begin{aligned} H &= T_n + V_{nn} + T_e + V_{ee} + V_{en} \\ &= - \sum_I^{N_n} \frac{\nabla_I^2}{2M_I} + \frac{1}{2} \sum_{I \neq J}^{N_n} \frac{Z_I Z_J}{|\mathbf{R}_I - \mathbf{R}_J|} \\ &\quad - \sum_i^{N_e} \frac{\nabla_i^2}{2} + \frac{1}{2} \sum_{i \neq j}^N \frac{1}{|\mathbf{r}_i - \mathbf{r}_j|} - \sum_{i,I}^{N_e, N_n} \frac{Z_I}{|\mathbf{R}_I - \mathbf{r}_i|}, \end{aligned} \quad (2.2)$$

where \mathbf{r} , \mathbf{R} , N_e , N_n , M , Z denote the electronic coordinate, the nuclear coordinate, the number of nuclei, the number of electrons, the nuclear mass and the nuclear charge.

In this chapter, density functional theory (DFT) will be introduced to solve the many-body problem of Eq. 2.1.

2.1 Born-Oppenheimer approximation

As nuclei are much heavier than electrons, we can assume that electrons react to nuclear motions instantaneously. By applying the Born-Oppenheimer approximation[27], we can decouple the electronic and nuclear degree of freedom. While nuclear motions are practically treated using Newtonian dynamics, we will focus on the electronic problem in the following thesis:

$$H_e = T_e + V_{ee} + V_{en}. \quad (2.3)$$

However due to the electron-electron interaction V_{ee} , the $3N_e$ -dimension many-body wave function makes Eq. 2.3 hardly tractable. Only a few systems have analytic solutions. Therefore we have to get around the many-body wave function.

The many-body wave function contains all the information about the quantum system. However you can extract the information you need by working with *integrated* variables rather than this $3N_e$ -dimension many-body wave function. In this thesis, the *electron density* and the *Green's function* are used to meet different demands[28]. The electron density approach is introduced in this chapter, namely DFT. The Green's function approach will be introduced in the next chapter, with the combination of the electron transport setup.

2.2 Hohenberg-Kohn theorem and Kohn-Sham formalism

Instead of solving a problem of $3N_e$ degrees of freedom, we can convert the problem to 3 degrees of freedom, namely Ψ to $\rho(\mathbf{r})$, according to the Hohenberg-Kohn (HK) theorem[29]. It states that firstly the electronic density uniquely determines the external potential of the system, which means the total energy is the functional of the density $E[\rho(\mathbf{r})]$; secondly ground state energy E_0 is smaller or equal to $E[\rho(\mathbf{r})]$, which allows the existence of a variational principle to minimize the total energy.

The HK theorem only tells us the relation between electron density and total energy. We still do not know the explicit form of the Hamiltonian. The remain-

ing problem can be further approximated according to the Kohn-Sham (KS) formalism[30]:

$$\left(-\frac{\nabla^2}{2} + \int d\mathbf{r}' \frac{\rho(\mathbf{r}')}{|\mathbf{r} - \mathbf{r}'|} + V_{ext}(\mathbf{r}) + V_{xc}(\rho(\mathbf{r}))\right) \psi_n(\mathbf{r}) = \epsilon_n \psi_n(\mathbf{r}). \quad (2.4)$$

The central ideal of the KS formalism is to map the system of interacting electrons onto a non-interacting system with the same density. Note that there is no justification about the physical meaning of KS eigenvalues, except that KS wave functions ψ_n produce the true ground state electron density.

Since the Hamiltonian depends on the electron density, which is constructed by the KS wave function, then we can solve it in a self-consistent fashion:

$$\rho_{old} \rightarrow H_e \rightarrow \psi_n \rightarrow \rho_{new}. \quad (2.5)$$

Therefore the total energy can be written as:

$$E[\rho(\mathbf{r})] = T_{KS}[\{\psi[\rho(\mathbf{r})]\}] + \frac{1}{2} \int d\mathbf{r} d\mathbf{r}' \frac{\rho(\mathbf{r})\rho(\mathbf{r}')}{|\mathbf{r} - \mathbf{r}'|} + \int d\mathbf{r} \rho(\mathbf{r}) V_{ext}(\mathbf{r}) + E_{xc}[\rho(\mathbf{r})], \quad (2.6)$$

where the second term is the Hartree energy, the third term is the external potential energy and the last term includes the exchange-correlation contribution from the non-classical correction and many body effects. Note here that $T_{KS} = \sum_n^N \langle \psi_n | -\frac{\nabla^2}{2} | \psi_n \rangle$ and the difference $(T[\rho] - T_{KS}[\rho])$ is put into the $E_{xc} = T[\rho] - T_{KS}[\rho] + E_x[\rho] + E_c[\rho]$, where $E_x[\rho]$ and $E_c[\rho]$ denote the exchange and correlation parts. By doing this, the very large part of energy contribution is described reasonably.

2.3 Exchange-correlation functional

Now the problem has been very much simplified into a independent particle problem with the variable of electron density. But the exact form of E_{xc} is unknown. There are several ways to approximate this term. The most widely used is the local density approximation (LDA)[30]. The main idea is to consider a general inhomogeneous electronic system as locally homogeneous. In practice, energy terms local in the density are calculated by integrating over the volume of the system:

$$E_{xc}[\rho(\mathbf{r})] = \int d\mathbf{r} \rho(\mathbf{r}) \varepsilon_{xc}^{hom}(\rho(\mathbf{r})), \quad (2.7)$$

where ε_{xc}^{hom} denotes the exchange-correlation energy density of the homogeneous electron gas, which can be solved accurately via numerical methods[31]. The LDA neglects corrections due to the nearby inhomogeneities (non-local contributions) in the electron density. Beyond the LDA, we have the generalized gradient approximation (GGA)[32], meta-GGA, hybrid functional etc[33, 34, 35]. In general, the more accurate the functional, the more computationally demanding.

2.4 Projector-augmented wave method

In practice, core electrons are localized around nuclei and are chemically inert. Therefore do not play an important role in the chemical bonding and electronic structure in most cases. On the other hand, we need large amount of basis functions to describe the strongly oscillating wave functions of core electrons. It will largely increase the computational demand. Therefore it is intuitive to freeze core electrons with nuclei and produce a pseudo-potential. For valence electrons, the part of wave function within the core region is replaced by the smooth pseudo wave function. This is the so-called pseudo-potential method[36, 37].

In this thesis, we use the projector-augmented wave (PAW) method implemented in the GPAW code[38, 39, 40, 41]. It is an all electron method in the sense that valence electrons are kept orthogonal to core electrons. The advantage of this scheme is that it remains the accuracy of all electron scheme within the frozen core approximation, but decompose the all electron wave function into a smooth pseudo wave function and a rapidly varying contribution localized within the core region. Therefore the full pseudo-potential machinery can be taken advantage to speed up the calculation. The true all electron wave function $|\psi_n\rangle$ and the smooth pseudo wave function $|\tilde{\psi}_n\rangle$ are related by a linear transformation \hat{T} [42]

$$|\psi_n\rangle = \hat{T}|\tilde{\psi}_n\rangle. \quad (2.8)$$

2.5 Basis sets

To represent a wave function, we need to choose a basis set. In this thesis, two types of basis set are used, namely linear combination of atomic orbitals (LCAO) [43] and grid representation implemented in GPAW. The grid representation is used for the energy related properties, since we can converge the basis set systematically by decreasing the grid spacing. On the other hand, the LCAO is used for the electron transport calculations due to its locality. In the LCAO, the

KS pseudo wave functions $\psi_n(\mathbf{r})$ are expanded by a set of atomic-like orbitals $\phi_\mu(\mathbf{r})$,

$$\psi_n(\mathbf{r}) = \sum_{\mu} c_{\mu n} \phi_{\mu}(\mathbf{r}) \quad (2.9)$$

where basis functions are constructed as products of numerical radial functions and spherical harmonics.

2.6 Boundary conditions

Bloch's theorem[44] allows us to convert a problem of infinite number of electrons in a solid to a problem of finite number of electrons in a unit cell at infinite number of k points. The k points is constrained to lie in the first Brillouin Zone (BZ). Many interesting quantities such as charge density, total energy, etc. are evaluated by integrating over the first BZ. For instance, the charge density:

$$\rho(\mathbf{r}) = \frac{1}{\Omega_{BZ}} \sum_n \int_{BZ} f_{n\mathbf{k}} |\psi_{n\mathbf{k}}(\mathbf{r})|^2 d\mathbf{k}, \quad (2.10)$$

where Ω_{BZ} and $f_{n\mathbf{k}}$ denote the volume of the first BZ and the Fermi-Dirac distribution.

Since the distribution of \mathbf{k} is very dense, we can substitute the integration over the \mathbf{k} with a weighted sum over a discrete set of points: $\int_{BZ} 1/\Omega_{BZ} d\mathbf{k} \rightarrow \sum_{\mathbf{k}} \omega_{\mathbf{k}}$, where $\omega_{\mathbf{k}}$ denotes the weight of the k -points. This is the so-called k -point sampling[45].

In order to model aperiodic systems like molecules, surfaces and defects with periodic boundary conditions, we need to use the supercell method. It is important to make sure the physical and chemical properties are converged with respect to the supercell size. For example to model a surface, we need to put enough vacuum in the direction normal to the surface, in order to separate the interaction with the other surface. The surface in plane can be sampled by a k -point mesh.

Electron transport calculations

The conductance of a macroscopic conductor follows the Ohm's law,

$$\mathcal{G} = \sigma \frac{A}{L}, \quad (3.1)$$

where σ , A , L denotes the conductivity, the cross-section and the length of the conductor. However this equation is not valid when the quantum nature of the system starts to play a role. For molecular junction systems we are interested in this thesis, the length scales of those systems fulfil the following inequalities[46, 47]

$$\lambda_F \approx l_m < L < l_\phi, \quad (3.2)$$

where λ_F , l_m , l_ϕ denotes the Fermi wave length, the mean free path and the phase coherence length. To investigate the steady state electron transport in those molecular junction systems, the non-equilibrium Green function technique (NEGF)[48, 49, 50] combined with the *ab initio* description of the electronic structure can be applied.

In this chapter, the basics of the NEGF formalism will be introduced as well as the description of the electron-electron interaction with either DFT or the many-body perturbation theory. Additionally a semi-empirical method, DFT+ Σ , is formulated in detail.

3.1 Transport setup

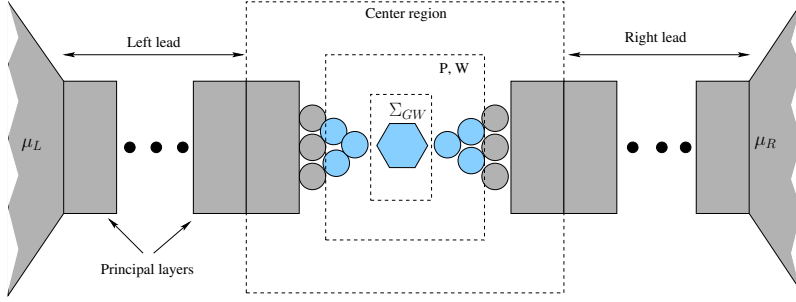


Figure 3.1: The schematic model for the electron transport through a molecule (the blue hexagon) sandwiched by the left/right semi-infinite leads (the circles plus the boxes) which are connected to the left/right macroscopic reservoirs at the temperature $T_{L/R}$ and the chemical potential $\mu_{L/R}$. One single box represents one principal layer.

The schematic model of a typical molecular system is shown in Fig. 3.1. A single molecule (the blue hexagon) is sandwiched by two semi-infinite leads (the circles plus the boxes). The left/right lead is connected to the left/right macroscopic reservoir at the temperature $T_{L/R}$ and the chemical potential $\mu_{L/R}$. Since the reservoirs are macroscopic objects, the electrons coming in and out the leads are thermalized at the temperature $T_{L/R}$ and the chemical potential $\mu_{L/R}$. We assume that the leads are perfect crystal without any scattering processes.

The general current formula for the system is[51, 52]:

$$I = \frac{i}{4\pi} \int \text{Tr}[(\Gamma_L - \Gamma_R)G^< + (f_L\Gamma_L - f_R\Gamma_R)(G^r - G^a)]d\varepsilon \quad (3.3)$$

where G is the interacting Green function matrix of the center region, $\Gamma_{L/R}$ is the coupling strength between the center region and the left/right lead, $f_{L/R}$ is the Fermi-Dirac distribution of the left/right reservoir. Note that the energy dependence are dropped out for simplicity.

The interacting G can be calculated from the Dyson equation[53]

$$G = G_0 + G_0\tilde{\Sigma}G \quad (3.4)$$

where G_0 is the non-interacting Green function matrix of the center region and the self-energy $\tilde{\Sigma}$ includes the perturbation from the lead and the electron correlation.

3.2 NEGF+DFT

In this section, we will describe the NEGF combined with DFT. The non-interacting DFT Hamiltonian includes the electron-electron interaction at a mean field level. Therefore the $\tilde{\Sigma}$ in Eq. 3.4 only includes the perturbation from the left/right leads. By using strictly localized basis sets, for instance the numerical atomic orbitals generated by the confinement scheme, the non-interacting DFT Hamiltonian of the entire system (the left/right leads plus the center region) can always be partitioned into

$$H_0 = \begin{bmatrix} H_L & H_{LC} & 0 \\ H_{LC}^\dagger & H_C & H_{RC} \\ 0 & H_{RC}^\dagger & H_R \end{bmatrix} \quad (3.5)$$

where H_α with $\alpha \in L, R$ is the Hamiltonian matrix of the leads, $H_{\alpha C}$ is the coupling matrix between the leads and the center region and H_C is the Hamiltonian matrix of the center region.

According to the Dyson equation Eq. 3.4, the interacting retarded Green function at the DFT level is

$$G^r(\varepsilon) = [(\varepsilon + i\eta)S - H_0 - \Sigma_L(\varepsilon) - \Sigma_R(\varepsilon)]^{-1}, \quad (3.6)$$

where

$$H_{0,ij} = \langle \phi_i | -1/2 \nabla^2 + \nu_{ion}(\mathbf{r}) + \nu_H(\mathbf{r}) + \nu_{xc}(\mathbf{r}) | \phi_j \rangle, \quad (3.7)$$

$$S_{ij} = \langle \phi_i | \phi_j \rangle, \quad (3.8)$$

denotes the KS Hamiltonian matrix and overlap matrix in numerical atomic basis functions. Additionally, the perturbations from the left/right leads are included by the self-energies:

$$\Sigma_\alpha^r(\varepsilon) = ((\varepsilon + i\eta)S_{C\alpha} - H_{C\alpha})g_\alpha^{0,r}(\varepsilon)((\varepsilon + i\eta)S_{C\alpha}^\dagger - H_{C\alpha}^\dagger), \quad (3.9)$$

where the surface Green's function

$$g_\alpha^{0,r}(\varepsilon) = ((\varepsilon + i\eta)S_\alpha - H_\alpha)^{-1} \quad (3.10)$$

Due to the periodicity in the crystal leads, the semi-infinite leads can always be constructed by infinitely repeated principal layers(integer number of periodicity). By using localized basis, the first nearest coupling is allowed between the principal layers.

The Hamiltonian of the left lead has the form

$$H_L = \begin{bmatrix} \cdots & \vdots & \vdots & \vdots \\ \cdots & h_0 & h_1 & 0 \\ \cdots & h_1^\dagger & h_0 & h_1 \\ \cdots & 0 & h_1^\dagger & h_0 \end{bmatrix} \quad (3.11)$$

where h_0 is the Hamiltonian matrix of a single principle layer and h_1 is the coupling Hamiltonian matrix between the two principle layers. A similar form applies to the right lead.

Because only the first principle layer is coupled to the center region, the surface Green's function can be evaluated by iterative methods[54]. Additionally, the coupling between the left/right lead and the center region $H_{\alpha C}$ is identical to the coupling between two principle layers h_1 . This can be justified by putting enough layers of lead into the center region. In the case of metals with short screening lengths, we are able to make the properties converge into lead at the boundary with a few atomic layers.

3.3 NEGF+GW

In this section, we will describe the NEGF formalism combined with the many-body perturbation theory, namely the description of the electron-electron interaction at the GW level. The non-interacting Green's function G_0 can be reasonably constructed from the single-particle KS-DFT scheme. Therefore the retarded Green's function of the center region is calculated by

$$G^r(\varepsilon) = [(\varepsilon + i\eta)S - H_0 + V_{xc} - \Delta V_H[G] - \Sigma_L(\varepsilon) - \Sigma_R(\varepsilon) - \Sigma_{xc}[G](\varepsilon)]^{-1}, \quad (3.12)$$

In Eq. 3.3 the Hartree potential change is calculated from

$$\Delta V_{H,ij} = 2 \sum_{kl} \nu_{ij,kl} (\varrho_{kl} - \varrho_{kl}^0) \quad (3.13)$$

where

$$\varrho = -i \int G^<(\varepsilon) d\varepsilon \quad (3.14)$$

$$\varrho^0 = -i \int G_0^<(\varepsilon) d\varepsilon \quad (3.15)$$

$$\nu_{ij,kl} = \iint \frac{\phi_i^*(\mathbf{r}) \phi_j(\mathbf{r}) \phi_k(\mathbf{r}') \phi_l^*(\mathbf{r}')}{|\mathbf{r} - \mathbf{r}'|} d\mathbf{r} d\mathbf{r}' \quad (3.16)$$

denotes the interacting density matrices, the KS density matrices and the bare Coulomb interactions in atomic orbital basis functions.

In Eq. 3.3 the KS exchange-correlation functional $V_{xc,ij} = \langle \phi_i | \nu_{xc}(\mathbf{r}) | \phi_j \rangle$ is replaced by the many-body self-energy Σ_{GW} which is approximated at the GW level. The GW self energy can be symbolically written as[53]

$$\Sigma_{GW} = iGW, \quad (3.17)$$

where

$$W = \epsilon^{-1}\nu, \quad (3.18)$$

$$\epsilon = 1 - \nu P, \quad (3.19)$$

$$P = -iGG, \quad (3.20)$$

denotes the screened interaction, the dielectric function and the irreducible density response function. The GW method is described in detail in Ref. [55, 56, 57].

P , W and Σ_{GW} are calculated for the extended molecule (The part in blue as shown in Fig. 3.1). However only the Σ_{GW} corresponding to the molecule is kept and the lead part is replaced by the DFT xc potential,

$$\Sigma_{xc}(\varepsilon) = \begin{bmatrix} \nu_{xc} & \nu_{xc} & \nu_{xc} \\ \nu_{xc} & \Sigma_{GW}(\varepsilon) & \nu_{xc} \\ \nu_{xc} & \nu_{xc} & \nu_{xc} \end{bmatrix}. \quad (3.21)$$

This treatment ensures that the lead is consistently treated at the DFT level. More importantly, the unconverged part of Σ_{GW} at the edge is removed, but the correlation interaction between the molecule and the leads is included in Σ_{GW} .

The calculation is performed self-consistently using a linear mixing of Green's functions as

$$G_{old} \rightarrow P \rightarrow \epsilon \rightarrow W \rightarrow \Sigma_{xc} \rightarrow G_{new}. \quad (3.22)$$

The self-consistent solution ensures the charge continuity condition[58, 59] and removes the starting point dependency.

3.4 DFT+ Σ

In this section, the DFT+ Σ method will be formulated in detail[60, 61, 62]. This semi-empirical method is computationally much cheaper than the GW calculations. It corrects the KS eigenvalues of the frontier molecular orbitals

in the gas phase and also includes the image charge effect via a classical image charge model.

First, despite the unjustified physical meaning of the KS eigenvalues, the KS HOMO-LUMO gap is typically underestimated by several eV s. This can be corrected by shifting the KS HOMO and LUMO energies to match the experimental values:

$$\Delta_{1,occ} = -IP - \epsilon_H \quad (3.23)$$

$$\Delta_{1,unocc} = -EA - \epsilon_L. \quad (3.24)$$

Here the calculated ionization potential (IP) and electron affinity (EA) from total energy difference approach is used instead:

$$IP = E(N - 1) - E(N) \quad (3.25)$$

$$EA = E(N) - E(N + 1), \quad (3.26)$$

where $E(N)$, $E(N + 1)$, $E(N - 1)$ denotes the total energy of the neutral, -1 charged, +1 charged of the gas phase molecule.

When a molecule is approaching a metal surface, an induced image charge in the metal surface will renormalize molecular levels. The reduction of the HOMO-LUMO gap can be included via a classical image charge model. The image charge energy for a point charge distribution placed between two image planes located at $x = 0$ and $x = L$ is

$$\begin{aligned} \Delta_2 &= \frac{1}{8\pi\epsilon_0} \sum_{\alpha=1}^N \sum_{\beta=1}^N \rho_i(r_\alpha) \rho_i(r_\beta) \\ &\times \sum_{n=1}^{\infty} \left[\frac{1}{\sqrt{(x_\alpha + x_\beta - 2nL)^2 + R_{\alpha\beta}^2}} \right. \\ &+ \frac{1}{\sqrt{(x_\alpha + x_\beta - (n-1)L)^2 + R_{\alpha\beta}^2}} \\ &- \frac{1}{\sqrt{(x_\alpha - x_\beta + 2nL)^2 + R_{\alpha\beta}^2}} \\ &\left. + \frac{1}{\sqrt{(x_\alpha - x_\beta - 2nL)^2 + R_{\alpha\beta}^2}} \right] \end{aligned} \quad (3.27)$$

where x_α is the x -coordinate of atoms α , $R_{\alpha\beta} = \sqrt{(y_\alpha - y_\beta)^2 + (z_\alpha - z_\beta)^2}$ and $\rho_i(r)$ is the point charge distribution for a given orbital i .

The image charge correction relies on the assumption that the screening by metal electrodes can be described classically as two flat conductors characterized by an image plane. The image plane position can in principle be calculated for a single flat surface using DFT [63, 64, 65] yielding around 1.0 Å outside the last metal layer. The situation is, however, more complicated for a tip structure, and one might expect a reduced screening with the effective image plane further away from the molecule. Therefore the positions of the image charge plane are input parameters.

The total corrections of the KS eigenvalues for a molecule contacted to metal electrodes is

$$\Sigma_{occ/unocc} = \Delta_{1,occ/unocc} + \Delta_{2,occ/unocc} \quad (3.28)$$

Then the H_{mol} spanned by the basis functions on the molecular atoms is replaced by the corrected \tilde{H}_{mol} :

$$\begin{aligned} \tilde{H}_{mol} &= H_{mol} + \Sigma \\ &= \sum_{i \in occ/unocc} (\epsilon_i + \Sigma_{occ/unocc} |\psi_i\rangle \langle \psi_i|) \end{aligned} \quad (3.29)$$

Finally the whole corrected \tilde{H} is used to construct the Green's function Eq. 3.3.

3.5 Conductance and thermopower

In the *linear response regime* (currents are linear in ΔT and $\Delta\mu$), where $\Delta T = T_L - T_R \ll T$ and $\Delta\mu = \mu_L - \mu_R = e\Delta V \ll \mu$. The conductance and thermopower are calculated from [66, 67]

$$\mathcal{G} = e^2 \mathcal{L}_0(\epsilon_F) \quad (3.30)$$

and

$$\mathcal{S} = \frac{\mathcal{L}_1(\epsilon_F)}{eT\mathcal{L}_0(\epsilon_F)} = -\frac{\pi^2 k_B^2 T}{3e} \left. \frac{\partial \ln(\mathcal{T}(\epsilon))}{\partial \epsilon} \right|_{\epsilon=\epsilon_F}. \quad (3.31)$$

Here $\mathcal{L}_m(\mu)$ is defined as

$$\mathcal{L}_m(\mu) = \frac{2}{h} \int_{-\infty}^{\infty} d\epsilon \mathcal{T}(\epsilon) (\epsilon - \mu)^m \left(-\frac{\partial f(\epsilon, \mu, T)}{\partial \epsilon} \right), \quad (3.32)$$

where the transmission function can be calculated from[51, 52]

$$\mathcal{T}(\varepsilon) = \text{Tr}[G^r(\varepsilon)\Gamma_L(\varepsilon)G^a(\varepsilon)\Gamma_R(\varepsilon)] \quad (3.33)$$

and $f(\varepsilon, \mu, T)$ is the Fermi-Dirac distribution function. Note Eq. 3.5 is derived from the non-interacting picture, but in the linear response region it is also valid for the interacting picture[68].

The last expression in \mathcal{S} assumes that the transmission is slowly varying around ε_F [69]. T is the average temperature of the left and right electrodes. We note that the thermopower in Eq. 3.31 is defined within linear response, and is thus applicable when $\Delta T/T$ is small. The non-linear effects are expected to be of minor importance, since the experiments were done with $T \approx 300$ K and $|\Delta T| < 30$ K. Moreover, the measured thermoelectric current is linearly dependent with small ΔT in the experiments, indicating that the linear response formula is adequate.

Energy level alignment

Over the last decade, it has been clear that in order to close the discrepancy between experimental conductances and calculated ones, it is necessary to have an accurate theoretical description of the molecular energy levels in molecular junctions.

Despite the unjustified physical meaning of the KS energies and wave functions, NEGF+DFT is used as a standard tool to provide qualitative understanding of the electron transport in nano-scale systems[70, 71, 72, 73]. However because standard DFT suffers from the underestimation of HOMO-LUMO gaps[74, 75], the calculated conductances are overestimated by several orders of magnitude compared to experimental values in most molecular junctions.

This could be efficiently remedied by the GW approximation of the electronic structure[53, 76]. The GW method provides an accurate description of frontier molecular levels for gas-phase molecules[77, 78, 79]. Additionally, the GW method catches the image charge effect[80, 81, 82] when the molecule is sandwiched between two metal electrodes. NEGF+GW therefore provides an accurate energy level alignment at the molecule/metal interface and a quantitative description of electron transport in molecular junctions[83, 84, 85, 57, 86, 87, 88].

In this chapter, the NEGF formalism combined with either DFT or GW is applied to study the electron transport in different molecular junctions.

4.1 Functionalization of the benzene-diamine molecule

4.1.1 Motivation

Venkataraman *et al.*[89] reported that the conductance of a 1,4-benzenediamine (BDA) molecule sandwiched between two Au leads can be tuned to some extent by functionalizing the benzene molecule with different side groups. Since the conductance of Au-BDA-Au junction is mainly dominated by the highest occupied molecular orbital (HOMO), the conductance tuning results from the change of the level alignment between the HOMO level and the Au Fermi level. In the experiment, the HOMO level is shifted up in energy by the introduction of an electron donating (ED) side group and down in energy by an electron withdrawing (EW) side group. Although the effect of different functional groups on the conductance change is relatively small, the system can be used as a test-bed for a theoretical description of the energy level alignment and electronic transport through the molecules.

In this study, the effect of side groups on the conductance of Au-BDA-Au junctions is addressed using the NEGF with different levels of theory to describe exchange-correlation (xc) effects, namely DFT, DFT+ Σ , GW and HF. This section is based on Paper I.

4.1.2 Results and discussion

The atomic structure of the Au-BDA-Au junction is shown in Fig. 4.1. The other junctions are made by substituting the BDA molecule. The junction structures are optimized until the residual force on each atom is smaller than 0.01 eV/Å. For all the junctions, very small structural variations at the contact interface are observed due to the side group substitution. Since the conductance is relatively insensitive to the contact geometry for weakly coupled amine-linked junctions[17, 62, 90], we conclude that the origin of the conductance variation observed for the functionalized junctions is an electronic rather than a structural effect.

Fig. 4.2 (a) shows the transmission functions of the unsubstituted Au-BDA-Au junction, calculated using DFT-PBE, HF, and GW. The transmission functions of all the different functionalized BDA junctions around the Fermi energy are shown in Fig. 4.2 (b). The effect of side groups on conductance is weak, indicating by the small change in the transmission shape and the values of the transmission around the Fermi energy. It is HOMO mediated electron transport

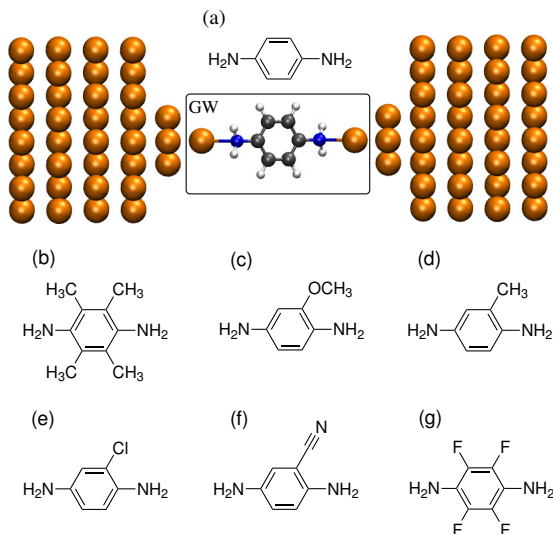


Figure 4.1: (a) The atomic structure of the Au-BDA-Au junction. The amine linkers connect the benzene ring to the gold electrodes via two 3-fold coordinated gold atoms. The black box indicates the region where the GW self-energy is evaluated self-consistently. The other structures considered are constructed by replacing BDA by (b) BDA+CH₃*4, (c) BDA+OCH₃, (d) BDA+OCH₃, (e) BDA+Cl, (f) BDA+CN, (g) BDA+F*4.

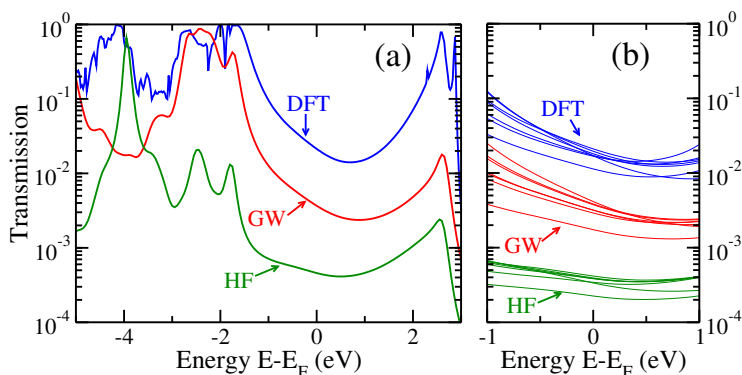


Figure 4.2: (a) The transmission function for the unsubstituted BDA junction calculated using DFT-PBE, HF and the self-consistent GW approximation. (b) The transmission functions for different functionalized BDA junctions.

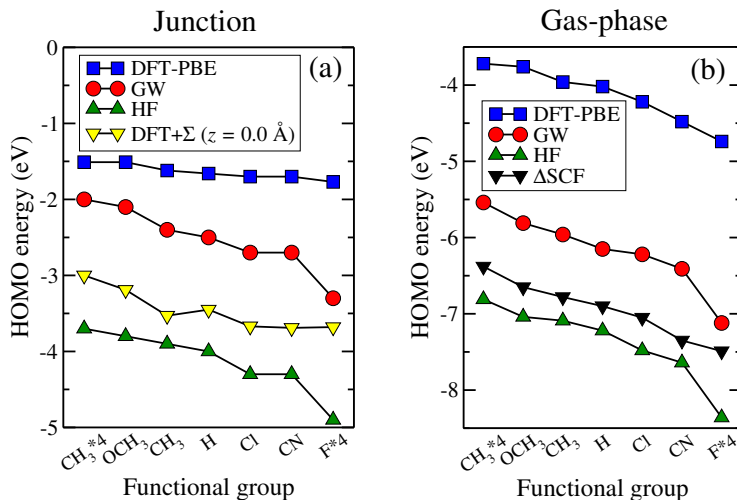


Figure 4.3: (a) The HOMO positions relative to the Fermi level of different functionalized BDA junctions calculated using DFT-PBE, HF, the self-consistent GW approximation and DFT+ Σ . The position of the HOMO is taken as the first transmission peak below the Fermi level. (b) The HOMO positions in the gas-phase relative to the vacuum level.

in all the cases, indicated by the position of the Fermi level crossing the HOMO resonance. It has a negative Seebeck coefficient since the Fermi level is crossing the tail of the HOMO resonance, in agreement with the experimental finding on Au-BDA-Au junctions[91].

Fig.4.3 (a) and (b) shows the positions of the HOMO resonance in the junction and in the gas-phase respectively, calculated using different methods. The functional groups have been ordered according to their ED/EW nature with the most donating groups to the left and the most withdrawing groups to the right.

In the gas-phase, the same trend for the HOMO position is observed in all the methods, but considerable differences are observed both in the absolute values as well as the relative differences between the molecules. Using either GW or Δ SCF as a reference, the DFT-PBE levels are typically overestimated by 2-3 eV while HF underestimates by 0.5-1 eV. This is because, while the DFT-PBE HOMO level are overestimated due to the spurious self-interaction in PBE xc functional, the self-interaction free HF approximation underestimates the HOMO due to the missing correlation.

Fig. 4.3 (a) shows that the general trend of the HOMO position observed in the gas-phase carry over to the contacted molecules in the junctions. While

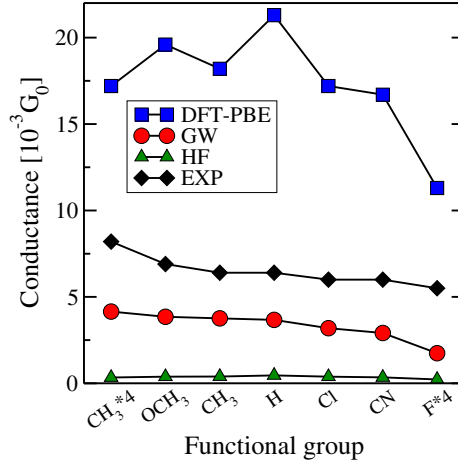


Figure 4.4: The conductance of side group functionalized BDA junctions calculated using DFT-PBE, HF, and self-consistent GW. The experimental conductances are shown in black.

the relative HOMO resonance positions in the junctions with GW and HF are almost unchanged from the gas-phase and still show a variation of around 1.5 eV, the DFT-PBE HOMO resonance positions vary much less with the side groups compared to the gas-phase and show a total variation of only 0.25 eV. The stronger pinning of the HOMO to the Fermi level in the DFT-PBE calculations results from the larger overlap of the HOMO resonance with the Fermi level in DFT and from the spurious self-interaction which enhances the effective fields making it energetically more difficult for charge to flow to/from the HOMO. In addition, the strong pinning in DFT is inherited in DFT+ Σ , showing a small total variation of 0.7 eV.

The screening is enhanced by metal electrodes which shifts the HOMO level upwards in energy, when the molecule is sandwiched in the junction[83, 85]. While HF and DFT completely miss this effect, the GW method naturally captures this feature, which can be seen from the increased distance between the GW and HF levels when going from the gas-phase to the junction in Fig. 4.3. The screening (image charge shift) amounts to around 0.4 eV on average for the functionalized BDA junctions studied here.

The calculated zero-bias conductances are shown in shown in Fig. 4.4 with the corresponding values are listed in Tab. 4.1. The DFT-PBE conductances overestimate the experimental values by a factor of 3, while the HF conductances underestimate the experimental values by a factor of 20. Inclusion of the screening at the GW level brings the conductances closer to the experimental values,

Table 4.1: The summary of conductances (in units of $10^{-3}G_0$) calculated using DFT-PBE, GW, HF, and DFT+ Σ for different image plane positions, namely $z = -1.0, 0.0, +1.0$ Å relative to the Au tip atom. The last column are the experimental conductances[89].

	Effect	DFT	GW	HF	DFT+ Σ			EXP
					-1.0 Å	0.0 Å	+1.0 Å	
CH ₃ *4	donor	17.2	4.15	0.337	4.41	6.24	10.79	8.2±0.2
OCH ₃	donor	19.6	3.85	0.385	3.37	4.26	6.23	6.9±0.2
CH ₃	donor	18.2	3.76	0.393	3.16	3.77	5.81	6.4±0.6
H		21.3	3.67	0.459	3.57	4.51	6.69	6.4±0.2
Cl	acceptor	17.2	3.19	0.384	3.35	3.88	5.90	6.0±0.4
CN	acceptor	16.7	2.91	0.343	3.05	3.52	5.29	6.0±0.3
F*4	acceptor	11.3	1.74	0.225	3.42	4.13	6.65	5.5±0.3

but the GW method still underestimates the experimental values by a factor of 2.

Surprisingly the relative effect of the functional groups is only correctly predicted using the GW method, given the fact that the changes of the DFT HOMO positions follow the ED and EW effects of the substituent groups as well. Specifically, functional groups with donor characteristic such as CH₃*4, OCH₃ and CH₃ increase the conductance, while functional groups with acceptor characteristic such as Cl, CN, and F*4 decrease the conductance. As shown in Fig. 4.3, due to the stronger effect of pinning to the metal Fermi level, the changes of the DFT HOMO positions are relatively small compared to the GW results. As a result, the variation in the DFT conductances is more sensitive to other effects[88] and does not reflect the (small) variation in the level positions.

In Fig. 4.5, the DFT+ Σ results are compared with GW and experimental values. The conductances of the $z = +1.0$ Å image plane position are in agreement with the experimental values. The image charge energies are reduced when shifting the image planes further away from the molecule by $z = -1.0$ Å or $z = 0.0$ Å. This implies that the molecular levels are shifted away from the Fermi level, and the conductances are lowered to values closer to the GW results. While the DFT+ Σ conductances are in overall good agreement with the experiments, the changes in conductance with different side groups are not correctly captured by this method.

We can also consider the DFT+SO method, where the positions of the DFT HOMO and LUMO levels are shifted using a scissor operator to match the positions of GW HOMO and LUMO levels. The DFT+SO method recovers the correct ordering of the conductance as shown in Fig. 4.5. The relative conductance

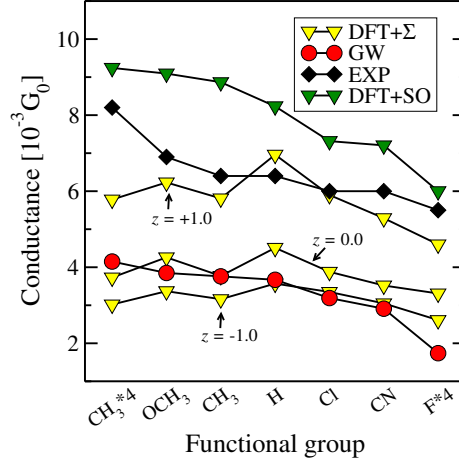


Figure 4.5: The conductance of the functionalized BDA junctions calculated using the DFT+ Σ method (yellow) with three different image plane positions, namely $z = -1.0, 0.0, +1.0$ Å relative to the Au tip atom, compared with the GW, DFT+SO and experimental results.

difference between the DFT+SO and GW results from the frequency dependence of the GW self-energy which is absent in DFT+SO[88]. The DFT+SO results further support the interpretation that the wrong ordering of the conductances in DFT and DFT+ Σ is a consequence of incorrect level alignment.

In conclusion, we have studied the role of energy level alignment for a correct description of the electronic conductance of side group functionalized BDA molecular junctions. It was found that the self-consistent GW method yields excellent agreement with experiments for both qualitative trends and absolute conductance values. In contrast, because of the over-pinning of the molecular levels to the Au Fermi level, the energy level alignment is incorrectly predicted by DFT and DFT+ Σ . Therefore both standard DFT and the scissors operator corrected DFT+ Σ method failed to catch the relative variation in conductance with functional groups.

4.2 The effect of contact variation on conductance and thermopower

4.2.1 Motivation

With the global energy shortage issue, thermoelectric materials provide a promising solution to convert waste heat into electricity. On the other hand, by applying electric potential, thermoelectric materials can be utilized to cool or heat devices. This is called thermoelectric effect.

The efficiency of thermoelectric materials can be measured by the dimensionless figure of merit

$$ZT = \frac{S^2 GT}{\kappa_{ph} + \kappa_e}, \quad (4.1)$$

where S : the Seebeck coefficient, G : the electronic conductance, T : the average temperature, κ_{ph} : the phonon thermal conductance and κ_e : the electron thermal conductance. To date, the best reported ZT values are in the $2 \sim 3$ range[92].

Ideally, to get the best ZT , we should have large S , large G and small κ . Typically, for bulk materials, these quantities are interrelated and cannot be controlled independently: lowering the thermal conductance typically also lowers the electrical conductance.

One promising approach is to use molecular junctions to improve the thermoelectric effect. This has been demonstrated both experimentally and theoretically[93, 24]. This opens a new way to improve the efficiency of thermoelectric devices. However to understand the factors that influence ZT at the atomic scale is quite challenging experimentally.

In addition, thermopower measurements are used as a spectroscopic technique because they characterize whether the electron transport is mediated by the HOMO or the LUMO.

In this study, the conductance and the thermopower of benzenediamine (BDA) and benzenedicarbonitrile (BDCN) molecules contacted to Au electrodes are calculated using DFT, GW and DFT+ Σ . While the electron transport in Au-BDA-Au junctions are HOMO-mediated, it is LUMO-mediated in Au-BDCN-Au junctions. We focus on accessing the sensitivity of these quantities on the atomic details of the electrode-molecule interface. This section is based on Paper II.

4.2.2 Results and discussion

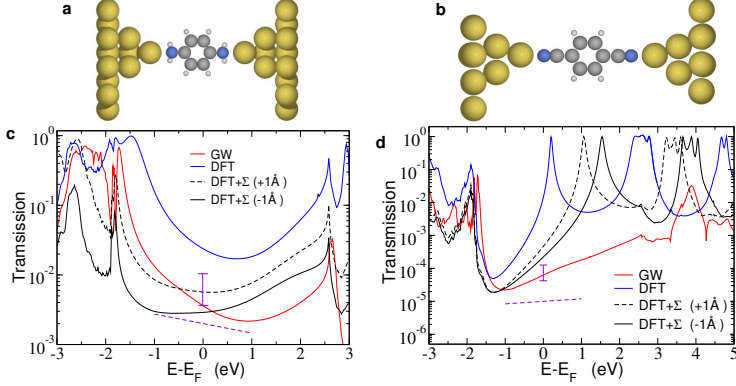


Figure 4.6: The atomic structure of Au-BDA-Au junction (a) and Au-BDCN-Au junction (b) with the perfect tip contacts. The corresponding transmission functions are shown in (c) and (d), calculated using DFT, GW and DFT+ Σ . Two positions of the image charge plane are used, namely $\pm 1 \text{ \AA}$. The experimental conductances and thermopowers are indicated by the vertical bar and the slope of the dashed line at the Fermi energy respectively.

Starting with perfect tip contacts, three different methods, namely DFT, DFT+ Σ and GW, are applied. The transmission functions of Au-BDA-Au junction and Au-BDCN-Au junction with the perfect tip contacts are shown in Fig. 4.6. The calculated conductance and thermopower values are listed in Tab. 4.2.

Table 4.2: Summary of the calculated conductances and thermopowers of the Au-BDA-Au junctions and the Au-BDCN-Au junction with perfect tip contacts, compared with experimental values. The conductances and thermopowers are in units of G_0 and $\mu V/K^{-1}$ respectively.

	BDA		BDCN	
	G	S	G	S
Exp.	6.4×10^{-3}	2.3	8.4×10^{-5}	-1.3
GW	3.6×10^{-3}	7.8	6.3×10^{-5}	-9.2
DFT	24×10^{-3}	6.7	1.9×10^{-2}	-129
DFT+ $\Sigma(+1\text{\AA})$	5.7×10^{-3}	0.8	4.7×10^{-4}	-24
DFT+ $\Sigma(-1\text{\AA})$	2.9×10^{-3}	-0.9	2.2×10^{-4}	-19

In the BDA case, both the GW and the DFT+ $\Sigma(+1 \text{ \AA})$ conductances agree with

the experiments, while the DFT overestimates the conductance by a factor of 2. All the methods show a positive thermopower in agreement with the experiment, except for the DFT+ Σ (-1 Å). Moreover the DFT+ Σ (+1 Å) conductance gives the best agreement with the experiment.

In the BDCN case, the DFT conductance is two orders of magnitude larger than the experiment because the DFT LUMO level is located too close to the Au Fermi level. The DFT+ Σ and GW give better conductances by correcting the LUMO level up in the energy. All the methods give a positive thermopower and the GW thermopower is in excellent agreement with the experiment.

To access the sensitivity of the contact details, different contact configurations are used namely, a tip, adatom or a trimer configuration as shown in Fig. 4.7. From the above conductance and thermopower calculations for the perfect tip contacts, GW and DFT+ Σ show improvement over DFT due to the better energy level alignment. Additionally, due to the high computational demand of the GW calculations, the DFT+ Σ method is applied in the remaining part of our study in order to provide an accurate description.

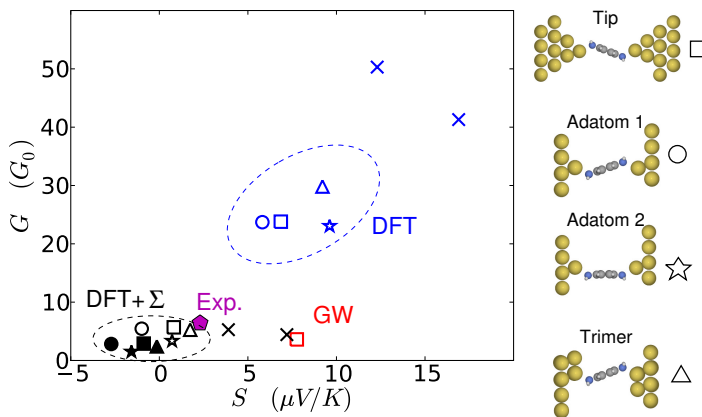


Figure 4.7: The conductance versus the thermopower of Au-BDA-Au junction with various contact geometries, calculated using DFT and DFT+ Σ . Two positions of the image charge plane are used, namely +1 Å (open symbols) and -1 Å (filled symbols). The cross indicates the calculated values from Ref. [91].

In the BDA case shown in Fig. 4.7, the conductance and thermopower of all four structures calculated using the DFT+ Σ (+1 Å) are in good agreement with the experiments, while the calculations with image planes placed 1 Å inside the Au

lead to negative thermopower, namely DFT+ Σ (-1 Å). The GW conductance is close to the experiments, but the thermopower is a factor of 3 larger. Both DFT conductances and thermopowers are largely overestimated. Compared to the previous calculations[91] which are done with different DFT codes and presumably different geometries, the agreement with our results are very close.

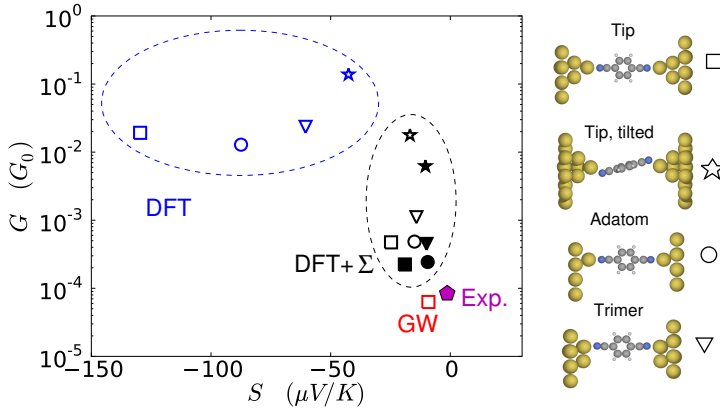


Figure 4.8: The conductance versus the thermopower of Au-BDCN-Au junction with various contact geometries, calculated using DFT and DFT+ Σ . Two positions of the image charge plane are used, namely +1 Å (open symbols) and -1 Å (filled symbols).

In the BDCN case shown in Fig. 4.8, the DFT conductances are 2-3 orders of magnitude larger while the DFT thermopowers are a factor of 30-100 larger, compared to the experiments. The DFT+ Σ conductances are 3-200 times larger than the experiments. The largest discrepancy is found for the tilted tip configuration, resulting from the strong coupling between the LUMO and the Au s-orbitals. On the other hand, the thermopower from DFT+ Σ are an order of magnitude larger than the experimental value. The GW method gives an excellent agreement with the experiments. The GW conductance is only 25% lower than the experimental value and the GW thermopower is larger by a factor of 7.

In conclusion, we have studied the electronic conductance and thermopower for BDA and BDCN single-molecule junctions. For both molecules, good agreement with experimental results are found with the exchange and correlation effects described by the self-consistent GW approximation. While the DFT conductances and thermopowers for different BDA junctions agree with experimental results within a factor of 5, much larger discrepancies are found for the BDCN

junction where the DFT results differ from the experiments by two orders of magnitude. By correcting the energy level alignment, DFT+ Σ improves the results for both BDA and BDCN. It is also found that the conductance and the thermopower are robust against the small structural changes. We demonstrated here that a proper treatment of exchange–correlation effects is important to have quantitative description of the energy level alignment and therefore the conductance and thermopower properties.

4.3 Electrochemical gating of nonredox molecules

4.3.1 Motivation

To realize a single molecular transistor, a gate electrode is required to control the molecular energy levels[94]. The electrochemical gate approach shown in Fig. 4.9 (a) can operate in room temperature liquid environments and produce high gate efficiency due to the achievable large electric field. Combined with scanning tunnelling microscope break junction techniques, it has been used to study the nonredox 4,4'-bipyridine (44BP) molecule sandwiched between Au contacts[95, 96].

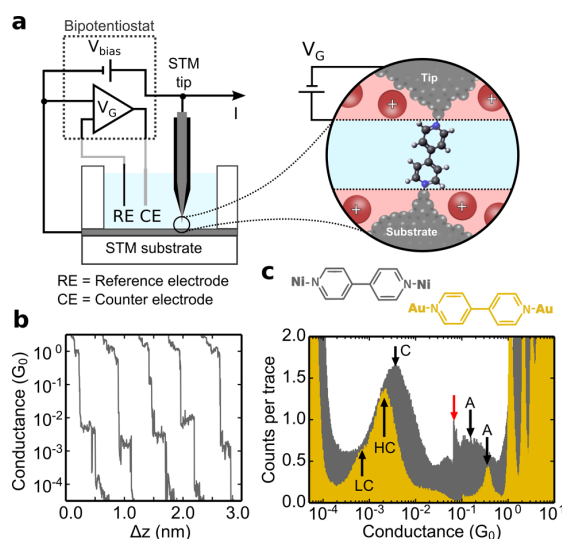


Figure 4.9: (a) The schematic of the electrochemical gating setup for scanning tunnelling microscope break junction measurements. (b) Examples of conductance traces. (c) The conductance histograms for Ni-44BP-Ni (gray) and Au-44BP-Au (yellow) junctions.

The metal-molecule contact plays a critical role in molecular electronics. Most single molecule junction experiments are done with Au contacts due to its chemical stability and mechanical elasticity. Using ferromagnetic metal contacts such as Ni could lead to *spininterface*, namely spin-dependent orbital hybridization at the metal-molecule interface [97, 98, 99]. In the electrochemical control approach, it becomes possible to use Ni contacts instead of Au contacts, because Ni can be prevented from oxidation.

In this study, electrochemical control is used to do nonredox gating for Ni-44BP-Ni and Au-44BP-Au single molecule junctions. The DFT based calculations are used to underpin the different gating mechanism for those two junctions. Specifically, the DFT+ Σ method is employed to calculate the conductance for both Ni-44BP-Ni and Au-44BP-Au junctions at different gate voltages. The GW method is used for Au-44BP-Au junction to benchmark the accuracy of the DFT+ Σ calculations. The gating effect is simulated by shifting the molecular states:

$$\Sigma_{gate} = \sum_n V_g |\psi_n\rangle \langle \psi_n|, \quad (4.2)$$

where V_g is the applied gate voltage and $|\psi_n\rangle$ is the molecular states calculated by diagonalizing the molecular part of the DFT Hamiltonian for the junction. This section is based on Paper III.

4.3.2 Results and discussion

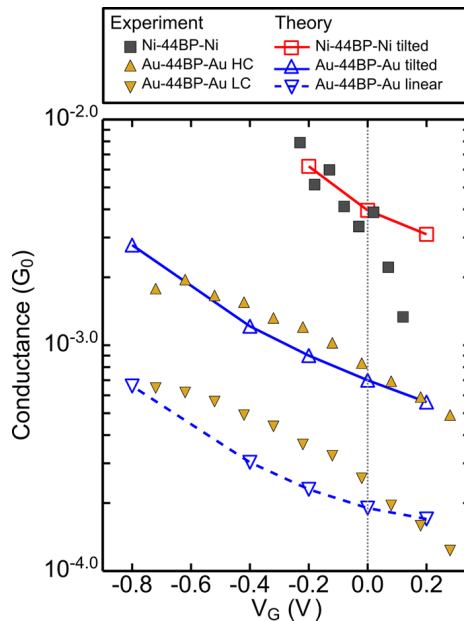


Figure 4.10: The experimental (open symbols) and calculated (filled symbols) conductances for Ni-44BP-Ni and Au-44BP-Au junctions as a function of the gating voltage. The squares and triangles are for the Ni and Au contacts respectively.

The experimental conductances of Ni-44BP-Ni and Au-44BP-Au junctions at different gating voltages are shown in Fig. 4.10. While two distinct conductance values are observed in the Au contacts, only one conductance values is measured in the Ni contacts. More interestingly, the Ni contacts not only shows much higher conductance than the Au ones, but also has much larger gate-dependency.

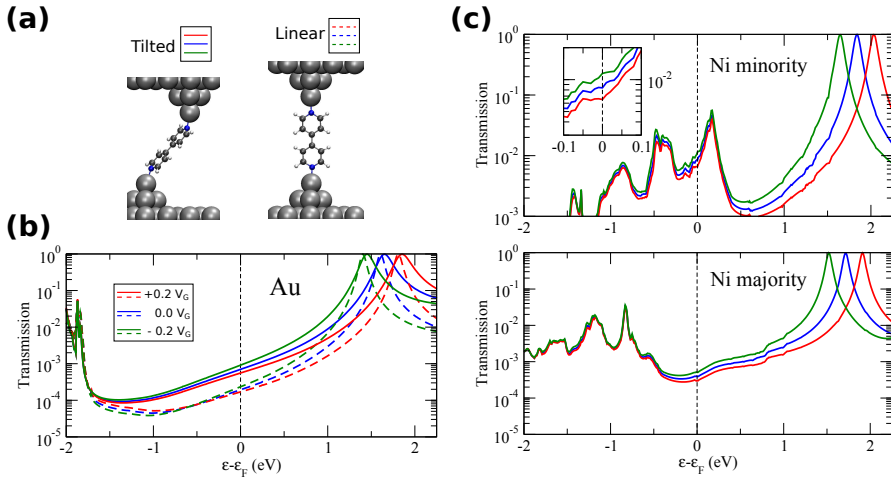


Figure 4.11: (a) The atomic structures of the tilted and linear configuration. (b) The transmission functions for Au-44BP-Au junctions at different gating voltages in the linear configuration (dashed lines) and in the tilted ones (solid lines). (c) The spin-dependent transmission functions for Ni-44BP-Ni junctions at different gating voltages in the tilted configurations. The inset is a transmission zoom-in around the Fermi energy.

The origin of the two distinct conductances in the Au contacts is ascribed to the two different junction geometries, seen in Fig. 4.11 (a), during the break junction experiments[100]. The DFT+ Σ calculations predict a higher conductance when the molecule is tilted compared to when it is linear. The transmission functions and the calculated conductances for Au contacts in the tilted and linear configurations are shown in Fig. 4.7 and Fig. 4.10 respectively. The tilted configuration enhances the coupling between Au s-orbitals and LUMO of the 44BP. As a result, the broadened LUMO resonance increases the conductance compared to the linear configuration. At the same time, the LUMO is pushed up in energy because the molecule is further negatively charged. Additionally, the GW calculations are performed to validate the DFT+ Σ calculations for the Au-44BP-Au junction and give $5.7 \times 10^{-3} G_0$ and $1.1 \times 10^{-3} G_0$ for the titled and linear configurations, in agreement with the DFT+ Σ .

In the case of Ni contacts, the linear and tilted configurations have similar conductances according to the DFT+ Σ . The Ni contacts have much larger binding energies for the tilted and linear configurations of 2.64 and 2.54 eV respectively, compared to the Au cases that the binding energies are 1.71 and 1.91 eV respectively. This suggests that both configurations are probed in the Ni break junction experiments, but are indistinguishable from each other because the conductance is insensitive to the contact angle. Note that only the transmission functions of the tilted configuration are shown in Fig. 4.11 (c) for clarification.

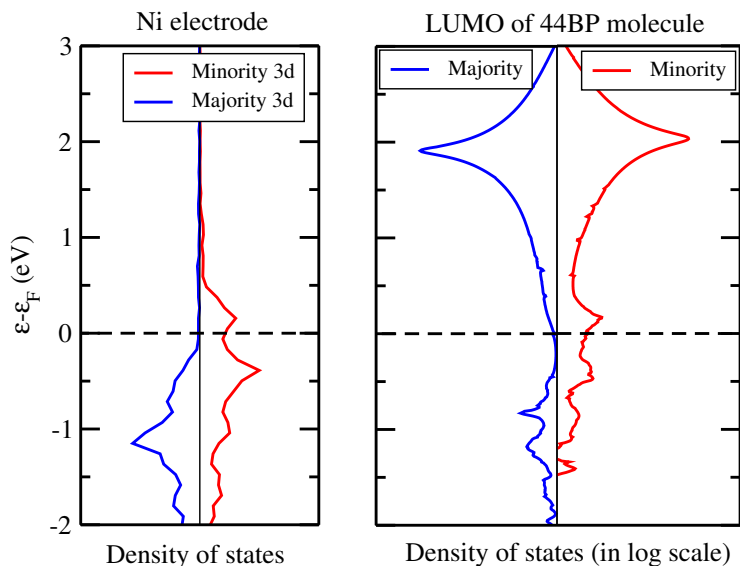


Figure 4.12: The density of states of the Ni electrode and the LUMO of 44BP molecule in the junction setup.

The enhanced gating efficiency and large conductance in the case of Ni contacts result from the ferromagnetic nature of the Ni electrodes. Fig. 4.11 (c) shows that the spin-degeneracy is lifted, resulting in one minority and one majority spin channels. In the minority channel, high transmission at Fermi energy is due to the coupling between the Ni d band and the LUMO of the molecule. This is called *spininterface*. On the other hand, weaker Ni d-LUMO hybridization in the majority channel results in small transmission at Fermi energy. The spin-polarization in the Ni contacts are clearly seen from the projected density of states in Fig. 4.12.

As the gate voltage applied to the Ni-44BP-Ni junctions is increased, the Fermi level is shifted closer to the LUMO and the hybridization of the LUMO with

the Ni d band increases. Consequently, the peak due to the hybridization in the minority channel is enhanced, which results in the increase of the conductance.

A pinning effect for the gating is observed experimentally in the case of Au contacts. However the calculated gating efficiency in Au contacts is similar to the Ni case. To clarify that, a self-consistent treatment of the gate is needed to take care of the charge transfer.

In conclusion, we have studied the electron transport and gating mechanisms of the 44BP molecule contacted to either Au or Ni electrodes. The two distinct conductance values in Au-44BP-Au junctions results from two possible junction geometries during the experiments. Furthermore, the DFT based calculations suggest that the larger conductance in Ni-44BP-Ni junctions over that in Au-44BP-Au junction results from the *spinterface*: The strong hybridization between the Ni d band and the LUMO of the 44BP molecule.

Beyond energy level alignment

The image charge could renormalize the energies of the molecular levels by decreasing/increasing the additional/removal energies. This enhanced screening effect accounts for an accurate energy level alignment at the molecule-metal interface.

In addition to energy level alignment, the electron transport could be effected by: (1) The polarization of the molecular wave functions due to the image charge induced in the metal electrodes. This would change the coupling strength at the molecule-metal interface[87]. (2) The finite formation time of the image charge. This means that the image charge is *lacking behind* the tunneling electron and results in a reduction of the effective metal-molecule coupling strength[88]. Both two effects are fully accounted in the GW calculations, apart from the accurate energy level alignment.

In this chapter, the effect of the finite image charge formation time will be studied in Sec. 5.1 and the consequence on the conductance and the thermopower in Sec. 5.2. Since the molecules of interest here have low polarizability, the image charge induced polarization is negligible.

5.1 Dynamical image charge effect

5.1.1 Motivation

An image charge (IC) is induced in metal electrodes when an electron tunnels between two metal electrodes. Under the assumption that the image charge is formed instantaneously, the effect on the energy level alignment can be taken into account by a static model for the image potential, as shown in the Chap. 4.

However, the response time of a noble metal is often comparable to the tunneling time. Therefore the static model is questionable in such situation. The time it takes to polarize the electrode is given roughly by the inverse plasmon frequency of the electrode, $\tau_p \approx 1/\omega_p$, while a simple expression for the time the electron spends on the molecule follows from the time-energy uncertainty relation $\tau_{tun} \approx \hbar/|E_F - \varepsilon_a|$, where ε_a is the energy of the molecular orbital closest to the Fermi level.

In this study, we explore the effect of the finite electrode response time to form an image charge. Firstly, we analytically derive and provide the explanation for the conductance suppression due to the finite image charge formation time. Then first-principles many-body calculations are performed to account for more realistic systems. This section is based on Paper IV.

5.1.2 Results and discussion

The electron transport through a localized electronic level $|a\rangle$ coupled to two electrodes is considered, as shown in Fig. 5.1. We assume that the finite spectral width γ is constant in the relevant energy range, and the level is unoccupied, i.e., $\varepsilon > E_F + \gamma$ (the case for an occupied level is treated completely analogously). The Green's function of the localized level:

$$G_a(\omega) = \frac{1}{[\omega - \varepsilon_a - \text{Re}\Sigma_a(\omega)] + i[\gamma - \text{Im}\Sigma_a(\omega)]} \quad (5.1)$$

where the self-energy $\Sigma_a(\omega) = \langle a|\hat{\Sigma}(r, r', \omega)|a\rangle$ contains only the correlation effects and the Hartree and exchange parts are absorbed in ε_a as they do not contribute to the image charge effect.

The screening from the electrodes shifts the pole of the GF from ε_a to the

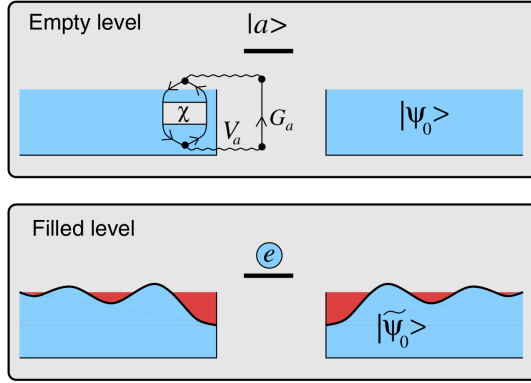


Figure 5.1: Upper panel: When the localized level $|a\rangle$ is empty, the charge distribution corresponding to the electrode ground state, $|\Psi_0\rangle$, is homogeneous (no image charge). Lower panel: When the level is occupied, the potential from the localized electron, $V_a(r)$, induces an image charge in the electrode ground state, $|\tilde{\Psi}_0\rangle$.

quasiparticle energy

$$\varepsilon_a^{QP} = \varepsilon_a + \Delta\varepsilon_{ic}, \Delta\varepsilon_{ic} = Z\Sigma_a(\varepsilon_a) \quad (5.2)$$

where $\Delta\varepsilon_{ic}$ is the image charge shift and $Z = (1 - d\Sigma_a(\varepsilon_a)/d\varepsilon)^{-1}$ is the renormalization factor. The physical meaning of Z is explained later.

Within the GW approximation, the self-energy has the form

$$\Sigma(r, r', \omega) = \frac{i}{2\pi} \int G_0(r, r', \omega + \omega') \bar{W}(r, r', \omega') d\omega', \quad (5.3)$$

where the bare Coulomb interaction ν has been subtracted from dynamically screened Coulomb interaction W : $\bar{W} = W - \nu$. Neglecting the spatial overlap between $|a\rangle$ and the metal states, the relevant matrix element of the screened interaction becomes

$$\bar{W}_a(\omega) = \int \int V_a(r) \chi(r, r', \omega) V_a(r') dr dr', \quad (5.4)$$

where $V_a(r)$ is the potential created by an electron in the states $|a\rangle$,

$$V_a(r) = \int \frac{|\psi_a(r')|^2}{|r - r'|} dr'. \quad (5.5)$$

and χ is the density response function of the metal electrode. Clearly, \bar{W} describes the energy associated with the polarization of the electrode due to the

presence of an electron in $|a\rangle$. A Feynman diagram of the self-energy is shown in Fig. 5.1.

Using the plasmon pole approximation for the response function, the self energy energy can be written as

$$\Sigma_a(\omega) = \frac{A}{\omega - \varepsilon_a - \omega_p + i(\gamma + \gamma_p)}, \quad (5.6)$$

where ω_p and γ_p are the characteristic plasmon energy and spectral width. The constant A can be fixed using the condition in Eq. 5.2 which yields

$$A = \frac{\Delta\varepsilon_{ic}\omega_p^2}{\omega_p - \Delta_{ic}}. \quad (5.7)$$

For a single-level model, the transmission at the Fermi energy can be written as

$$T(E_F) = \frac{(\gamma)^2}{(E_F - \varepsilon_a^{\text{eff}})^2 + (\gamma)^2}, \quad (5.8)$$

where the effective energy level is defined as

$$\begin{aligned} \varepsilon_a^{\text{eff}} &= \varepsilon_a + \text{Re}\Sigma_a(E_F) \\ &= \varepsilon_a + \Delta\varepsilon_{ic} \left(\frac{\omega_p}{|E_F - \varepsilon_a| + \omega_p} \right). \end{aligned} \quad (5.9)$$

The transmission through the interacting level is thus equivalent to transmission through a noninteracting level with energy $\varepsilon_a^{\text{eff}}$. When the image charge formation is fast compared to the average time spent by the electron on the molecule, i.e., when $\omega_p \gg |E_F - \varepsilon_a|$, the effective level equals $\varepsilon_a^{\text{QP}}$ and the static image charge approximation is valid. In the opposite regime where the tunneling time is short compared with the image charge formation, i.e., $\omega_p \ll |E_F - \varepsilon_a|$, the self-energy vanishes and the tunneling electron "sees" the unscreened level ε_a .

The effect of the finite electrode response time is embedded into an effective level model as shown in the Eq. 5.8. However it does not reflect the correct physics since the pole of the Green's function remains at $\varepsilon_a^{\text{QP}}$. Within the quasiparticle approximation, $\Sigma(\omega)$ can be expanded to first order around ε_a , which resulting the transmission function

$$T^{\text{QP}}(\omega) = \frac{(Z\gamma)^2}{(\omega - \varepsilon_a^{\text{QP}})^2 + (Z\gamma)^2}, \quad (5.10)$$

where

$$Z = 1 - \frac{\Delta\varepsilon_{ic}}{\omega_p} \quad (5.11)$$

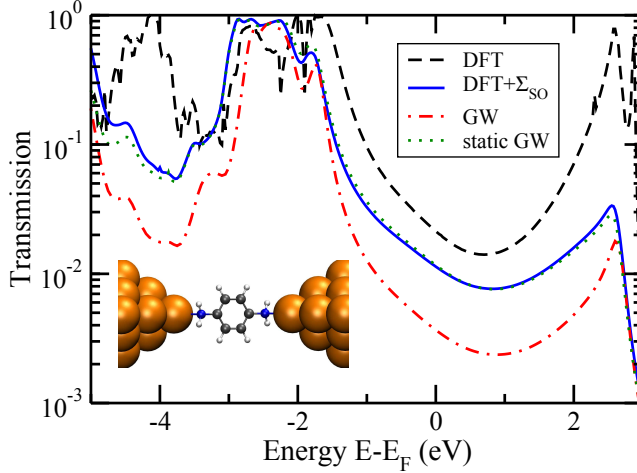


Figure 5.2: The transmission function of the gold/BDA junction calculated using DFT, DFT+ Σ_{SO} , GW and static GW (QPscGW).

is derived from Eq. 5.6 and 5.7. This shows that the transmission resonance remains at ε_a^{QP} , but is narrowed by a factor of Z compared to the noninteracting result. Therefore the conductance is suppressed by a factor of Z^2 in the off-resonant tunneling regime.

To test the role of dynamical screening under more realistic conditions, first-principles GW calculations are performed for the BDA molecule connected to Au electrodes. Fig. 5.2 shows the transmission functions calculated using four different methods. Not surprisingly the DFT method overestimates the conductance because the HOMO is placed too close relative the Fermi level. To isolate the role of dynamical screening, the DFT+ Σ_{SO} is performed where a "scissor operator" is used to match the DFT molecular levels with the GW ones. Additionally QPscGW scheme of Schilfgaarde *et al.*[101] is employed here to perform the static GW calculations. The transmission functions calculated using the QPscGW and DFT+ Σ_{SO} methods are essentially identical. This is because the DFT and QP molecular orbitals coincide, given the low polarizability of BDA.

The observed difference in the transmissions between full GW and DFT+ Σ_{SO} or QPscGW originates from the frequency dependence of the GW self-energy. Fig. 5.3 shows the HF and GW results for the spectral function of the BDA HOMO together with the imaginary and real parts of the GW self-energy. The renormalization factor Z equals to 0.84 obtained from the slope of $\text{Re}\Sigma$. This leads to a conductance reduction by a factor of $Z^2 = 0.71$. The transmission

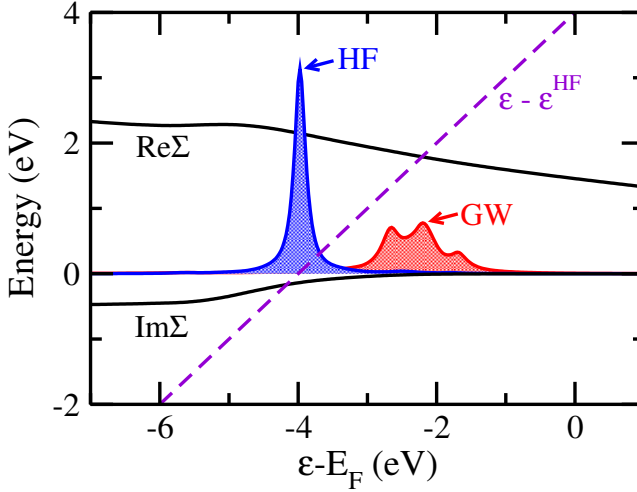


Figure 5.3: The spectral function of the HOMO of the contacted BDA molecule calculated using HF and GW. The real and imaginary parts of the GW self-energy are also shown.

reduction in Fig. 5.2 is not fully accounted by Z^2 , which is probably due to the nontrivial interplay between the dynamical effects on different transport channels.

In conclusion, we have demonstrated that the finite formation time of the image charge can renormalize the coupling strength and therefore suppresses the conductance.

5.2 Simultaneous description of conductance and thermopower

5.2.1 Motivation

From a calculation with an incorrect energy level alignment, it is in principle possible to obtain the correct conductance or thermopower of a single-molecule junction. However a simultaneously good description of conductance and thermopower can hardly be achieved unless the energy level alignment and level broadening are correctly described. To have a highly stringent test of the quality of the underlying electronic structure calculation, it is necessary to conduct a simultaneous modeling of the conductance and thermopower.

In addition, by considering various junction geometries and preferentially comparing to experiments where the conductance and thermopower were measured simultaneously, a faithful benchmark of the GW approximation for electronic transport calculations can be established.

In this study, we apply the GW method to study the conductance and thermopower of a single bis-(4-aminophenyl) acetylene molecule (B4APA) sandwiched between two Au electrodes where the conductance and thermopower of Au/B4APA junctions were simultaneously measured by Widawsky *et al.*[102]. This section is based on Paper V.

5.2.2 Results and discussion

The Au/B4APA molecular junction is shown in Fig. 5.4. To mimic the experimental break junction setup, the break junction simulation is carried out by displacing the two Au electrodes in steps of 0.25 Å. Fig. 5.5 (a) shows that the configuration S0 has the minimum energy which corresponds to the zero-stress configuration in the experiments.

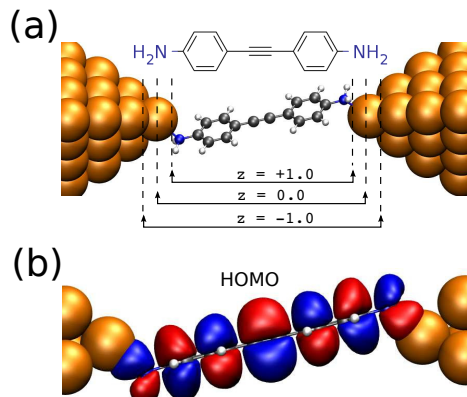


Figure 5.4: (a) A single B4APA molecule is sandwiched between two Au tip electrodes. The three different image plane positions are employed in DFT+ Σ method. (b) The HOMO orbital of the B4APA molecule in the junction.

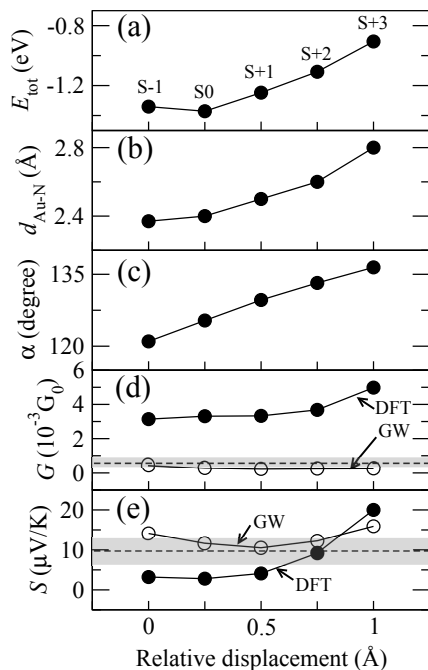


Figure 5.5: When stretching the Au/B4APA junction, the effect on (a) the total energy, (b) the Au-N bond length $d_{\text{Au-N}}$, (c) the angle $\alpha_{\text{Au-N-C}}$ between the Au-N-C atoms, (d) the conductance, and (e) the thermopower. The experimental values are indicated by the gray bars[102].

Fig. 5.5 (d) and (e) show the evolution of the conductance and thermopower calculated using DFT and GW respectively. The DFT conductances are in general a factor of 6 larger than the experimental value, while the DFT thermopower varies from 2.8 to 20 $\mu V/K$. The configuration S+2 has a DFT thermopower close to the experimental value. However it is unlikely to have such configuration in the statistical break junction experiment due to the high total energy. The variation of the DFT conductance and thermopower during the stretching stimulation can be understood in terms of the Lorentzian model, as explained in Paper V. We conclude that the discrepancy between the DFT results and the experimental values are not because of the variation in the junction geometry.

The energy levels of B4APA in the gas phase are listed in the Tab. 5.1 calculated using DFT-PBE Kohn-Sham eigenvalues (PBE-eig), GW, HF and DFT-PBE total energy differences (PBE-tot). In the absence of the experimental reference, the PBE-tot values have been taken as the reference which are found to have an accuracy of around 0.2 eV for the ionization energy for small molecules. The DFT HOMO level is overestimated by 1.9 eV while the DFT LUMO is underestimated by 2.0 eV compared to the PBE-tot. Additionally the HF opens up the DFT the HOMO-LUMO gap from 2.8 eV to 9.4 eV by correcting the self-interaction error in the DFT-PBE functional. Furthermore the GW reduces the HF gap to 7.1 eV by including the correlation effect that is missing in the HF.

Table 5.1: Summary of the HOMO and LUMO energies of the B4APA molecule in the gas-phase and in the junction respectively, calculated using DFT-PBE KS eigenvalues (PBE-eig), GW, HF and DFT-PBE total energy differences (PBE-tot). Units are eV.

Molecule	Orbital	PBE-eig	GW	HF	PBE-tot
Gas-phase	HOMO	-4.4	-5.9	-6.9	-6.3
	LUMO	-1.6	1.2	2.5	0.4
	H-L gap	2.8	7.1	9.4	6.7
Junction	HOMO	-1.4	-2.1	-3.3	N/A
	LUMO	1.5	4.5	6.2	N/A
	H-L gap	2.9	6.6	9.5	N/A

Fig. 5.6 shows the transmission functions calculated using DFT, GW and HF for the zero-stress configuration S0. The calculated conductance and thermopwer are listed in the Tab. 5.2. Compared to the DFT and HF results, the GW results are in excellent agreement with the experiments mainly due to the better energy level alignment at the molecule-metal interface. The HOMO and LUMO levels positions are listed in the Tab. 5.1.

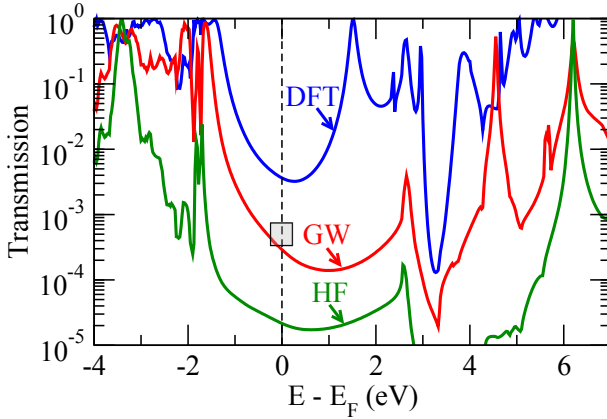


Figure 5.6: Transmission functions for the zero-stress Au/B4APA junction configuration (S0) calculated using DFT-PBE, GW and HF. The experimental conductance[102] is indicated by the gray box and the Fermi level is set to zero eV.

Table 5.2: Conductances and thermopowers for the zero-stress Au/B4APA junction configuration (S0) calculated using DFT-PBE, GW and HF. The experimental values are listed in the last column[102].

	DFT-PBE	GW	HF	Exp.
\mathcal{G} ($10^{-3}G_0$)	3.31	0.29	0.022	0.57 ± 0.2
\mathcal{S} ($\mu V/K$)	2.8	11.6	5.4	9.7 ± 0.3

The image charge induced wave function polarization is negligible in this system due to limited polarizability of the B4APA HOMO orbital. However the effect of finite image charge formation on conductance and thermopower are explored here by comparing the GW calculations with the DFT+ Σ_{SO} calculations. As shown in Fig. 5.7, the GW conductance is a factor of 0.73 lower than the DFT+ Σ_{SO} ones, while the thermopower are essentially identical. The reduction of the GW conductance is related to the quasi-particle renormalization of the HOMO level, as explained in Sec 5.1.

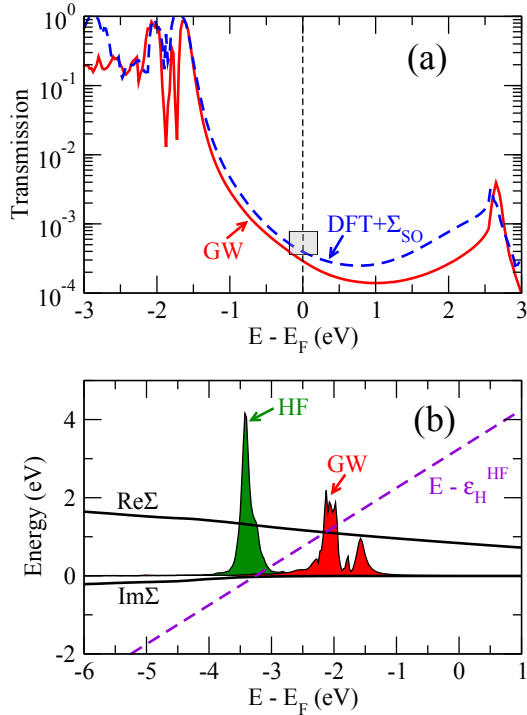


Figure 5.7: (a) Transmission functions calculated using GW and DFT+ Σ_{SO} for the zero-stress Au/B4APA junction configuration (S0). The experimental conductance is indicated by the gray box and the Fermi level is set to zero eV[102]. (b) Spectral functions of the HOMO of the contacted molecule calculated using HF and GW. The black curves show the real and imaginary parts of the GW self-energy.

When electron-electron interactions are described with a GW self-energy, the

transmission of a single level in the wide band limit can be written as

$$\mathcal{T}^{\text{QP}}(E) = \frac{(Z\Gamma)^2}{(E - \varepsilon_a^{\text{QP}})^2 + (Z\Gamma)^2} \quad (5.12)$$

where Γ , Z , $\varepsilon_a^{\text{QP}}$ denote the tunneling width, the renormalization factor and the QP energy level.

In the off-resonance tunneling regime, the conductance can be written as

$$\mathcal{G}^{\text{QP}} \approx \frac{(Z\Gamma)^2}{\varepsilon_a^{\text{QP}2}} G_0 \quad (5.13)$$

For the HOMO level of 4BAPA in the junction, it is found that the renormalization factor of $Z^2 = 0.74$ agrees almost exactly with the ration between the conductance obtained from GW and DFT+ Σ_{SO} . Similarly the thermopower can be written as

$$\mathcal{S}^{\text{QP}} \approx -\frac{\pi^2 k_B^2 T}{3e} \frac{2}{\varepsilon_a^{\text{QP}}}. \quad (5.14)$$

The thermopower turns to be independent of Z , which is consistent with the fact that the thermopowers using GW and DFT+ Σ_{SO} are essentially identical.

Next we address the effect of stretching the Au/B4APA junction on the conductance and thermopower calculated using the DFT+ Σ method, as shown in Fig.5.8. Three different image plane positions, namely $z = +1, 0, -1 \text{ \AA}$ relative to the Au tip atom are employed. It is found that the conductances are greatly improved over the uncorrected DFT results, but the thermopowers are not improved; in fact they are worsened.

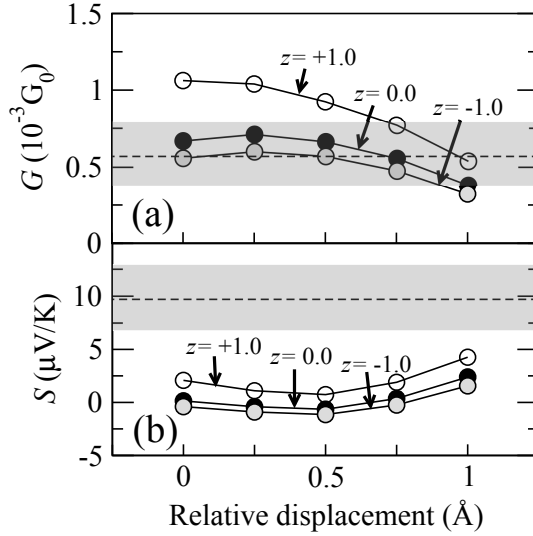


Figure 5.8: When stretching the Au/B4APA junction, the effect on (a) the conductance and (b) the thermopower, calculated from DFT+ Σ method using three different image plane positions, namely $z = +1, 0, -1$ Å relative to the Au tip atom. The broken junction experimental values are indicated by the gray bars[102].

While the DFT conductances remain almost constant during the stretching, the DFT+ Σ conductances are decreasing during the stretching simulation. This is due to the reduction of the image charge effect on the energy level renormalization when the molecule is moving away from the electrodes.

In conclusion, we have demonstrated that a quantitatively simultaneous description of both conductance and thermopower in a gold/B4APA junction is achievable by using the GW approximation to the exchange-correlation functional. The GW method not only provides a better level alignment, but also accounts for the dynamics of the image charge screening which reduces the effective metal-molecule coupling strength.

Bibliography

- [1] G. E. Moore, "Cramming more components onto integrated circuits," *Electronic Magazine*, vol. 38, pp. 114–116, 1965.
- [2] <http://public.itrs.net>, *International Roadmap for Semiconductors (ITRS)*.
- [3] S. Datta, *Quantum Transport: Atom to Transistor*. Cambridge University Press, 2005.
- [4] A. Aviram and M. A. Ratner, "Molecular rectifiers," *Chemical Physics Letters*, vol. 29, pp. 277 – 283, 1974.
- [5] M. Ratner, "A brief history of molecular electronics," *Nat Nano*, vol. 8, p. 378, 2013.
- [6] R. A. Marcus, "Electron transfer reactions in chemistry. theory and experiment," *Rev. Mod. Phys.*, vol. 65, pp. 599–610, 1993.
- [7] G. Cuniberti, G. Fagas, and K. Richter, *Introducing Molecular Electronics: A Brief Overview*. Springer Berlin Heidelberg, 2005.
- [8] J. Cuevas and E. Scheer, *Molecular Electronics: An Introduction to Theory and Experiment*. World Scientific, 2010.
- [9] W. Liang, M. P. Shores, M. Bockrath, J. R. Long, and H. Park, "Kondo resonance in a single-molecule transistor," *Nature*, vol. 417, pp. 725–729, 2002.
- [10] S. Kubatkin, A. Danilov, M. Hjort, J. Cornil, J.-L. Bredas, N. Stuhr-Hansen, P. Hedegard, and T. Bjornholm, "Single-electron transistor of a single organic molecule with access to several redox states," *Nature*, vol. 425, pp. 698–701, 2003.

- [11] P. Sautet and C. Joachim, "Electronic interference produced by a benzene embedded in a polyacetylene chain," *Chemical Physics Letters*, vol. 153, pp. 511 – 516, 1988.
- [12] G. C. Solomon, D. Q. Andrews, T. Hansen, R. H. Goldsmith, M. R. Wasielewski, R. P. Van Duyne, and M. A. Ratner, "Understanding quantum interference in coherent molecular conduction," *The Journal of Chemical Physics*, vol. 129, 2008.
- [13] C. M. Guedon, H. Valkenier, T. Markussen, K. S. Thygesen, J. C. Hummelen, and S. J. van der Molen, "Observation of quantum interference in molecular charge transport," *Nat Nano*, vol. 7, pp. 305–309, 2012.
- [14] S. Schmaus, A. Bagrets, Y. Nahas, T. K. Yamada, A. Bork, M. Bowen, E. Beaurepaire, F. Evers, and W. Wulfhekel, "Giant magnetoresistance through a single molecule," *Nat Nano*, vol. 6, pp. 185–189, 2011.
- [15] M. A. Reed, C. Zhou, C. J. Muller, T. P. Burgin, and J. M. Tour, "Conductance of a molecular junction," *Science*, vol. 278, pp. 252–254, 1997.
- [16] Xiao, Xu, and N. J. Tao, "Measurement of single molecule conductance: Benzenedithiol and benzenedimethanethiol," *Nano Letters*, vol. 4, pp. 267–271, 2004.
- [17] L. Venkataraman, J. E. Klare, I. W. Tam, C. Nuckolls, M. S. Hybertsen, and M. L. Steigerwald, "Single-molecule circuits with well-defined molecular conductance," *Nano Letters*, vol. 6, pp. 458–462, 2006.
- [18] S. V. Aradhya and L. Venkataraman, "Single-molecule junctions beyond electronic transport," *Nat Nano*, vol. 8, p. 399, 2013.
- [19] G. Rubio, N. Agraït, and S. Vieira, "Atomic-sized metallic contacts: Mechanical properties and electronic transport," *Phys. Rev. Lett.*, vol. 76, pp. 2302–2305, 1996.
- [20] B. Xu, X. Xiao, and N. J. Tao, "Measurements of single-molecule electromechanical properties," *Journal of the American Chemical Society*, vol. 125, pp. 16164–16165, 2003.
- [21] D. R. Ward, N. J. Halas, J. W. Ciszek, J. M. Tour, Y. Wu, P. Nordlander, and D. Natelson, "Simultaneous measurements of electronic conduction and raman response in molecular junctions," *Nano Letters*, vol. 8, pp. 919–924, 2008.
- [22] X. H. Qiu, G. V. Nazin, and W. Ho, "Vibrationally resolved fluorescence excited with submolecular precision," *Science*, vol. 299, pp. 542–546, 2003.

- [23] B. Ludoph and J. M. v. Ruitenbeek, "Thermopower of atomic-size metallic contacts," *Phys. Rev. B*, vol. 59, pp. 12290–12293, 1999.
- [24] P. Reddy, S.-Y. Jang, R. A. Segalman, and A. Majumdar, "Thermoelectricity in molecular junctions," *Science*, vol. 315, pp. 1568–1571, 2007.
- [25] W. Lee, K. Kim, W. Jeong, L. A. Zotti, F. Pauly, J. C. Cuevas, and P. Reddy, "Heat dissipation in atomic-scale junctions," *Nature*, vol. 498, pp. 209–212, 2013.
- [26] G. D. Scott and D. Natelson, "Kondo resonances in molecular devices," *ACS Nano*, vol. 4, pp. 3560–3579, 2010.
- [27] M. Born and R. Oppenheimer, "Zur quantentheorie der molekeln," *Annalen der Physik*, vol. 389, pp. 457–484, 1927.
- [28] G. Onida, L. Reining, and A. Rubio, "Electronic excitations: density-functional versus many-body green's-function approaches," *Rev. Mod. Phys.*, vol. 74, pp. 601–659, 2002.
- [29] P. Hohenberg and W. Kohn, "Inhomogeneous electron gas," *Phys. Rev.*, vol. 136, pp. B864–B871, 1964.
- [30] W. Kohn and L. J. Sham, "Self-consistent equations including exchange and correlation effects," *Phys. Rev.*, vol. 140, pp. A1133–A1138, 1965.
- [31] D. M. Ceperley and B. J. Alder, "Ground state of the electron gas by a stochastic method," *Phys. Rev. Lett.*, vol. 45, pp. 566–569, 1980.
- [32] J. P. Perdew, K. Burke, and M. Ernzerhof, "Generalized gradient approximation made simple," *Phys. Rev. Lett.*, vol. 77, pp. 3865–3868, 1996.
- [33] R. Parr and W. Yang, *Density-Functional Theory of Atoms and Molecules*. Oxford University Press, USA, 1994.
- [34] J. Kohanoff, *Electronic Structure Calculations for Solids and Molecules: Theory and Computational Methods*. Cambridge University Press, 2006.
- [35] R. Dreizler and E. Gross, *Density Functional Theory: An Approach to the Quantum Many-Body Problem*. Springer Berlin Heidelberg, 2012.
- [36] J. C. Phillips and L. Kleinman, "New method for calculating wave functions in crystals and molecules," *Phys. Rev.*, vol. 116, pp. 287–294, 1959.
- [37] D. R. Hamann, M. Schlüter, and C. Chiang, "Norm-conserving pseudopotentials," *Phys. Rev. Lett.*, vol. 43, pp. 1494–1497, 1979.
- [38] P. E. Blöchl, "Projector augmented-wave method," *Phys. Rev. B*, vol. 50, pp. 17953–17979, 1994.

- [39] G. Kresse and D. Joubert, "From ultrasoft pseudopotentials to the projector augmented-wave method," *Phys. Rev. B*, vol. 59, pp. 1758–1775, 1999.
- [40] J. J. Mortensen, L. B. Hansen, and K. W. Jacobsen, "Real-space grid implementation of the projector augmented wave method," *Phys. Rev. B*, vol. 71, p. 035109, 2005.
- [41] J. Enkovaara, C. Rostgaard, J. J. Mortensen, J. Chen, M. Duřak, L. Ferrighi, J. Gavnholt, C. Glinsvad, V. Haikola, H. A. Hansen, H. H. Kristoffersen, M. Kuisma, A. H. Larsen, L. Lehtovaara, M. Ljungberg, O. Lopez-Acevedo, P. G. Moses, J. Ojanen, T. Olsen, V. Petzold, N. A. Romero, J. Stausholm-Møller, M. Strange, G. A. Tritsarlis, M. Vanin, M. Walter, B. Hammer, H. Häkkinen, G. K. H. Madsen, R. M. Nieminen, J. K. Nørskov, M. Puska, T. T. Rantala, J. Schiøtz, K. S. Thygesen, and K. W. Jacobsen, "Electronic structure calculations with gpaw: a real-space implementation of the projector augmented-wave method," *Journal of Physics: Condensed Matter*, vol. 22, p. 253202, 2010.
- [42] C. Rostgaard, "The projector augmented-wave method," *ArXiv e-prints*, 2009.
- [43] A. H. Larsen, M. Vanin, J. J. Mortensen, K. S. Thygesen, and K. W. Jacobsen, "Localized atomic basis set in the projector augmented wave method," *Phys. Rev. B*, vol. 80, p. 195112, 2009.
- [44] C. Kittel, *Introduction to solid state physics*. Wiley, 1986.
- [45] H. J. Monkhorst and J. D. Pack, "Special points for brillouin-zone integrations," *Phys. Rev. B*, vol. 13, pp. 5188–5192, 1976.
- [46] S. Datta, *Electronic Transport in Mesoscopic Systems*. Cambridge University Press, 1997.
- [47] H. Bruus and K. Flensberg, *Many-Body Quantum Theory in Condensed Matter Physics: An Introduction*. OUP Oxford, 2004.
- [48] L. V. Keldysh, "Diagram technique for non-equilibrium processes," *JETP*, vol. 20, p. 1018, 1965.
- [49] H. Haug and A. Jauho, *Quantum Kinetics in Transport and Optics of Semiconductors*. Springer London, Limited, 2007.
- [50] L. P. Kadanoff and G. Baym, *Quantum Statistical Mechanics*. Benjamin, 1962.
- [51] Y. Meir and N. S. Wingreen, "Landauer formula for the current through an interacting electron region," *Phys. Rev. Lett.*, vol. 68, pp. 2512–2515, 1992.

- [52] K. S. Thygesen, "Electron transport through an interacting region: The case of a nonorthogonal basis set," *Phys. Rev. B*, vol. 73, p. 035309, 2006.
- [53] L. Hedin, "New method for calculating the one-particle green's function with application to the electron-gas problem," *Phys. Rev.*, vol. 139, pp. A796–A823, 1965.
- [54] F. Guinea, C. Tejedor, F. Flores, and E. Louis, "Effective two-dimensional hamiltonian at surfaces," *Phys. Rev. B*, vol. 28, pp. 4397–4402, 1983.
- [55] K. S. Thygesen and A. Rubio, "Nonequilibrium gw approach to quantum transport in nano-scale contacts," *The Journal of Chemical Physics*, vol. 126, 2007.
- [56] K. S. Thygesen and A. Rubio, "Conserving gw scheme for nonequilibrium quantum transport in molecular contacts," *Phys. Rev. B*, vol. 77, p. 115333, 2008.
- [57] M. Strange, C. Rostgaard, H. Häkkinen, and K. S. Thygesen, "Self-consistent gw calculations of electronic transport in thiol- and amine-linked molecular junctions," *Phys. Rev. B*, vol. 83, p. 115108, 2011.
- [58] G. Baym and L. P. Kadanoff, "Conservation laws and correlation functions," *Phys. Rev.*, vol. 124, pp. 287–299, 1961.
- [59] G. Baym, "Self-consistent approximations in many-body systems," *Phys. Rev.*, vol. 127, pp. 1391–1401, 1962.
- [60] T. Markussen, C. Jin, and K. S. Thygesen, "Quantitatively accurate calculations of conductance and thermopower of molecular junctions," *physica status solidi (b)*, vol. 250, pp. 2394–2402, 2013.
- [61] D. J. Mowbray, G. Jones, and K. S. Thygesen, "Influence of functional groups on charge transport in molecular junctions," *The Journal of Chemical Physics*, vol. 128, 2008.
- [62] S. Y. Quek, L. Venkataraman, H. J. Choi, S. G. Louie, M. S. Hybertsen, and J. B. Neaton, "Amine-gold linked single-molecule circuits: Experiment and theory," *Nano Letters*, vol. 7, pp. 3477–3482, 2007.
- [63] N. D. Lang and W. Kohn, "Theory of metal surfaces: Induced surface charge and image potential," *Phys. Rev. B*, vol. 7, pp. 3541–3550, 1973.
- [64] S. C. Lam and R. J. Needs, "First-principles calculations of the screening of electric fields at the aluminium (111) and (110) surfaces," *Journal of Physics: Condensed Matter*, vol. 5, p. 2101, 1993.

- [65] F. Pauly, J. K. Viljas, and J. C. Cuevas, “Length-dependent conductance and thermopower in single-molecule junctions of dithiolated oligophenylene derivatives: A density functional study,” *Phys. Rev. B*, vol. 78, p. 035315, 2008.
- [66] U. Sivan and Y. Imry, “Multichannel landauer formula for thermoelectric transport with application to thermopower near the mobility edge,” *Phys. Rev. B*, vol. 33, pp. 551–558, 1986.
- [67] K. Esfarjani, M. Zebarjadi, and Y. Kawazoe, “Thermoelectric properties of a nanocontact made of two-capped single-wall carbon nanotubes calculated within the tight-binding approximation,” *Phys. Rev. B*, vol. 73, p. 085406, 2006.
- [68] H. Ness, L. K. Dash, and R. W. Godby, “Generalization and applicability of the landauer formula for nonequilibrium current in the presence of interactions,” *Phys. Rev. B*, vol. 82, p. 085426, 2010.
- [69] M. Paulsson and S. Datta, “Thermoelectric effect in molecular electronics,” *Phys. Rev. B*, vol. 67, p. 241403, 2003.
- [70] J. Taylor, H. Guo, and J. Wang, “*Ab initio* modeling of quantum transport properties of molecular electronic devices,” *Phys. Rev. B*, vol. 63, p. 245407, 2001.
- [71] M. Brandbyge, J.-L. Mozos, P. Ordejón, J. Taylor, and K. Stokbro, “Density-functional method for nonequilibrium electron transport,” *Phys. Rev. B*, vol. 65, p. 165401, 2002.
- [72] Y. Xue, S. Datta, and M. A. Ratner, “First-principles based matrix green’s function approach to molecular electronic devices: general formalism,” *Chemical Physics*, vol. 281, pp. 151 – 170, 2002.
- [73] A. R. Rocha, V. M. García-Suárez, S. Bailey, C. Lambert, J. Ferrer, and S. Sanvito, “Spin and molecular electronics in atomically generated orbital landscapes,” *Phys. Rev. B*, vol. 73, p. 085414, 2006.
- [74] A. J. Cohen, P. Mori-Sánchez, and W. Yang, “Insights into current limitations of density functional theory,” *Science*, vol. 321, pp. 792–794, 2008.
- [75] C. Toher and S. Sanvito, “Efficient atomic self-interaction correction scheme for nonequilibrium quantum transport,” *Phys. Rev. Lett.*, vol. 99, p. 056801, 2007.
- [76] F. Aryasetiawan and O. Gunnarsson, “The gw method,” *Reports on Progress in Physics*, vol. 61, p. 237, 1998.

- [77] C. Rostgaard, K. W. Jacobsen, and K. S. Thygesen, "Fully self-consistent gw calculations for molecules," *Phys. Rev. B*, vol. 81, p. 085103, 2010.
- [78] N. Marom, F. Caruso, X. Ren, O. T. Hofmann, T. Körzdörfer, J. R. Chelikowsky, A. Rubio, M. Scheffler, and P. Rinke, "Benchmark of gw methods for azabenzenes," *Phys. Rev. B*, vol. 86, p. 245127, 2012.
- [79] P. Koval, D. Foerster, and D. Sánchez-Portal, "Fully self-consistent gw and quasiparticle self-consistent gw for molecules," *Phys. Rev. B*, vol. 89, p. 155417, 2014.
- [80] J. Repp, G. Meyer, S. M. Stojković, A. Gourdon, and C. Joachim, "Molecules on insulating films: Scanning-tunneling microscopy imaging of individual molecular orbitals," *Phys. Rev. Lett.*, vol. 94, p. 026803, 2005.
- [81] E. Tsiper, Z. Soos, W. Gao, and A. Kahn, "Electronic polarization at surfaces and thin films of organic molecular crystals: {PTCDA}," *Chemical Physics Letters*, vol. 360, pp. 47 – 52, 2002.
- [82] X. Lu, M. Grobis, K. H. Khoo, S. G. Louie, and M. F. Crommie, "Charge transfer and screening in individual c₆₀ molecules on metal substrates: A scanning tunneling spectroscopy and theoretical study," *Phys. Rev. B*, vol. 70, p. 115418, 2004.
- [83] J. B. Neaton, M. S. Hybertsen, and S. G. Louie, "Renormalization of molecular electronic levels at metal-molecule interfaces," *Phys. Rev. Lett.*, vol. 97, p. 216405, 2006.
- [84] C. Freysoldt, P. Rinke, and M. Scheffler, "Controlling polarization at insulating surfaces: Quasiparticle calculations for molecules adsorbed on insulator films," *Phys. Rev. Lett.*, vol. 103, p. 056803, 2009.
- [85] J. M. Garcia-Lastra, C. Rostgaard, A. Rubio, and K. S. Thygesen, "Polarization-induced renormalization of molecular levels at metallic and semiconducting surfaces," *Phys. Rev. B*, vol. 80, p. 245427, 2009.
- [86] M. Strange and K. Thygesen, "Towards quantitative accuracy in first-principles transport calculations: The gw method applied to alkane/gold junctions," *Beilstein Journal of Nanotechnology*, vol. 2, pp. 746–754, 2011.
- [87] M. Strange and K. S. Thygesen, "Image-charge-induced localization of molecular orbitals at metal-molecule interfaces: Self-consistent gw calculations," *Phys. Rev. B*, vol. 86, p. 195121, 2012.
- [88] C. Jin and K. S. Thygesen, "Dynamical image-charge effect in molecular tunnel junctions: Beyond energy level alignment," *Phys. Rev. B*, vol. 89, p. 041102, 2014.

- [89] L. Venkataraman, Y. S. Park, A. C. Whalley, C. Nuckolls, M. S. Hybertsen, and M. L. Steigerwald, "Electronics and chemistry: Varying single-molecule junction conductance using chemical substituents," *Nano Letters*, vol. 7, pp. 502–506, 2007.
- [90] M. S. Hybertsen, L. Venkataraman, J. E. Klare, A. C. Whalley, M. L. Steigerwald, and C. Nuckolls, "Amine-linked single-molecule circuits: systematic trends across molecular families," *Journal of Physics: Condensed Matter*, vol. 20, p. 374115, 2008.
- [91] S. Y. Quek, H. J. Choi, S. G. Louie, and J. B. Neaton, "Thermopower of aminegold-linked aromatic molecular junctions from first principles," *ACS Nano*, vol. 5, pp. 551–557, 2011.
- [92] T. M. Tritt and M. A. Subramanian, "Thermoelectric materials, phenomena, and applications: A bird's eye view," *MRS Bulletin*, vol. 31, pp. 188–198, 2006.
- [93] P. Murphy, S. Mukerjee, and J. Moore, "Optimal thermoelectric figure of merit of a molecular junction," *Phys. Rev. B*, vol. 78, p. 161406, 2008.
- [94] H. Song, Y. Kim, Y. H. Jang, H. Jeong, M. A. Reed, and T. Lee, "Observation of molecular orbital gating," *Nature*, vol. 462, pp. 1039–1043, 2009.
- [95] C. Li, A. Mishchenko, and T. Wandlowski, "Charge transport in single molecular junctions at the solid/liquid interface," *Topics in Current Chemistry*, vol. 313, pp. 121–188, 2012.
- [96] B. Capozzi, Q. Chen, P. Darancet, M. Kotiuga, M. Buzzeo, J. B. Neaton, C. Nuckolls, and L. Venkataraman, "Tunable charge transport in single-molecule junctions via electrolytic gating," *Nano Letters*, vol. 14, pp. 1400–1404, 2014.
- [97] S. Sanvito, "Molecular spintronics: The rise of spinterface science," *Nat Phys*, vol. 6, pp. 562–564, 2010.
- [98] S. L. Kawahara, J. Lagoute, V. Repain, C. Chacon, Y. Girard, S. Rousset, A. Smogunov, and C. Barreateau, "Large magnetoresistance through a single molecule due to a spin-split hybridized orbital," *Nano Letters*, vol. 12, pp. 4558–4563, 2012.
- [99] S. K. Lee, T. Ohto, R. Yamada, and H. Tada, "Thermopower of benzenedithiol and c60 molecular junctions with ni and au electrodes," *Nano Letters*, vol. 14, pp. 5276–5280, 2014.

-
- [100] S. Y. Quek, M. Kamenetska, M. L. Steigerwald, H. J. Choi, S. G. Louie, M. S. Hybertsen, N. B., and VenkataramanLatha, “Mechanically controlled binary conductance switching of a single-molecule junction,” *Nat Nano*, vol. 4, pp. 230–234, 2009.
- [101] M. van Schilfgaarde, T. Kotani, and S. Faleev, “Quasiparticle self-consistent *gw* theory,” *Phys. Rev. Lett.*, vol. 96, p. 226402, 2006.
- [102] J. R. Widawsky, P. Darancet, J. B. Neaton, and L. Venkataraman, “Simultaneous determination of conductance and thermopower of single molecule junctions,” *Nano Letters*, vol. 12, pp. 354–358, 2012.

Appendix A

Paper I

Energy level alignment and quantum conductance of functionalized metal-molecule junctions: Density functional theory versus GW calculations

C. Jin, M. Strange, T. Markussen, G. C. Solomon, K. S. Thygesen
The Journal of Chemical Physics **139**, 184307 (2013)

Energy level alignment and quantum conductance of functionalized metal-molecule junctions: Density functional theory versus GW calculations

Chengjun Jin,¹ Mikkel Strange,² Troels Markussen,¹ Gemma C. Solomon,² and Kristian S. Thygesen^{1,a)}

¹Center for Atomic-scale Materials Design, Department of Physics, Technical University of Denmark, DK-2800 Kgs. Lyngby, Denmark

²Nano-Science Center and Department of Chemistry, University of Copenhagen, Universitetsparken 5, 2100 Copenhagen Ø, Denmark

(Received 14 June 2013; accepted 28 October 2013; published online 11 November 2013)

We study the effect of functional groups (CH₃, OCH₃, CH₃, Cl, CN, F) on the electronic transport properties of 1,4-benzenediamine molecular junctions using the non-equilibrium Green function method. Exchange and correlation effects are included at various levels of theory, namely density functional theory (DFT), energy level-corrected DFT (DFT+ Σ), Hartree-Fock and the many-body GW approximation. All methods reproduce the expected trends for the energy of the frontier orbitals according to the electron donating or withdrawing character of the substituent group. However, only the GW method predicts the correct ordering of the conductance amongst the molecules. The absolute GW (DFT) conductance is within a factor of two (three) of the experimental values. Correcting the DFT orbital energies by a simple physically motivated scissors operator, Σ , can bring the DFT conductances close to experiments, but does not improve on the relative ordering. We ascribe this to a too strong pinning of the molecular energy levels to the metal Fermi level by DFT which suppresses the variation in orbital energy with functional group. © 2013 AIP Publishing LLC. [<http://dx.doi.org/10.1063/1.4829520>]

A single molecule connected to source and drain electrodes through well defined chemical bonds constitutes an ideal system for exploring (coherent) charge and heat flow within a molecule and across a metal-molecule interface.^{1,2} Understanding the electronic structure of metal-molecule interfaces, and in particular the energy level alignment and interface conductance, is essential for the development of accurate models in several research fields including organic photovoltaics,³ (photo-)electrochemical reactions^{4,5} and molecular electronics,⁶ which all involve charge flow across a metal-molecule interface as a key element.

Molecular transport junctions are also interesting in their own right. A variety of fascinating phenomena, including strong correlation Kondo physics,^{7,8} electrostatic gate control,^{7,9} magnetic switching,^{10,11} and quantum interference,^{12–14} have recently been demonstrated at the single-molecule level. However, the most unique property of molecular junctions, which continues to drive new discoveries in the field, is the vast degree of flexibility in the design of molecular components providing atomic-scale handles on the electronic properties.^{15–17} The main problem is the lack of atomic-scale control of the metal-molecule interface. Amine anchoring groups have shown promise in some experimental testbeds, offering well defined and reproducible electronic properties.

The effect of chemical modifications of the 1,4-benzenediamine (BDA) molecule on the electrical conduc-

tance has been studied experimentally by Venkataraman *et al.*¹⁶ It was shown that the conductance can be tuned, to some extent, by functionalizing the BDA molecule with different side groups. The conductance of BDA is mainly dominated by the highest occupied molecular orbital (HOMO). The HOMO energy level will be shifted up in energy by the introduction of an electron donating (ED) group and down in energy by an electron withdrawing (EW) group. While the effect of different functional groups only lead to relatively small changes in the conductance it still provides an interesting testbed for a theoretical description of the energy level alignment and electronic transport through the molecules. We note in passing that functional side groups can lead to much larger relative conductance changes in molecules showing destructive quantum interference effects, either by tuning or switching on/off the interference effect.^{13,14,18}

DFT calculations have previously been performed to investigate the effect of different functional groups on the BDA conductance.¹⁹ Due to the self-interaction error in standard (semi-)local exchange-correlation (xc) functionals, the HOMO level lies too high in energy, and the conductance is typically overestimated by up to several orders of magnitude. This discrepancy has been corrected to some extent by the DFT+ Σ method.^{19–22} In this method, the positions of the HOMO and LUMO levels are rigidly shifted to correct for the error in the approximate xc functionals. The shift corrects the energy levels for the free molecule in the gas-phase, for which accurate numbers are available, and includes an image charge correction to account for the screening by the electrodes. The

^{a)}Electronic mail: thygesen@fysik.dtu.dk

latter is estimated using a classical electrostatic model, which depends on the positions of two image planes as adjustable parameters. Self-interaction errors and image charge screening could, in principle, also affect the shape of molecular orbitals which thus influence the metal-molecule coupling strength and the broadening of molecular resonances.²³ More recently, the self-consistent GW method has been successfully applied to calculate the conductance of several small molecules.^{24–26} It has been demonstrated that the GW scheme, without adjustable parameters, provides quantitative agreement with the experiments for both conductance^{25,26} and thermopower.²⁷

In this paper, we address the effect of functional groups on the conductance of gold/BDA junctions using the non-equilibrium Green's function method (NEGF) with different levels of theory to describe exchange-correlation (xc) effects. The DFT+ Σ method improves on DFT-PBE and yields conductances within a factor 2 of the experimental results for certain positions of the image planes. However, both DFT-PBE and DFT+ Σ fail to capture the trends in the conductance observed in experiment and expected from the electron donating or withdrawing character of the functional group. Hartree-Fock (HF) underestimates the conductance by a factor of 20 and also fails to capture the conductance trends. We find that only the GW method predicts both the trend, that is, the relative ordering of conductance amongst the BDA functionalized molecules, as well as the overall magnitude of the conductance in good agreement with experiments.

All the calculations are performed with the GPAW code²⁸ using the projector-augmented wave method and a numerical atomic orbitals basis set.²⁹ We use a double zeta with polarization (DZP) basis for Au and a double zeta (DZ) basis for the molecules. We use rather diffuse basis functions for Au corresponding to an energy shift of 0.01 eV. This is essential to obtain a good description of the surface dipole, which is important for a correct alignment of molecular energy levels. With the present basis set, we obtain a work function of 5.4 eV for the flat Au(111) surface in good agreement with the experimental value of 5.31 eV.³⁰ The molecules are sandwiched between two four-atom Au tips attached to Au(111) surface as illustrated in Fig. 1(a). The supercell contains eight 4×4 Au(111) atomic layers. The geometries of the molecular junctions are optimised by relaxing the molecule and four atom tips until the residual force on any atom is less than 0.01 eV/Å. For the relaxation, we use the PBE³¹ functional and a $4 \times 4 \times 1$ k-point sampling. The HF and GW transport calculations are performed according to the method described in Ref. 24. The transmission is calculated from the Landauer formula^{32,33}

$$T(\epsilon) = \text{Tr}[G^r(\epsilon)\Gamma_L(\epsilon)G^a(\epsilon)\Gamma_R(\epsilon)], \quad (1)$$

where the retarded Green's function is obtained from

$$G^r(E) = [(E + i\eta)S - H_0 + V_{xc} - \Delta V_H[G] - \Sigma_L^r(E) - \Sigma_R^r(E) - \Sigma_{xc}[G](E)]^{-1}. \quad (2)$$

Here S , H_0 , and V_{xc} are the overlap matrix, Kohn-Sham (KS) Hamiltonian matrix and the PBE xc-potential in the atomic orbital basis, respectively. η is a numerical positive infinitesimal which is set to 0.02 eV in all the calculations. $\Sigma_{L/R}^r$ are

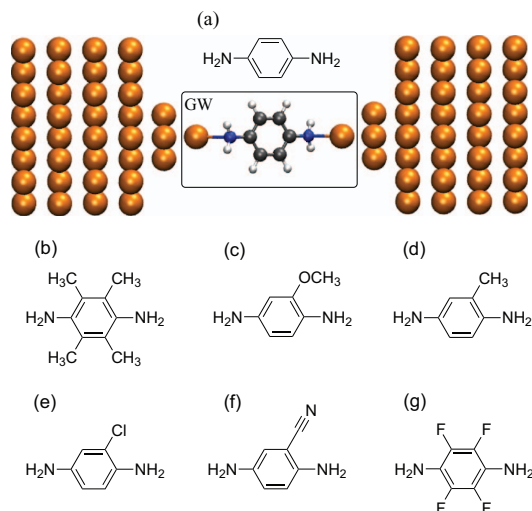


FIG. 1. (a) The atomic structure of the gold/BDA junction. The amine linkers connect the benzene ring to the gold electrodes via two 3-fold coordinated gold atoms. The black box indicates the region where the GW self-energy is evaluated self-consistently. The other structures considered are constructed by replacing BDA by (b) BDA+CH₃*4, (c) BDA+OCH₃, (d) BDA+OCH₃*4, (e) BDA+Cl, (f) BDA+CN, (g) BDA+F*4.

the retarded lead self-energies and ΔV_H is the deviation of the Hartree potential from the equilibrium DFT-PBE value. Σ_{xc} is the many-body xc self-energy. For HF and GW, Σ_{xc} is the non-local Fock exchange potential and the GW self-energy, respectively. These self-energies are evaluated self-consistently for atomic orbitals centered on atoms within the box region in Fig. 1(a). A standard NEGF-DFT calculation is recovered when Σ_{xc} is taken as KS xc-potential, V_{xc} . The self-consistent cycle is performed by a linear mixing of the Green functions. The energy dependent quantities are represented on an energy grid ranging from -160 eV to 160 eV with an energy-grid spacing of 0.01 eV.

In the DFT+ Σ method an orbital dependent self-energy term Σ is included to shift the molecular orbital energies.^{19–22} The self-energy term Σ has the form $\sum_n \Delta_n |\psi_n\rangle \langle \psi_n|$, where $\Delta_n = \Delta_{occ}$ for all the occupied states and $\Delta_n = \Delta_{unocc}$ for all the unoccupied states. The states $|\psi_n\rangle$ are the molecular orbitals calculated by diagonalizing the molecular part of the DFT Hamiltonian for the junction. The energy shift Δ_{occ} has two contributions: A correction obtained as the difference between the Kohn-Sham HOMO energy and the vertical ionisation potential (IP) of the molecule in the gas-phase. The IP is evaluated from a Δ SCF calculation involving the PBE ground state energies of the neutral and cation species, i.e., $IP = E(N-1) - E(N)$. This term mainly corrects for self-interaction errors and moves the occupied states down by 2–3 eV. Likewise, Δ_{unocc} corrects the LUMO to fit the electron affinity $EA = E(N) - E(N+1)$ and moves the unoccupied states up in energy. Second, we include a classical image charge correction due to the screening from the metal electrodes of the HOMO and LUMO charge densities. This correction relies on the assumption that screening by the Au electrodes can be described

classically as two flat conductors characterised by two image planes, the positions of which are adjustable parameters. The image planes are placed symmetrically in the junction. We consider three different positions of the image plane relative to the tip gold atom, namely, $z = -1.0, 0.0, +1.0$ Å.

The junction atomic structure and the functionalized BDA molecules investigated are shown in Fig. 1. For all the junctions, we observe very small structural variations at the contact interface due to the side group substitution. The average Au-N bond length is 2.55 Å with standard deviation (STD) of 0.026 Å and the average Au-N-C angle is 130.4° with STD of 3.1°. It is known, both experimentally and theoretically, that the conductance is relatively insensitive to the contact geometry for amine-linked junctions.^{20,34} Previous calculations also show that, for the most stable configurations, the conductance remains essentially constant when the Au-N bond length is changed by up to 0.05 Å.³⁵ Since the STD of the Au-N bond length obtained for the molecules is only 0.026 Å, we conclude that the origin of the conductance variation observed for the functionalized junctions is an electronic rather than a structural effect.

The transmission functions for the unsubstituted BDA junction calculated using DFT-PBE, HF, and GW are shown in Figs. 2(a) and 2(b) shows a zoom of the transmission of all the different functionalized BDA junctions around the Fermi energy on a logarithmic scale. For each method, we find that the functional group only induces small changes in the shape and value of the transmission around the Fermi energy. This indicates that the effect of functional group on conductance is weak, in agreement with the experiment. In all cases, the Fermi level is crossing the tail of a HOMO resonance peak, indicating that the HOMO level is mediating the charge transport. We note that the slope of the transmission function at the Fermi energy is an indicator for the Seebeck coefficient. The negative slope signals HOMO-mediated transport in agreement with measurements of the Seebeck coefficient of gold BDA junctions.²²

The positions of the HOMO resonance in the junction and in the gas-phase are shown in Figs. 3(a) and 3(b), respectively. In addition, we show the results obtained with the DFT+ Σ approach. To define the HOMO level position in the junction we have used the position of the first transmis-

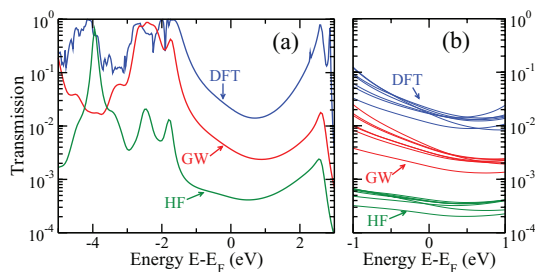


FIG. 2. (a) The transmission function for the unsubstituted BDA junction calculated by DFT-PBE (blue), Hartree-Fock (green), and the self-consistent GW approximation (red). (b) The transmission functions for the different functionalized BDA junctions.

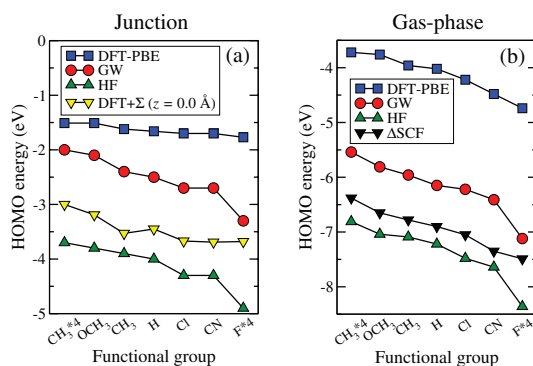


FIG. 3. (a) The HOMO positions relative to the Fermi level of different functionalized BDA junctions calculated by using DFT-PBE (blue), HF (green), the self-consistent GW approximation (red), and DFT+ Σ (yellow). The position of the HOMO is taken as the first transmission peak below the Fermi level. (b) HOMO level positions in the gas-phase relative to the vacuum level.

sion peak below the Fermi level reaching a value of 0.8–1. The functional groups have been ordered according to their electron donating/withdrawing nature with the most donating groups to the left and most withdrawing groups to the right. The position of the HOMO level is seen to follow this trend both in the junction and the gas-phase.

Focusing on the gas-phase, we see that although all methods give the same trend for the HOMO level position, there are considerable differences both in the absolute values as well as the relative differences between the molecules. Taking either GW or Δ SCF as a reference, the DFT-PBE levels are typically overestimated by 2–3 eV while HF underestimates by 0.5–1 eV. The large overestimation of the HOMO level by DFT-PBE can be explained by the spurious self-interaction. In contrast, the self-interaction free HF approximation underestimates the HOMO due to the missing correlation. All methods predict similar trends for the dependence of the HOMO energy on the functional group, except for the F*4 group where DFT+ Σ and DFT-PBE predict give much smaller change than HF and GW.

We note that the GW results for the IPs lie around 1 eV above the IPs predicted by the Δ SCF method. For BDA, the IP predicted by GW (6.2 eV) is 1–1.5 eV smaller than the experimental vertical IP which lies in the range 7.3–7.6 eV.³⁶ Thus, it seems that the gas-phase IPs obtained with GW are on the order 1 eV too small for the present set of molecules. This is somewhat larger than that reported previously by some of us for a test set of 34 small molecules (mean deviation from experiments of 0.4 eV).³⁷ We ascribe this difference to the different basis sets employed. In Ref. 37 we used a DZP basis set comprising maximally localized Wannier functions constructed from a highly accurate real space grid DFT calculation augmented by numerical atomic orbitals, whereas the present calculations are performed with a DZ basis of numerical atomic orbitals. We further note that previous plane wave G_0W_0 calculations found an IP for BDA of 7.0 eV.³⁸ This result is more consistent with the mean deviation of 0.4 eV reported in Ref. 37 and indicates that our present basis set is not

TABLE I. Summary of conductances (in units of $10^{-3}G_0$) obtained with DFT-PBE, GW, Hartree-Fock, and DFT+ Σ for different image plane positions, namely $z = -1.0, 0.0, +1.0$ Å relative to the Au tip atom. The experimental conductances are listed in the last column.¹⁶

	Effect	DFT	GW	HF	DFT+ Σ			Expt.
					-1.0 Å	0.0 Å	+1.0 Å	
CH ₃ *4	donor	17.2	4.15	0.337	4.41	6.24	10.79	8.2 ± 0.2
OCH ₃	donor	19.6	3.85	0.385	3.37	4.26	6.23	6.9 ± 0.2
CH ₃	donor	18.2	3.76	0.393	3.16	3.77	5.81	6.4 ± 0.6
H		21.3	3.67	0.459	3.57	4.51	6.69	6.4 ± 0.2
Cl	acceptor	17.2	3.19	0.384	3.35	3.88	5.90	6.0 ± 0.4
CN	acceptor	16.7	2.91	0.343	3.05	3.52	5.29	6.0 ± 0.3
F*4	acceptor	11.3	1.74	0.225	3.42	4.13	6.65	5.5 ± 0.3

fully converged for gas-phase calculations. We would like to stress, however, that the accuracy of our GW calculations are expected to be higher for the molecules in the junction than for the gas-phase. This is because in the junction, the screened interaction entering the GW self-energy is dominated by the response function of the gold electrodes. The latter is mainly determined by low-energy transitions ($s - s$ intraband and $s - d$ interband transitions), which are well represented by our DZP basis set. The last point follows from the excellent agreement between the band structure of bulk gold obtained with our DZP basis and a plane wave basis set (not shown). Moreover, it is our experience that standard G_0W_0 quasiparticle calculations for metallic systems converge much faster with respect to plane wave cut-off than calculations for isolated molecules. Based on this we expect our GW calculations for the contacted molecules to be less sensitive to the finite basis set than the gas-phase calculations.

The general trends in the HOMO level position observed in the gas-phase are also seen for the contacted molecules, see Fig. 3(a). The relative HOMO resonance position in the junction with GW and HF is almost unchanged from the gas-phase and still shows a variation of around 1.5 eV. However, with DFT-PBE the HOMO resonance position varies much less with the functional group compared to the gas-phase and shows a total variation of only 0.25 eV. We ascribe this to a stronger pinning of the HOMO to the Fermi level in the DFT-PBE calculations. The stronger pinning results from the larger overlap of the HOMO resonance with the Fermi level in DFT and from the spurious self-interaction which enhances the effective fields making it energetically more difficult for charge to flow to/from the HOMO. Additionally, the DFT+ Σ inherits the strong pinning in DFT and therefore shows a small total variation of 0.7 eV.

We note that the DFT-PBE levels are in general closer to the GW levels in the junction than in the gas-phase. This is a result of the enhanced screening by the metal electrodes which pushes the HOMO level upwards in energy when the molecule is placed in the junction.^{39,40} This effect is completely missed by Hartree-Fock and DFT. However, our GW method naturally captures this feature, which can be seen from the increased distance between the GW and HF levels when going from the gas-phase to the junction in Fig. 3. For the functionalized BDA junctions, the image charge shift amounts to around 0.4 eV on average.

The calculated zero-bias conductances obtained from $G = G_0T(E_F)$, where $G_0 = 2e^2/h$ is the conductance quantum, are shown in Fig. 4. The corresponding values are listed in Table I. We find that DFT-PBE overestimates the experimental conductances by a factor of 3, while HF underestimates the experimental conductances by a factor of 20. Inclusion of screening at the GW level brings the conductances closer to experimental values, but the method still underestimates the experimental values by a factor of 2.

Interestingly, only GW correctly predicts the relative effect of the functional groups. Specifically, functional groups with donor characteristic such as CH₃*4, OCH₃, and CH₃ increase the conductance, while functional groups with acceptor characteristic such as Cl, CN, and F*4 decrease the conductance. Although the variations in conductance are small, they correlate well with the variations in the HOMO positions and with the expected effects of the side groups. In the case of DFT, although the changes of the DFT HOMO positions follow the ED and EW effects of the substituent groups, the conductances do not follow this trend. From Fig. 3, as already mentioned, the changes of the DFT HOMO positions are relatively small compared to the GW results due to the stronger effect of pinning to the metal Fermi level. Consequently, the variation in the DFT conductance is more sensitive to other

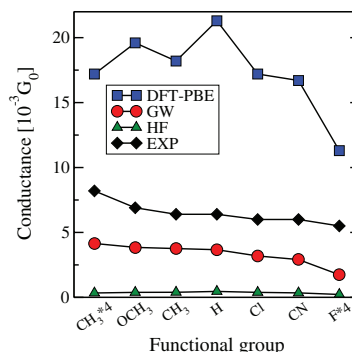


FIG. 4. Conductance of side group functionalized BDA junctions calculated with DFT-PBE (blue), Hartree-Fock (green), and self-consistent GW (red). The experimental conductances are shown in black.

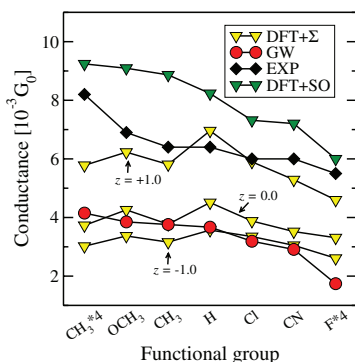


FIG. 5. Conductance of the functionalized BDA junctions calculated using the DFT+ Σ method (yellow) with three different image plane positions, namely, $z = -1.0, 0.0, +1.0$ Å relative to the Au tip atom, compared with the GW (red), DFT+SO (green), and experimental (black) results. Note in DFT+SO method, the positions of DFT HOMO and LUMO levels are shifted with a scissor operator to match the positions of GW HOMO and LUMO levels.

effects, such as the variation in the coupling strengths, and does not reflect the (small) variation in the level positions.

In Fig. 5, we compare the DFT+ Σ results with GW and experimental values. The conductances of the $z = +1.0$ Å image plane position gives results in overall best agreement with the experimental values. Shifting the image planes further away from the molecule by $z = -1.0$ Å or $z = 0.0$ Å reduces the image charge energies. This implies that the molecular levels are shifted away from the Fermi level, and the conductances are lowered to values closer to the GW results. While the DFT+ Σ results are in overall good agreement with the experiments, the changes in conductance with different side groups are not correctly captured by this method. Interestingly, if the positions of the DFT HOMO and LUMO levels are shifted using a scissor operator (DFT+SO) to match the positions of GW HOMO and LUMO levels, the correct ordering of the conductance is recovered. We note in passing that the relative conductance difference between the DFT+SO and GW is related to the frequency dependence of the GW self-energy which is absent in DFT+SO.⁴¹ The DFT+SO results further support the interpretation that the wrong ordering of the conductances in DFT and DFT+ Σ is a consequence of incorrect level alignment.

In their original work Venkataraman *et al.* explored the connection between the change induced by a side group on the tunnel conductance and reaction rate of the BDA, respectively.¹⁶ To this end, they plotted the log of the ratio of the measured conductance for the substituted (G_X) and unsubstituted (G_H) molecule scaled by the number of substituents on the ring against the Hammett parameter σ_{para} . In Fig. 6 we have made a similar plot comparing our calculated data with the measured data from Ref. 16 and taking Hammett constants from Ref. 42. Overall, there is a good agreement between the GW and experimental data sets. In particular, the clear trend that the conductance decreases as the Hammett constant is made more positive is well reproduced by GW. In contrast the DFT results do not show this trend. The non-additive depen-

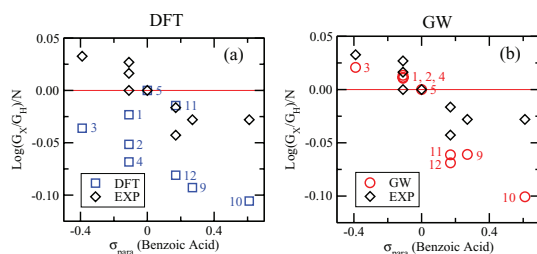


FIG. 6. Logarithm of the ratio of the functionalized molecule conductance (G_X) to the BDA conductance (G_H) divided by the number of side groups (N) in each molecule against the Hammett σ_{para} coefficient from Ref. 42. (a) DFT calculations. (b) GW calculations. Note that the labels used for the molecules follow Ref. 16 for the ease of comparison.

dence on the number of substituent groups (labels 1,2,4 for methyl and 11,12 for fluorine) is, however, not well accounted for by GW which underestimates the change in conductance with the number of groups compared with experiments.

The results presented above demonstrate a quantitative agreement between experiments and self-consistent GW transport calculations. Although the GW conductances are still around a factor of two lower than the experiments, the agreement is indeed satisfactory given the statistical variations in the metal-molecule linker structure, solvent, and temperature effects. In a recent study we have investigated the influence of structural effects on the BDA conductance.²⁷ At the level of DFT+ Σ we found that the conductance varied by about a factor of two for different junction geometries in agreement with previous work,²⁰ and similar structure-induced variation are expected at the GW level. In contrast to the DFT-based calculations, the variations in GW conductance for different side groups follow the experimental trends as well as the variations in the HOMO position as expected from the donating/accepting character of the functional groups.

We have found that the DFT+ Σ method gives conductance values in close agreement with experiment for image plane positions at $z = +1.0$ Å. On the other hand, the closer agreement with the more accurate GW calculations for $z = 0.0$ Å or $z = -1.0$ Å might just as well suggest that these are more correct positions of the image planes. More importantly, both DFT and DFT+ Σ show, irrespective of image plane positions, a very similar relative ordering of the conductance, although the absolute position of the frontier energy levels are rather different in the two methods. This is a consequence of the strong pinning of the DFT molecular resonances to the metal Fermi level an effect which is inherited by the DFT+ Σ method.

In conclusion, we have explored the role of energy level alignment for a correct description of the electronic conductance of side group functionalized benzene-diamine molecular junctions. The self-consistent GW method was found to yield excellent agreement with experiments for both qualitative trends and absolute conductance values. In contrast, standard DFT as well as the scissors operator corrected DFT+ Σ method failed to reproduce the relative variation in

conductance with functional group. This result could be explained by incorrect energy level alignment predicted by DFT due to over-pinning of the molecular levels to the metal Fermi level.

ACKNOWLEDGMENTS

T.M. acknowledges support from the Danish Council for Independent Research, FTP Grant Nos. 11-104592 and 11-120938. K.S.T. and C.J. acknowledge support from the Danish Council for Independent Research, FTP Sapere Aude Grant No. 11-1051390. G.C.S. and M.S. received funding from the European Research Council under the European Union's Seventh Framework Programme (FP7/2007-2013)/ERC Grant agreement No. 258806.

- ¹C. Joachim, J. K. Gimzewski, and A. Aviram, *Nature (London)* **408**, 541 (2000).
- ²Y. Dubi and M. DiVentra, *Rev. Mod. Phys.* **83**, 131 (2011).
- ³J.-L. Brdas, J. E. Norton, J. Cornil, and V. Coropceanu, *Acc. Chem. Res.* **42**, 1691 (2009).
- ⁴I. E. Castellì, D. D. Landis, K. S. Thygesen, S. Dahl, I. Chorkendorff, T. F. Jaramillo, and K. W. Jacobsen, *Energy Environ. Sci.* **5**, 9034 (2012).
- ⁵I. E. Castellì, T. Olsen, S. Datta, D. D. Landis, S. Dahl, K. S. Thygesen, and K. W. Jacobsen, *Energy Environ. Sci.* **5**, 5814 (2012).
- ⁶K. Moth-Poulsen and T. Bjørnholm, *Nat. Nanotechnol.* **4**, 551 (2009).
- ⁷S. Kubatkin, A. Danilov, M. Hjort, J. Cornil, J.-L. Bredas, N. Stühr-Hansen, P. Hedegard, and T. Bjørnholm, *Nature (London)* **425**, 698 (2003).
- ⁸W. Liang, M. P. Shores, M. Bockrath, J. R. Long, and H. Park, *Nature (London)* **417**, 725 (2002).
- ⁹H. Song, Y. Kim, Y. H. Jang, H. Jeong, M. A. Reed, and T. Lee, *Nature (London)* **462**, 1039 (2009).
- ¹⁰S. Sanvito, *Chem. Soc. Rev.* **40**, 3336 (2011).
- ¹¹M. Diefenbach and K. Kim, *Angew. Chem., Int. Ed.* **46**, 7640 (2007).
- ¹²P. Sautet and C. Joachim, *Chem. Phys. Lett.* **153**, 511 (1988).
- ¹³D. Q. Andrews, G. C. Solomon, R. P. Van Duyne, and M. A. Ratner, *J. Am. Chem. Soc.* **130**, 17309 (2008).
- ¹⁴C. M. Guedon, H. Valkenier, T. Markussen, K. S. Thygesen, J. C. Hummel, and S. J. van der Molen, *Nat. Nanotechnol.* **7**, 305 (2012).
- ¹⁵L. Venkataraman, C. Nuckolls, M. S. Hybertsen, and M. L. Steigerwald, *Nature (London)* **442**, 904 (2006).
- ¹⁶L. Venkataraman, Y. S. Park, A. C. Whalley, C. Nuckolls, M. S. Hybertsen, and M. L. Steigerwald, *Nano Lett.* **7**, 502 (2007).
- ¹⁷A. Mishchenko, D. Vonlanthen, V. Meded, M. Brkle, C. Li, I. V. Pobelov, A. Bagrets, J. K. Viljas, F. Pauly, F. Evers *et al.*, *Nano Lett.* **10**, 156 (2010).
- ¹⁸T. Markussen, R. Stadler, and K. S. Thygesen, *Nano Lett.* **10**, 4260 (2010).
- ¹⁹D. J. Mowbray, G. Jones, and K. S. Thygesen, *J. Chem. Phys.* **128**, 111103 (2008).
- ²⁰S. Y. Quek, L. Venkataraman, H. J. Choi, S. G. Louie, M. S. Hybertsen, and J. B. Neaton, *Nano Lett.* **7**, 3477 (2007).
- ²¹S. Y. Quek, H. J. Choi, S. G. Louie, and J. B. Neaton, *Nano Lett.* **9**, 3949 (2009).
- ²²S. Y. Quek, H. J. Choi, S. G. Louie, and J. B. Neaton, *ACS Nano* **5**, 551 (2011).
- ²³M. Strange and K. S. Thygesen, *Phys. Rev. B* **86**, 195121 (2012).
- ²⁴K. S. Thygesen and A. Rubio, *Phys. Rev. B* **77**, 115333 (2008).
- ²⁵M. Strange, C. Rostgaard, H. Häkkinen, and K. S. Thygesen, *Phys. Rev. B* **83**, 115108 (2011).
- ²⁶M. Strange and K. S. Thygesen, *Beilstein J. Nanotechnol.* **2**, 746 (2011).
- ²⁷T. Markussen, C. Jin, and K. S. Thygesen, "Quantitatively accurate calculations of conductance and thermopower of molecular junctions," *Phys. Status Solidi B* (published online).
- ²⁸J. Enkovaara, C. Rostgaard, J. J. Mortensen, J. Chen, M. Dulak, L. Ferrighi, J. Gavnholt, C. Glinsvad, V. Haikola, H. A. Hansen *et al.*, *J. Phys.: Condens. Matter* **22**, 253202 (2010).
- ²⁹A. H. Larsen, M. Vanin, J. J. Mortensen, K. S. Thygesen, and K. W. Jacobsen, *Phys. Rev. B* **80**, 195112 (2009).
- ³⁰H. B. Michaelson, *J. Appl. Phys.* **48**, 4729 (1977).
- ³¹J. P. Perdew, K. Burke, and M. Ernzerhof, *Phys. Rev. Lett.* **77**, 3865 (1996).
- ³²Y. Meir and N. S. Wingreen, *Phys. Rev. Lett.* **68**, 2512 (1992).
- ³³K. S. Thygesen, *Phys. Rev. B* **73**, 035309 (2006).
- ³⁴L. Venkataraman, J. E. Klare, I. W. Tam, C. Nuckolls, M. S. Hybertsen, and M. L. Steigerwald, *Nano Lett.* **6**, 458 (2006).
- ³⁵M. S. Hybertsen, L. Venkataraman, J. E. Klare, A. C. Whalley, M. L. Steigerwald, and C. Nuckolls, *J. Phys.: Condens. Matter* **20**, 374115 (2008).
- ³⁶See <http://webbook.nist.gov/cgi/cbook.cgi?ID=C106503&Units=SI&Mask=20#Ion-Energetics> for gas phase ion energetics data (accessed 13 June 2013).
- ³⁷C. Rostgaard, K. W. Jacobsen, and K. S. Thygesen, *Phys. Rev. B* **81**, 085103 (2010).
- ³⁸I. Tamblyn, P. Darancet, S. Y. Quek, S. A. Bonev, and J. B. Neaton, *Phys. Rev. B* **84**, 201402 (2011).
- ³⁹J. B. Neaton, M. S. Hybertsen, and S. G. Louie, *Phys. Rev. Lett.* **97**, 216405 (2006).
- ⁴⁰J. M. Garcia-Lastra, C. Rostgaard, A. Rubio, and K. S. Thygesen, *Phys. Rev. B* **80**, 245427 (2009).
- ⁴¹C. J. Jin and K. S. Thygesen, "Dynamical image charge effect in electron tunneling beyond energy level alignment," e-print [arXiv:1311.0163v1](https://arxiv.org/abs/1311.0163v1) (unpublished).
- ⁴²C. Hansch, A. Leo, and R. W. Taft, *Chem. Rev.* **91**, 165 (1991).

Paper II**Quantitatively accurate calculations of conductance and thermopower of molecular junctions**

T. Markussen, [C. Jin](#), K. S. Thygesen

Physica Status Solidi (b) **250**, 2394 (2013)

Quantitatively accurate calculations of conductance and thermopower of molecular junctions

Troels Markussen*, Chengjun Jin, and Kristian S. Thygesen

Department of Physics, Center for Atomic-scale Materials Design (CAMD), Technical University of Denmark, 2800 Kgs. Lyngby, Denmark

Received 13 May 2013, revised 5 August 2013, accepted 5 August 2013

Published online 3 September 2013

Keywords conductance, first-principles calculations, molecular junctions, thermopower

*Corresponding author: e-mail trma@fysik.dtu.dk, Phone: +45 4525 3234, Fax: +45 4593 2399

Thermopower measurements of molecular junctions have recently gained interest as a characterization technique that supplements the more traditional conductance measurements. Here we investigate the electronic conductance and thermopower of benzenediamine (BDA) and benzenedicarbonitrile (BDCN) connected to gold electrodes using first-principles calculations. We find excellent agreement with experiments for both molecules when exchange–correlation effects are described by the many-body GW approximation. In contrast, results from standard density functional theory (DFT) deviate from experiments by up to two orders of magnitude. The failure of DFT

is particularly pronounced for the n-type BDCN junction due to the severe underestimation of the lowest unoccupied molecular orbital (LUMO). The quality of the DFT results can be improved by correcting the molecular energy levels for self-interaction errors and image charge effects. Finally, we show that the conductance and thermopower of the considered junctions are relatively insensitive to the metal–molecule bonding geometry. Our results demonstrate that electronic and thermoelectric properties of molecular junctions can be predicted from first-principles calculations when exchange–correlation effects are taken properly into account.

© 2013 WILEY-VCH Verlag GmbH & Co. KGaA, Weinheim

1 Introduction Molecular junctions in which one or several molecules are connected to metallic electrodes represents a unique testbed for our understanding of charge, spin, and heat transport at the nano-scale. Fascinating quantum phenomena such as giant magnetoresistance [1], Kondo effects [2], and quantum interference [3] have recently been observed in such systems. In addition, molecular junctions can be seen as model systems allowing for detailed studies of charge transfer and energy level alignment at metal–molecule interfaces [4] of great relevance to, e.g., organic electronic devices and dye-sensitized solar cells.

It has recently been proposed that molecular junctions could be used as basis for thermoelectric energy conversion [5,6]. As a first step towards this goal, several groups have recently reported measurements of the thermopower, S , of molecular junctions [7–14]. The thermopower enters the dimensionless thermoelectric figure of merit $ZT = GS^2T/\kappa$ characterizing the efficiency of a thermoelectric material. Here G is the electronic conductance, T is temperature, and κ is the thermal conductance with contributions from both electrons and phonons. ZT should

be large ($ZT > 1$) in order to achieve efficient energy conversion.

Thermopower measurements are also interesting as a spectroscopic tool as it provides information about the carrier type, i.e., whether the transport is dominated by the highest occupied molecular orbital (HOMO) or the lowest unoccupied molecular orbital (LUMO) [15]. Importantly, this information cannot be deduced from standard current–voltage characteristics (without a gate electrode).

Previous first-principles calculations of thermopower in molecular junctions have been based on density functional theory (DFT) within the Landauer formalism [16–18,14]. While the standard generalized gradient approximation (GGA) to the exchange–correlation functional generally overestimates both thermopower and conductance [16,18] better agreement with experimental values were reported for certain hybrid functionals with a simplified wide-band approximations. [17] By correcting for DFT-GGA self-interaction errors and image charge effects in a non-self-consistent way within the DFT + Σ approach, good agreement with experiments for both conductance and

thermopower values have recently been reported [18, 14]. Such simple correction schemes are attractive since they allow for efficient treatment of relatively large systems. However, their formal justification is limited to weakly coupled molecules. Specifically, charge-transfer screening [19], inelastic scattering [20], as well as orbital renormalization [21] are not accounted for by such methods. Moreover, their performance has not yet been benchmarked against more elaborate and fully self-consistent calculations. We mention that a large number of high-thermopower molecular devices have recently been proposed on the basis of theoretical DFT studies [22–28].

It has recently become clear that predictive and quantitatively accurate modeling of electronic energy level alignment and charge transport in metal–molecule junctions must be based on methods that go beyond the single-particle DFT description. The latter (with the standard GGA) significantly underestimates the distance from the molecular energy levels to the metal Fermi energy, in particular for the unoccupied orbitals [29], and consequently overestimates tunneling through the molecular HOMO–LUMO gap. In contrast, the GW method based on many-body perturbation theory yields excellent quasiparticle energies of both molecules [30, 31], metals [32] and semiconductors [33, 34], and drastically improves the description of the electronic structure of metal–molecule interfaces compared to DFT [29, 35]. Very recently, self-consistent GW conductance calculations for simple molecules in idealized junction geometries were shown to be in good agreement with experiments [36, 37].

In this work we report GW calculations of conductance and thermopower in molecular junctions and perform a systematic assessment of the sensitivity of these quantities on the atomic details of the electrode–molecule interface. Specifically, we consider benzenediamine (BDA) and benzenedicarbonitrile (BDCN) connected to gold electrodes. Conductance measurements for the two molecules have been reported in Refs. [38, 39], respectively, while thermopower measurements were reported in Refs. [8, 10]. We find that the GW results are in good agreement with the measured values for both molecules. While DFT-based results display large discrepancies with experiments, in particular for the BDCN junction, the energy level-corrected DFT + Σ approach yields better agreement with experiments and GW results. Having thus justified the DFT + Σ approach we use this computationally efficient method to investigate the detailed influence of junction geometries. This analysis shows that the DFT + Σ results are relatively robust against variations in the bonding geometry, and that the discrepancies between DFT-GGA and experiments cannot be explained by structural differences in the experiments and calculations.

2 Methods We consider molecules connected to a left (L) and right (R) semi-infinite gold electrode, each characterized by chemical potentials $\mu_{L,R}$ and temperature $T_{L,R}$. In the limit of small differences $V = (\mu_L - \mu_R)/e$ and $\Delta T = T_L - T_R$ the conductance and thermopower can be obtained

from the transmission function

$$\mathcal{T}(E) = \text{Tr} [G^r(E)\Gamma_L(E)G^a(E)\Gamma_R(E)], \quad (1)$$

where $G^{r(a)}(E)$ is the retarded (advanced) Green's function, and $\Gamma_{L,R}(E) = i(\Sigma_{L,R}^r(E) - \Sigma_{L,R}^a(E))$ describes the level broadening due to coupling to the left and right electrodes expressed in terms of the electrode self-energies $\Sigma_{L,R}(E)$. Defining the function $L_m(\mu)$:

$$L_m(\mu) = \frac{2}{h} \int_{-\infty}^{\infty} dE \mathcal{T}(E)(E - \mu)^m \left(-\frac{\partial f(E, \mu, T)}{\partial E} \right), \quad (2)$$

where $f(E, \mu, T)$ is the Fermi–Dirac distribution function at the (average) chemical potential μ and temperature T , the electronic conductance, G , and thermopower, S , are given by

$$G = e^2 L_0(E_F) \quad (3)$$

$$S = - \lim_{\Delta T \rightarrow 0} \frac{\Delta V}{\Delta T} \Big|_{I=0} = \frac{L_1(E_F)}{e T L_0(E_F)}. \quad (4)$$

Here we have included the definition of the thermopower, which is the proportionality constant between the temperature difference, ΔT , and the voltage bias, ΔV , needed to balance the electronic current induced by ΔT . If the transmission function is slowly varying the thermopower is approximately given by [15], $S = -\pi^2 k_B^2 T / (3e) \partial \ln(\mathcal{T}(E)) / \partial E|_{E=\mu}$, showing that a high thermopower is achieved when the slope of the transmission function is steep. Here, T is the average temperature of the left and right electrodes. We note that the thermopower in Eq. (4) is defined within linear response, and is thus applicable when $\Delta T/T$ is small. While nonlinear effects in principle could play a role we expect this to be of minor importance for the experiments we compare our calculations with, since in the experiments $T \approx 300$ K and $\Delta T < 30$ K. Moreover, the experiments directly show a linearly increasing ΔV versus ΔT indicating that the linear response formula is adequate.

2.1 DFT We use three different methods to calculate the (retarded) Green's function and electronic transmission. First, we use the standard DFT-NEGF approach, $G_{\text{DFT}}^r = ((E + i\eta) \cdot S - H_{\text{KS}} - \Sigma_L^r(E) - \Sigma_R^r(E))^{-1}$, where H_{KS} is the effective one-particle Kohn–Sham Hamiltonian expressed in a double- ζ polarized basis of localized atomic orbitals [40], S is the overlap matrix between the orbitals, and η is a positive infinitesimal. For the DFT calculations we use GPAW [41], which is an electronic structure code based on the projector-augmented wave method. The calculations are performed with a (4, 4, 1) k -point sampling and the exchange correlation potential described by the Perdew–Burke–Ernzerhof (PBE) functional [42].

2.2 GW Second, in order to describe exchange and correlation effects beyond DFT we apply the self-consistent GW

Table 1 Experimental [47] (exp.) and calculated ionization potential (IP) and electron affinity (EA) obtained from total energy calculations (ΔE) and from GW calculations. ε_H and ε_L are the Kohn–Sham HOMO and LUMO energies. The image charge energy shifts for the occupied states Δ_{occ} and for the unoccupied states, Δ_{unocc} are calculated from the HOMO and LUMO charge distributions, respectively. The two numbers correspond to the image plane placed 1 Å inside (outside) the closest Au atom. The total shift of the occupied (unoccupied) states are denoted by Σ_{occ} (Σ_{unocc}), with the two numbers corresponding to the two positions of the image plane. All energies are in units of eV.

	IP _{exp.}	EA _{exp.}	IP _{ΔE}	EA _{ΔE}	IP _{GW}	EA _{GW}	$-\varepsilon_H$	$-\varepsilon_L$	Δ_{occ}	Δ_{unocc}	Σ_{occ}	Σ_{unocc}
BDA	6.87	–	6.9	–1.0	6.2	–2.9	4.0	0.7	0.9 (1.6)	–0.8 (–1.3)	–1.9 (–1.2)	0.8 (0.4)
BDCN	10.1	1.1	9.9	1.3	9.2	–0.1	7.1	3.4	0.8 (1.3)	–0.7 (–1.2)	–2.1 (–1.6)	1.3 (0.9)

approximation, in which the retarded Green’s function of the molecule is given by

$$G_{GW}^r(E) = [(E + i\eta) \cdot S - (H_{KS} - V_{xc}) - \Sigma_{GW}^r(E) - \Sigma_L^r(E) - \Sigma_R^r(E)]^{-1}. \quad (5)$$

Here we subtract the PBE exchange–correlation potential, V_{xc} , from the DFT hamiltonian, H_{KS} , and add the GW self-energy $\Sigma_{GW}(E)$. Since the GW self-energy depends on $G^r(E)$ at all energies, Eq. (5), together with the equations for the GW self-energy, need to be solved self-consistently for all energies, which is a computationally demanding task that at present is only possible for small molecules. The details of the GW-transport method have been described previously in Refs. [36, 37, 43]. We have checked that ionization potentials of free molecules calculated with GW applying a double-zeta polarized basis set agree to within 0.3 eV with GW calculations employing much larger basis sets (up to triple-zeta with double polarization) [30].

2.3 DFT + Σ It is well known that DFT is unable to accurately describe energy gaps and level alignment of molecules at surfaces [29]. The GW approach greatly improves the description, but at the cost of being computationally very demanding. It is thus desirable of comparing the GW results to a numerically easier method, that allows for systematic studies of many junction structures and larger molecules. One such method is the non-self-consistent self-energy correction scheme (DFT + Σ) that has recently been shown to predict conductance and thermopower values in good agreement with single-molecule experiments [14, 18, 44, 45]. In this section we provide a detailed description of our implementation of the method. In the DFT + Σ approach we initially correct the gas phase HOMO and LUMO energies. This is done by calculating the ionization potential (IP) and electron affinity (EA) from total energy calculation:

$$IP = E(+e) - E(0), \quad (6)$$

$$EA = E(0) - E(-e), \quad (7)$$

where $E(0)$ is the total energy of the neutral molecule, $E(+e)$ is the energy of the molecule with one electron removed (i.e., positively charged), and $E(-e)$ is the total energy of the

molecule with one extra electron on it. For the IP and EA gas-phase calculations we use the GPAW code with a real space grid basis [41]. The calculated values are shown in Table 1. Also shown in the table are the Kohn–Sham HOMO and LUMO energies, obtained from GPAW with a double- ζ polarized basis of localized atomic orbitals [40]. While the real-space basis generally yields more accurate results, the transport calculations need the LCAO basis, and hence we calculate the Kohn–Sham energies with the LCAO basis. We note that the calculated IPs and EAs are in close agreement with experimental values. Also note that traditionally IP and EA are defined as *positive* for energies below the vacuum level, whereas HOMO and LUMO level positions are *negative*, if they are below the vacuum level.

When a molecule is brought close to a metallic surface, image charge interactions will change the energy levels resulting in a shift of the occupied levels *up* in energy and the unoccupied states *down* in energy [35]. We estimate the image charge corrections following Ref. [44]: (i) From a calculation with the molecule placed in the junction, we obtain a Hamiltonian, H , and overlap matrix, S , describing both molecular and metal atoms. From these matrices we cut out the sub-matrices H_{mol} and S_{mol} spanned only by the LCAO basis functions on the molecular atoms. The eigenenergies, ε_i and eigenvectors, $\psi^{(i)}$ for the molecule in the junction are obtained from the equation

$$H_{mol}\psi^{(i)} = \varepsilon_i S_{mol}\psi^{(i)}. \quad (8)$$

We obtain a point charge distribution for a given orbital, i , as

$$\rho_i(r) = -e \sum_v \sum_\alpha |\psi_{v,\alpha}^{(i)}|^2 \delta(r - R_v), \quad (9)$$

where $-e$ is the electron charge and $\psi_{v,\alpha}^{(i)}$ is the coefficient for orbital α at atom v with position R_v . The image charge energy for a point charge distribution placed between two image planes located at $x = 0$ and $x = L$ is

$$\Delta_i = \frac{1}{8\pi\varepsilon_0} \sum_{\alpha=1}^N \sum_{\beta=1}^N \rho_i(r_\alpha) \rho_i(r_\beta) \times \sum_{n=1}^{\infty} \left[\frac{1}{\sqrt{(x_\alpha + x_\beta - 2nL)^2 + R_{\alpha\beta}^2}} \right]$$

$$\left. \begin{aligned} & + \frac{1}{\sqrt{(x_\alpha + x_\beta + (n-1)L)^2 + R_{\alpha\beta}^2}} \\ & - \frac{1}{\sqrt{(x_\alpha - x_\beta + 2nL)^2 + R_{\alpha\beta}^2}} \\ & - \frac{1}{\sqrt{(x_\alpha - x_\beta - 2nL)^2 + R_{\alpha\beta}^2}} \end{aligned} \right\}, \quad (10)$$

where x_α is the x -coordinate of atom α and $R_{\alpha\beta} = \sqrt{(y_\alpha - y_\beta)^2 + (z_\alpha - z_\beta)^2}$.

We use the HOMO charge distributions to estimate the image charge correction, Δ_{occ} , for all the occupied states and likewise the LUMO charge distribution to obtain the correction Δ_{unocc} , for all the unoccupied states.

The image charge correction relies on the assumption that screening by the Au electrodes can be described classically as two flat conductors characterized by an image plane. The image plane position can in principle be calculated for a single flat surface using DFT [46, 14] yielding values of $\sim 1.5 \text{ \AA}$ outside the last metal layer. The situation is, however, more complicated for a tip structure, and one might expect a reduced screening with the effective image plane further away from the molecule. In order to assess the robustness of the method we consider both $z = \pm 1 \text{ \AA}$, relative to the closest Au atom.

The resulting shifts of all occupied states is then

$$\Sigma_{\text{occ}} = -IP - \varepsilon_{\text{H}} + \Delta_{\text{occ}} \quad (11)$$

and of all the unoccupied states

$$\Sigma_{\text{unocc}} = -EA - \varepsilon_{\text{L}} - \Delta_{\text{unocc}}, \quad (12)$$

where ε_{H} and ε_{L} are the Kohn–Sham HOMO and LUMO energies from a gas-phase calculation (measured relative

to the vacuum level). The calculated values are shown in Table 1.

We now obtain a corrected molecular Hamiltonian as

$$\begin{aligned} \tilde{H}_{\text{mol}} &= H_{\text{mol}} + \Sigma \\ &= \sum_{i \in \text{occ.}} (\varepsilon_i + \Sigma_{\text{occ}}) |\psi_i\rangle \langle \psi_i| \\ &\quad + \sum_{j \in \text{unocc.}} (\varepsilon_j + \Sigma_{\text{unocc}}) |\psi_j\rangle \langle \psi_j|, \end{aligned} \quad (13)$$

which replaces H_{mol} in the larger matrix H describing the whole junction. From the corrected Hamiltonian we calculate the transmission function as described above.

3 Results In all junction structures considered below the molecule (BDA or BDCN) is placed between Au(111) electrodes with either a tip, an adatom or a trimer on the surface. In all structures, the molecule and the outermost Au atoms, including the first Au layers (16 atoms) on each side, have been relaxed until the forces were below 0.05 eV \AA^{-1} . We use 8 Au layers in total and a (4, 4, 1) k-point sampling.

Figure 1 shows the calculated transmission functions for BDA (c) and BDCN (d). Here the molecules are connected to Au tips as shown in panels (a) and (b). The vertical bars at $E = E_{\text{F}}$ indicate an approximate experimental range of conductance values in units of $G_0 = 2e^2/h$. The dashed purple lines have slopes which would reproduce the experimental thermopower values. In agreement with previous studies we find that the transmission through BDA is HOMO dominated and the transmission at the Fermi level has a negative slope, and hence a positive thermopower in qualitative agreement with experiments. An exception to this is the DFT + $\Sigma(-1 \text{ \AA})$ with the image planes placed inside the Au tips, which give a slightly positive slope. We also note that both the GW and DFT + Σ results fall within the experimental range of conductances, while the DFT transmission

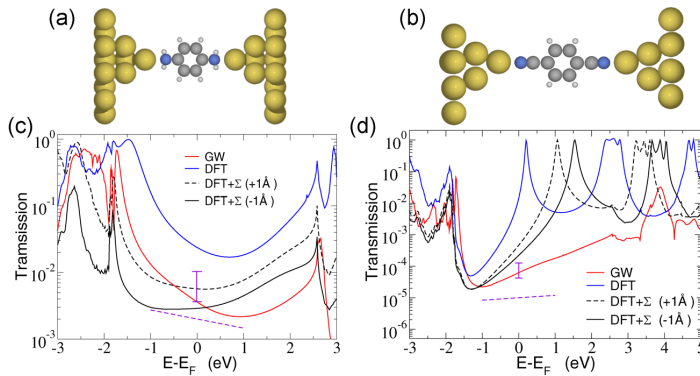


Figure 1 Junction structure for tip configurations of BDA (a) and BDCN (b). The transmission functions are shown in panels (c) and (d) calculated with GW (red), DFT (blue) and DFT + Σ (black). For DFT + Σ we show results for image plane positions $\pm 1 \text{ \AA}$ relative to the tip Au atom. The vertical bars at $E = E_{\text{F}}$ indicate the experimental conductance ranges and the dashed lines have slopes that would give the experimental thermopowers.

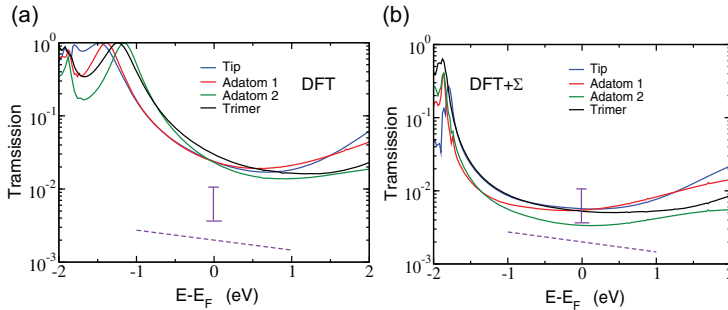


Figure 2 Transmission functions for different BDA junction structures calculated with DFT (a) and DFT + Σ (b) with the image planes at +1 Å outside the last Au atom. The junction structures are shown in Fig. 3.

at the Fermi level is a factor 2–3 too high. The DFT- and GW curves are seen to have too large slopes (in absolute values) compared with the experimental situation, whereas the DFT + Σ (+1 Å) is seen to have a slope that matches the experiments very well. The calculated conductance and thermopower values are given in Table 2.

We note that the features in the transmission function around -1.8 and 2.5 eV reflect the local density of states at the tip Au atom and are not related to the molecular levels. Since the gold atoms are always treated at DFT level in our calculations, these features appear at the same energies in the GW, DFT and DFT + Σ spectra.

Turning now to the BDCN transmissions (panel d) we observe much larger deviations between the three methods. In agreement with previous calculations [48], DFT gives a LUMO transmission peak right above the Fermi level. This leads to a conductance more than two orders of magnitude larger than the estimated experimental value [49]. On the other hand, DFT + Σ and GW shift the LUMO to higher energies and therefore yield lower conductances, with in particular the GW result close to the experiment. All three methods predict a negative thermopower (positive slope of $\mathcal{T}(E_F)$), but the magnitude is largely different, with the GW curve being closest to the experimental slope – see also

Table 2 Experimental and calculated conductance and thermopower values for BDA and BDCN in tip configurations. The corresponding transmission functions are shown in Fig. 1. For DFT + Σ we show the results for two different positions of the image plane: ± 1 Å correspond to 1 Å outside (inside) the last Au atom. The conductances are given in units of $G_0 = 2e^2/h$ and the thermopowers are in units of μVK^{-1} .

	BDA		BDCN	
	G	S	G	S
exp.	6.4×10^{-3}	2.3	8.4×10^{-5}	-1.3
GW	3.6×10^{-3}	7.8	6.3×10^{-5}	-9.2
DFT	24×10^{-3}	6.7	1.9×10^{-2}	-129
DFT + Σ (+1)	5.7×10^{-3}	0.8	4.7×10^{-4}	-24
DFT + Σ (-1)	2.9×10^{-3}	-0.9	2.2×10^{-4}	-19

Table 2. We note that the GW LUMO transmission peak around $E - E_F = 4.0$ eV has a significantly lower peak value (~ 0.05) than the DFT and DFT + Σ peak values of 1. This is due to quasiparticle scattering by electron-electron interaction which reduces the quasiparticle lifetimes at energies $E \neq E_F$. Mathematically this shows as a finite imaginary part of the GW self-energy which broadens the resonance and lowers the peak height [20]. We also note that GW predicts the LUMO energy to be significantly higher than the DFT + Σ results. The GW LUMO position might be too high in energy due to the finite basis set used in the calculations. However, we have checked that the GW conductance and thermopower are relatively robust against a manual downshift of the LUMO position. A down shift of the LUMO position by 2 eV leads to a conductance increase by a factor of 4 while the thermopower increases by a factor of 2, and thus remain close to the experimental values.

3.1 Structure dependence: BDA While the transmission functions in Fig. 1 and data in Table 2 indicate that both DFT + Σ and GW significantly improve the description of the electronic structure compared with ordinary DFT, it cannot at this point be ruled out that the better agreement with experiments is a result of a particular, and maybe incorrect atomic structure. To address this question we have calculated the transmission function at the DFT and DFT + Σ level for four different junction geometries. Since the GW calculations are computationally very demanding we restrict this part of the analysis to the computationally easier DFT and DFT + Σ methods. The transmission functions are shown in Fig. 2. It is seen that the conductance values, i.e., $\mathcal{T}(E_F)$, within each method are largely insensitive to the specific junction geometry, the slope of the transmission functions show a larger variation, which is reflected in the thermopower values.

Figure 3 shows a scatter plot of conductance versus thermopower values for BDA calculated with the three different methods and with the experimental values indicated with the filled pentagon. For DFT + Σ , the open (closed) symbols indicate image planes 1 Å outside (inside) the last Au atom. For all four structures the DFT + Σ (+1 Å) results (open black symbols) are very close to the experiments for both the

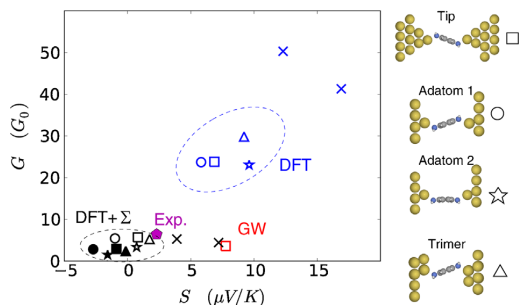


Figure 3 Scatter plot of conductance versus thermopower for BDA. Different open symbols correspond to the four different geometries shown to the right. DFT, GW, and DFT + Σ data are colored blue, red, and black respectively. For DFT + Σ we show results for image planes at 1 Å outside (inside) the closest Au atom corresponding to open (filled) symbols. In addition, we include data points from Ref. [18] (crosses) calculated for an adatom and a trimer geometry.

thermopower and the conductance, while the calculations with image planes placed 1 Å inside the Au (filled black symbols) lead to negative thermopower values. GW (red) gives a conductance close to experiments, but the thermopower is larger by a factor of three. The DFT calculations (blue) give both conductance and thermopower values larger than experiments. For comparison, we have also plotted data from Ref. [18] (crosses) for two different geometries calculated with DFT (blue) and DFT + Σ (black). In spite of the (presumably) different geometries and the different DFT codes, the agreement between our data and the data from Ref. [18] is very close. The relatively small variations observed in both conductance and thermopower of BDA for different junction structures is in agreement with previous studies [18].

3.2 Structure dependence: BDCN While the agreement between DFT + Σ (1 Å) and experiments for BDA is striking, the discrepancies are larger for the BDCN junctions. Again, we consider four different junction structures with DFT and DFT + Σ and plot the conductance and thermopower values in Fig. 4. The transmission functions calculated with DFT and DFT + Σ are shown in Fig. 5. The DFT calculations give conductance which are 2–3 orders of magnitudes too high, and thermopowers between 30 and 100 times too high compared with experiments. The DFT + Σ calculations yield conductances, which are larger than experiments by factors 3–200. The largest discrepancy is found for the tilted tip configurations. The high conductance found for this configuration is caused by a much stronger coupling of the LUMO orbital to the Au resulting in a significant broadening of the LUMO transmission peak as seen in Fig. 5. The stronger coupling of the LUMO with the Au can be understood from the symmetries of the LUMO and the gold s -states. In the linear tip configuration, the LUMO, which has π -character, couples very weakly to the Au s -orbitals due to different symmetries. In the tilted tip configuration there

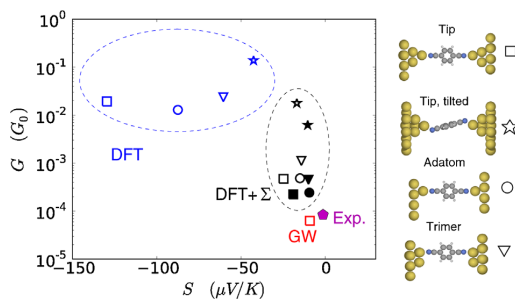


Figure 4 Scatter plot of conductance versus thermopower for BDCN. The different open symbols correspond to the four different geometries shown to the right. DFT, GW, and DFT + Σ data are colored blue, red, and black, respectively. For DFT + Σ we show results for image planes at 1 Å outside (inside) the closest Au atom corresponding to open (filled) symbols.

is no such symmetry mismatch and the LUMO hybridizes much stronger with the Au. However, the tilted tip configuration is also energetically much less favorable than the linear tip configuration. Excluding this geometry, the DFT + Σ conductances are within an order of magnitude from the experimental value. The thermopower from DFT + Σ are (numerically) an order of magnitude larger than the experimental value.

For the BDCN tip geometry, the GW calculations are in very good agreement with the experiments: The conductance is only 25% lower than the experimental value and the thermopower is larger by a factor of 7. While the very close agreement between GW and experimental conductances might be coincidental for the specific geometry, there is no doubt that a description of exchange and correlation effect beyond semi-local DFT is crucial for the BDCN junction.

3.3 Stretching simulation of BDA junction As an additional investigation of the influence of contact geometry we have simulated a stretching experiments for BDA between two Au tips. Initially, the tips are close together with the molecule in a relaxed configuration in between them as shown in Fig. 6 (top left). We have subsequently opened the junction in steps of 0.25 Å. In each step we relax the atomic coordinates for the molecule and Au tip atoms including the first Au layer in the electrodes. When the forces are below 0.05 eV Å⁻¹ the right electrode is again shifted by 0.25 Å and a new relaxation is performed. For each of the relaxed geometries we subsequently calculate the conductance and thermopower with DFT and DFT + Σ .

Figure 6 shows the conductance, thermopower, and change in total energy versus electrode separation. In the top we include snap shot images of the structure at $z = 0, 1, 2, 3, 4$ Å. Starting from a configuration, where the molecule is tilted at an angle $\sim 45^\circ$, the molecule is turning to a more linear configuration, when the junction is stretched. The most stable configuration is found at $z = 2.0$ Å. The bond between the molecule and right Au tip starts to break

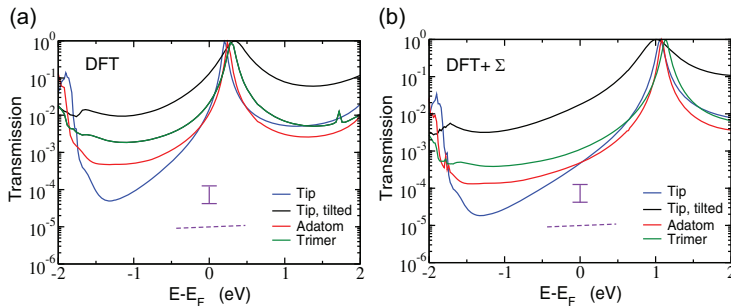


Figure 5 Transmission functions for different BDCN junction structures calculated with DFT (a) and DFT + Σ (b) with the image planes at +1 Å outside the last Au atom. The junction structures are shown in Fig. 4.

around $z \approx 3 \text{ \AA}$ where the Au–N distance at the right contact starts to increase whereas the left Au–N distance does not. The bond breaking is also seen in the conductance values which start to decrease exponentially around $z \approx 3 \text{ \AA}$. Both the DFT and DFT+ Σ conductances are remarkably stable in the first half of the stretching simulation. Except for $z =$

0.0 Å the conductances are constant up to $z = 2.0 \text{ \AA}$ while the thermopower show only a slight decrease.

The stretching simulation indicate that the conductance and thermopower are rather insensitive to the exact electrode–electrode separation. Together with the results in Figs. 3 and 2 we therefore conclude that the DFT + Σ results for the conductance and thermopower are reliable, and the close agreement with experiments is not a result of a particular atomic geometry. The close agreement with GW calculations further support DFT + Σ as a viable method for predicting the conductance and thermopower of molecular junctions, at least within an order of magnitude.

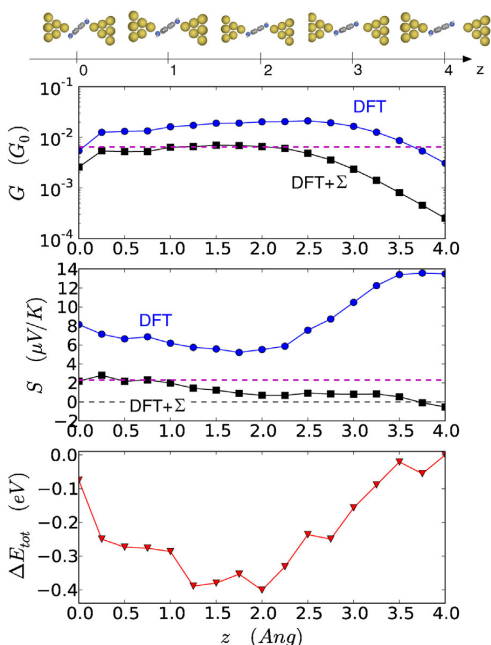


Figure 6 Stretching simulation. Conductance G and thermopower S , calculated with DFT (blue dots) and DFT + Σ (black squares) as function of electrode–electrode separation, z . The bottom panel shows the change in total energy ΔE_{tot} , relative to the final configuration. The zero-point of z is arbitrarily set at the initial configuration. On the top, we show snap shot images of the geometries at $z = 0, 1, \dots, 4 \text{ \AA}$. The dashed purple lines indicate the experimental conductance and thermopower values.

4 Discussion and conclusions

Concerning the image plane position in the DFT + Σ approach, we note that the +1 Å position gives the best agreement with experiments for BDA, but the opposite is true for BDCN where the –1 Å position gives results closer to experimental values. Although the variations with respect to image plane position are rather small, the deviating results may indicate limitations in the DFT + Σ approach due to the classical description of the image charge energy.

In our calculations we have neglected the effect of electron–phonon (el–ph) interactions. For non-resonant transport, as in our case, el–ph interactions only affect the electronic current by few percents in atomic junctions [50], although exceptions may occur when levels are quasi degenerate [51] or in molecules with large torsion angles between separate π -systems [27]. These exceptions are not relevant for the considered BDA or BDCN junctions. Even though the conductance is only weakly affected by el–ph interactions, the effect on the thermopower might be larger but still expectedly within 10–20% [27]. We expect that el–ph interactions will only lead to small quantitative changes of the calculated thermopower values and we expect all our conclusions to still be valid.

In conclusion, we have calculated the electronic conductance and thermopower for BDA and BDCN single-molecule junctions. With the electronic exchange and correlation effects described by the self-consistent GW approximation we find good agreement with experimental results for both

molecules. While DFT (GGA) calculated conductances and thermopowers for different BDA junctions agree with experimental results within a factor of 5, there are much larger discrepancies for the BDCN junction where the DFT results differ from the experiments by two orders of magnitude. A simple correction to the DFT Hamiltonian (DFT + Σ) improves the results for both BDA and BDCN. By considering various junction geometries we find that our results are robust against small structural changes. Our results demonstrate that a proper treatment of exchange–correlation effects is important when modeling electronic and thermoelectric properties of molecular junctions.

Acknowledgements The authors acknowledge support from the Danish Council for Independent Research's Sapere Aude Program through Grants No. 11-104592, No. 11-120938, and No. 11-1051390.

References

- [1] S. Schmaus, A. Bagrets, Y. Nahas, T. K. Yamada, A. Bork, M. Bowen, E. Beaupaire, F. Evers, and W. Wulfhekel, *Nature Nanotechnol.* **6**(3), 185–189 (2011).
- [2] J. Park, A. N. Pasupathy, J. I. Goldsmith, C. Chang, Y. Yaish, J. R. Petta, M. Rinkoski, J. P. Sethna, H. D. Abruna, P. L. McEuen, and D. C. Ralph, *Nature* **417**(6890), 722–725 (2002).
- [3] C. M. Guedon, H. Valkenier, T. Markussen, K. S. Thygesen, J. C. Hummelen, and S. J. van der Molen, *Nature Nanotechnol.* **7**(5), 304–308 (2012).
- [4] J. M. Beebe, B. Kim, J. W. Gadzuk, C. Daniel Frisbie, and J. G. Kushmerick, *Phys. Rev. Lett.* **97**(2), 026801 (2006).
- [5] P. Murphy, S. Mukerjee, and J. Moore, *Phys. Rev. B* **78**(16), 161406 (2008).
- [6] Y. Dubi and M. Di Ventra, *Rev. Mod. Phys.* **83**(1), 131–155 (2011).
- [7] P. Reddy, S. Y. Jang, R. A. Segalman, and A. Majumdar, *Science* **315**(5818), 1568–1571 (2007).
- [8] K. Baheti, J. A. Malen, P. Doak, P. Reddy, S. Y. Jang, T. D. Tilley, A. Majumdar, and R. A. Segalman, *Nano Lett.* **8**(2), 715–719 (2008).
- [9] J. A. Malen, P. Doak, K. Baheti, T. D. Tilley, A. Majumdar, and R. A. Segalman, *Nano Lett.* **9**(10), 3406–3412 (2009).
- [10] J. A. Malen, P. Doak, K. Baheti, T. D. Tilley, R. A. Segalman, and A. Majumdar, *Nano Lett.* **9**(3), 1164–1169 (2009).
- [11] A. Tan, S. Sadat, and P. Reddy, *Appl. Phys. Lett.* **96**(1), 013110 (2010).
- [12] S. K. Yee, J. A. Malen, A. Majumdar, and R. A. Segalman, *Nano Lett.* **11**(10), 4089–4094 (2011).
- [13] A. Tan, J. Balachandran, S. Sadat, V. Gavini, B. D. Dunietz, S. Y. Jang, and P. Reddy, *J. Am. Chem. Soc.* **133**(23), 8838–8841 (2011).
- [14] J. R. Widawsky, P. Darancet, J. B. Neaton, and L. Venkataraman, *Nano Lett.* **12**(1), 354–358 (2011).
- [15] M. Paulsson and S. Datta, *Phys. Rev. B* **67**(24), 241403 (2003).
- [16] F. Pauly, J. K. Viljas, and J. C. Cuevas, *Phys. Rev. B* **78**(3), 035315 (2008).
- [17] S. H. Ke, W. Yang, S. Curtarolo, and H. U. Baranger, *Nano Lett.* **9**(3), 1011–1014 (2009).
- [18] S. Y. Quek, H. J. Choi, S. G. Louie, and J. B. Neaton, *ACS Nano* **5**(1), 551–557 (2011).
- [19] J. D. Sau, J. B. Neaton, H. J. Choi, S. G. Louie, and M. L. Cohen, *Phys. Rev. Lett.* **101**(2), 026804 (2008).
- [20] K. S. Thygesen, *Phys. Rev. Lett.* **100**(16), 166804 (2008).
- [21] M. Strange and K. S. Thygesen, *Phys. Rev. B* **86**(19), 195121 (2012).
- [22] C. M. Finch, V. M. Garcia-Suarez, and C. J. Lambert, *Phys. Rev. B* **79**(3), 033405 (2009).
- [23] Y. S. Liu and Y. C. Chen, *Phys. Rev. B* **79**(19), 193101 (2009).
- [24] J. P. Bergfield and C. A. Stafford, *Nano Lett.* **9**(8), 3072–3076 (2009).
- [25] J. P. Bergfield, M. A. Solis, and C. A. Stafford, *ACS Nano* **4**(9), 5314–5320 (2010).
- [26] D. Nozaki, H. Sevinclik, W. Li, R. Gutierrez, and G. Cuniberti, *Phys. Rev. B* **81**(23), 235406 (2010).
- [27] N. Sergueev, S. Shin, M. Kaviani, and B. Dunietz, *Phys. Rev. B* **83**(19), 195415 (2011).
- [28] R. Stadler and T. Markussen, *J. Chem. Phys.* **135**(15), 154109 (2011).
- [29] J. M. Garcia-Lastra, C. Rostgaard, A. Rubio, and K. S. Thygesen, *Phys. Rev. B* **80**, 245427 (2009).
- [30] C. Rostgaard, K. W. Jacobsen, and K. S. Thygesen, *Phys. Rev. B* **81**(8), 085103 (2010).
- [31] X. Blase, C. Attaccalite, and V. Olevano, *Phys. Rev. B* **83**(11), 115103 (2011).
- [32] B. Holm and U. von Barth, *Phys. Rev. B* **57**(4), 2108–2117 (1998).
- [33] M. Shishkin, M. Marsman, and G. Kresse, *Phys. Rev. Lett.* **99**(24), 246403 (2007).
- [34] M. van Schilfgarde, T. Kotani, and S. Faleev, *Phys. Rev. Lett.* **96**(22), 226402 (2006).
- [35] J. B. Neaton, M. S. Hybertsen, and S. G. Louie, *Phys. Rev. Lett.* **97**(21), 216405 (2006).
- [36] M. Strange, C. Rostgaard, H. Hakkinen, and K. S. Thygesen, *Phys. Rev. B* **83**(11), 115108 (2011).
- [37] M. Strange and K. S. Thygesen, *Beilstein J. Nanotechnol.* **2**, 746–754 (2011).
- [38] L. Venkataraman, J. E. Klare, I. W. Tam, C. Nuckolls, M. S. Hybertsen, and M. L. Steigerwald, *Nano Lett.* **6**(3), 458–462 (2006).
- [39] H. Song, Y. Kim, Y. H. Jang, H. Jeong, M. A. Reed, and T. Lee, *Nature* **462**(7276), 1039–1043 (2009).
- [40] A. H. Larsen, M. Vanin, J. J. Mortensen, K. S. Thygesen, and K. W. Jacobsen, *Phys. Rev. B* **80**, 195112 (2009).
- [41] J. Enkovaara, C. Rostgaard, J. J. Mortensen, J. Chen, M. Dulak, L. Ferrighi, J. Gavnholt, C. Glinsvad, V. Haikola, H. A. Hansen, H. H. Kristoffersen, M. Kuisma, A. H. Larsen, L. Lehtovaara, M. Ljungberg, O. Lopez-Acevedo, P. G. Moses, J. Ojanen, T. Olsen, V. Petzold, N. A. Romero, J. Stausholm-Moller, M. Strange, G. A. Tritsarlis, M. Vanin, M. Walter, B. Hammer, H. Hakkinen, G. K. H. Madsen, R. M. Nieminen, J. K. Norkov, M. Puska, T. T. Rantala, J. Schiøtz, K. S. Thygesen, and K. W. Jacobsen, *J. Phys.: Condens. Matter* **22**(25), 253202 (2010).
- [42] J. P. Perdew, K. Burke, and M. Ernzerhof, *Phys. Rev. Lett.* **77**, 3865 (1996).
- [43] K. S. Thygesen and A. Rubio, *Phys. Rev. B* **77**(11), 115333 (2008).
- [44] D. J. Mowbray, G. Jones, and K. S. Thygesen, *J. Chem. Phys.* **128**(11), 111103 (2008).
- [45] S. Y. Quek, H. J. Choi, S. G. Louie, and J. B. Neaton, *Nano Lett.* **9**, 3949 (2009).

- [46] S. C. Lam and R. J. Needs, *J. Phys.: Condens. Matter* **5**, 2101–2108 (1993).
- [47] <http://webbook.nist.gov/chemistry/>.
- [48] Y. Xue and M. A. Ratner, *Phys. Rev. B* **69**(8), 085403 (2004).
- [49] We obtain an estimate of the BDCN conductance from Ref. [39], Supplementary Information, Fig. S8. In the Fowler–Nordheim plot we read off $\ln(I/V^2) = -16.36$ at $V = 0.1$ V giving a conductance $G = I/V = 1.0 \times 10^{-4} G_0$. At $V = 0.2$ V we read off $\ln I/V^2 = -17.45$ giving $G = I/V = 6.8 \times 10^{-5} G_0$. We take the average $G = 8.4 \times 10^{-5} G_0$ as an estimate of the experimental conductance.
- [50] M. Galperin, M. A. Ratner, and A. Nitzan, *J. Phys.: Condens. Matter* **19**(10), 103201 (2007).
- [51] R. Härtle, M. Butzin, O. Rubio-Pons, and M. Thoss, *Phys. Rev. Lett.* **107**(4), 046802 (2011).

Paper III**Single-molecule electrochemical transistor utilizing a nickel-pyridyl spinterface**

R. J. Brooke, C. Jin, D. Szumski, R. J. Nichols, B. Mao, K. S. Thygesen, W. Schwarzacher

Nano Letters **15**, 275 (2015)

Single-Molecule Electrochemical Transistor Utilizing a Nickel-Pyridyl Spinterface

Richard J. Brooke,[†] Chengjun Jin,[‡] Doug S. Szumski,[†] Richard J. Nichols,[§] Bing-Wei Mao,[⊥] Kristian S. Thygesen,^{*,‡} and Walther Schwarzacher^{*,†}

[†]H. H. Wills Physics Laboratory, University of Bristol, Tyndall Avenue, Bristol BS8 1TL, United Kingdom

[‡]Center for Atomic-Scale Materials Design (CAMD) and Center for Nanostructured Graphene (CNG), Department of Physics, Technical University of Denmark, DK2800 Kongens Lyngby, Denmark

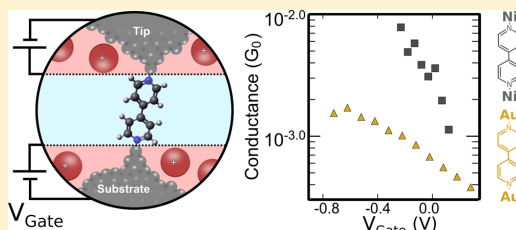
[§]Department of Chemistry, University of Liverpool, Liverpool L69 7ZD, United Kingdom

[⊥]State Key Laboratory of Physical Chemistry of Solid Surfaces, Chemistry Department, College of Chemistry and Chemical Engineering, Xiamen University, Xiamen 361005, China

Supporting Information

ABSTRACT: Using a scanning tunnelling microscope break-junction technique, we produce 4,4'-bipyridine (44BP) single-molecule junctions with Ni and Au contacts. Electrochemical control is used to prevent Ni oxidation and to modulate the conductance of the devices via nonredox gating—the first time this has been shown using non-Au contacts. Remarkably the conductance and gain of the resulting Ni-44BP-Ni electrochemical transistors is significantly higher than analogous Au-based devices. Ab-initio calculations reveal that this behavior arises because charge transport is mediated by spin-polarized Ni *d*-electrons, which hybridize strongly with molecular orbitals to form a “spinterface”. Our results highlight the important role of the contact material for single-molecule devices and show that it can be varied to provide control of charge and spin transport.

KEYWORDS: Single-molecule, break-junction, electrochemical gating, spintronics, density functional theory, metal–molecule interface



Single-molecule transistor behavior can be achieved using a gate electrode to control the energy levels of a molecule bridging two metallic electrodes.¹ This gate can be provided electrochemically using the double layer potential existing at the metal–electrolyte interface (Figure 1a). An electrochemical gate avoids the complex fabrication of solid-state three-terminal molecular devices, can operate in room temperature liquid environments, and can produce high gate efficiencies thanks to the large electric fields which are achievable. There has been significant interest in redox active molecules such as viologens as candidates for electrochemical transistors;^{2–4} however, the gating of nonredox molecules has only recently been demonstrated using Au electrodes by Li et al.⁵ with 4,4'-bipyridine (44BP) molecules and subsequently by Capozzi et al.⁶ Nonredox gating relies directly on the modulation of the electronic energy levels of the molecule and the contacts and closely resembles the operation of the traditional field-effect transistor.

The metal–molecule contact plays a critical role in molecular electronics.⁷ Au-pyridyl contacts, such as the Au-44BP bond, have been shown to provide reproducible junctions, for which two conductance values can be distinguished due to different binding geometries.^{8–10} However, despite significant progress investigating different chemical linker groups,^{8,11–18} there have

been few previous attempts to broaden the range of metal electrodes studied. The use of other metals promises a better understanding of the metal–molecule interface and new effects for molecular devices. For example, ferromagnetic contacts such as Ni are anticipated to deliver single-molecule spintronic effects.^{19,20} Spin-dependent orbital hybridization at the metal–molecule interface was previously demonstrated at low temperature²¹ and more recently at room temperature by Lee et al.,²² who showed that it strongly affects thermopower of Ni–benzenedithiol–Ni single-molecule junctions.

Using a scanning tunnelling microscope (STM) break junction technique,²³ we fabricate 44BP single-molecule electrochemical transistors with Ni and Au contacts, utilizing electrochemical control to prevent oxidation of the Ni contacts and to provide nonredox electrochemical gating of the devices. The Ni devices exhibit significant advantages compared to Au-based ones, including larger conductance and more stable chemical binding due to the influence of the Ni *d*-electrons. They also exhibit stronger electrochemical transistor behavior. Calculations based on density functional theory (DFT) show

Received: September 12, 2014

Revised: November 19, 2014

Published: December 2, 2014

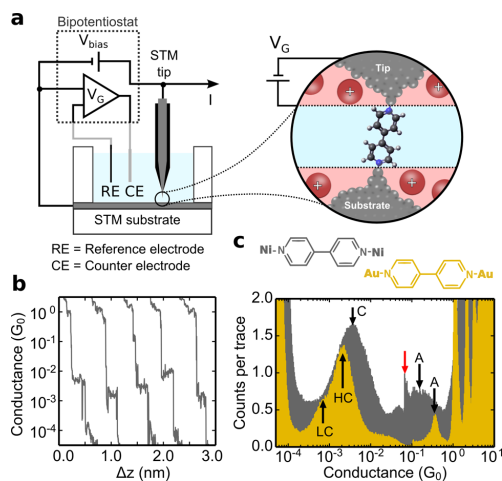


Figure 1. (a) Schematic diagram of the four-electrode cell and cartoon of the electrochemical double layer over which the gate voltage (V_G) is applied. (b) Example conductance–distance traces obtained for Ni-44BP-Ni single-molecule junctions with a substrate potential of -0.9 V. Δz is the relative displacement of the tip which is offset laterally in each scan for clarity. (c) Logarithmically binned conductance histograms for Ni (gray) and Au (yellow) junctions generated from 1441 and 2200 scans, respectively, obtained at -0.9 V without data selection. The spike-like feature (labeled with a red arrow) is an artifact of the dual-channel preamplifier used for the measurements (see Supporting Information).

that the microscopic origin of the gating is fundamentally different for Ni- and Au-based junctions due to the strong hybridization of the Ni d -electrons with the frontier molecular orbitals and the ferromagnetic nature of the Ni contacts, which is consistent with the findings of Lee et al.²²

Electrochemical control was provided by a four-electrode electrochemical cell, which is shown schematically in Figure 1a. The potentials of the STM tip and substrate were controlled relative to that of the electrolyte, which consisted of a pH 3, 0.05 M Na_2SO_4 aqueous solution. A Pt wire was used as a counter electrode, and a polypyrrole quasireference electrode (PPy) was used.²⁴ This was found to have an open circuit potential of $+0.31$ V with respect to a saturated calomel reference electrode. Au substrates were obtained commercially and were prepared by cleaning in piranha solution, a 3:1 mixture of H_2SO_4 and H_2O_2 (WARNING: piranha solution is dangerous and should be prepared and used with caution). Ni substrates were prepared by the electrodeposition of a ~ 100 nm Ni coating onto clean Au substrates. Ni and Au STM tips were produced by electrochemical etching^{25,26} and were coated with wax to minimize unwanted electrochemical currents. Ni oxide was removed by in situ electrochemical reduction.²⁷ To ensure the magnetic configuration of the Ni electrodes remained constant during the conductance measurements, a custom built electromagnet was used to provide a 2 kOe magnetic field parallel to the substrate surface.

Conductance–distance traces were obtained by measuring current through the STM tip while repeatedly withdrawing it from contact with the substrate surface. During each conductance–distance measurement the tip was first brought to a set-point current of $400 \mu\text{A}$ before the feedback was

disabled and the tip retracted by 6 nm at a rate of 20 nm s^{-1} . Figure 1b shows selected traces obtained using Ni electrodes under electrochemical control in a solution containing 44BP molecules. Plateaus observed in these traces which have $G \geq G_0$ (where G_0 is the conductance quantum $2e^2/h$) are attributed to spontaneous atomic restructuring of the metal contacts as they are stretched. Before the metal contact is broken, traces generally exhibit a plateau close to G_0 indicating the formation of single-atom contacts. After the initial separation of the newly formed contacts, a single-molecule can bridge them. In this case, a plateau is observed in the conductance–distance trace; otherwise, we observe an exponential decay of the tunnelling current (see Supporting Information). In each experiment, conductance histograms were generated from several thousand conductance traces. To avoid possible bias, no selection or filtering was applied to the data. A constant tip–substrate voltage of 0.1 V was maintained throughout the experiments, whereas the potential of the substrate with respect to the surrounding electrolyte was varied between measurements in order to modulate the gate voltage.

Figure 1c compares typical logarithmically binned conductance histograms obtained for Ni and Au junctions in the presence of 44BP under electrochemical control. Plateaus in the conductance traces give rise to clear features in the histograms. Pronounced peaks are observed in the Au histograms for $G \geq G_0$ due to the existence of preferred atomic configurations for the contacts. Even though Ni conductance traces exhibit clear plateaus for $G \geq G_0$ variation between individual traces leads to only a single broad peak in the histogram similar to previous reports of Ni atomic contacts²⁸ (see Supporting Information). Additional peaks (labeled A) observed between $0.1 G_0$ and $1 G_0$ are attributed to the effects of hydrogen adsorption on the atomic contacts^{5,29} (see Supporting Information). Molecular features appear in the histograms with $G \ll G_0$ only when 44BP molecules are present. High conductance and low conductance features (labeled HC and LC), which are typical of the Au-pyridyl contact^{8–10} are observed for Au, whereas only a single broad peak (labeled C) that has larger conductance than the Au features is observed for Ni contacts. Compared with Au, Ni junctions show considerable trace-to-trace conductance variation, leading to a broader peak in the histogram, which is similar to recently reported Ag molecular junctions.³⁰

The differences between Ni and Au junctions are also reflected in 2-dimensional (2d) histograms. In agreement with previous results,⁸ the Au histogram (see Supporting Information) exhibits two clearly distinguishable areas with a high number of counts due to the separate HC and LC configurations, whereas in Figure 2a only a single feature is seen for Ni junctions. In the initial stage of the junction evolution, the molecule is most likely tilted with respect to the junction axis because 44BP molecules are larger than the average initial electrode separation of 2.5 or 4.0 Å for Ni or Au contacts, respectively (see Supporting Information), so that the molecules are swept through a range of contact angles as the tip is retracted. In the case of Au-44BP-Au junctions, our DFT-based calculations (see later) predict a higher conductance when the molecule is tilted compared to when it is linear (see Figure 2b) with binding energies for the two configurations of 1.71 and 1.91 eV, respectively, in good agreement with previous results.⁸ Our calculations for Ni junctions show that 44BP binds more strongly to Ni than to Au by almost 1 eV, yielding binding energies for the tilted and linear configurations of 2.64 and 2.54 eV, respectively. According to the DFT-based

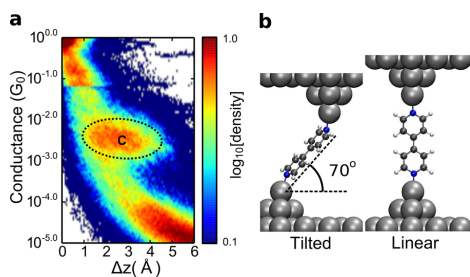


Figure 2. (a) 2d conductance histogram obtained for electrochemically controlled Ni-44BP-Ni molecular junctions with a substrate potential of -0.9 V (with respect to the PPy electrode). The individual conductance traces were offset laterally to synchronize the start of each scan with the end of the final atomic metal plateau in the range 0.8 – 2 G_0 . As such some data selection was carried out because only scans with a plateau in this range were included. This selection was done using an automated algorithm. The histogram contains 1817 out of 2520 scans. (b) The 44BP molecule in the tilted junction geometry and linear geometry.

transport calculations, the tilted and linear configurations are also found to have similar conductance (see Supporting Information), in contrast to the case of Au electrodes. This suggests that both configurations are probed in the Ni break junction experiments, but are indistinguishable from each other because the conductance is insensitive to the contact angle, which is consistent with the single feature in the histograms.

Figure 3a and b show that the conductance of Ni-44BP-Ni and Au-44BP-Au junctions vary as a function of the gate voltage applied to the substrate. The molecular peaks are clearly shifted to higher conductance values as the potential is made more negative. At potentials more positive than -0.7 V, no molecular junctions were observed for Ni contacts, which is likely due to the onset of Ni oxidation. The mean conductance was extracted from each histogram by fitting a log-normal distribution to the molecular conductance peak. These values are plotted in Figure 3c. For both Au and Ni contacts the conductance increases exponentially as the potential is made more negative. The conductance of Ni junctions is larger and the gate voltage

dependence is stronger. In the case of Au, the conductance reaches a plateau at negative potentials, which was not observed in previous studies covering a less extensive potential range.^{5,6} The gating effect can be explained by a change in the Fermi level of the electrodes (ϵ_F) relative to that of the molecule due to the potential applied between the electrodes and the solution in which the molecule is situated. As the potential is made more negative, ϵ_F is raised and the energy barrier for electron tunnelling between ϵ_F and the lowest unoccupied molecular orbital (LUMO) decreases.⁵ The conductances of Au-44BP-Au junctions measured in nonpolar 1,3,5-trimethylbenzene solvent (where no electrochemical gating is possible) are also plotted in Figure 3c at the potential of zero charge of Au electrodes in nonspecifically adsorbing HClO_4 electrolyte (PZC), where no gating effect is expected⁵ and where there is good agreement with the measurements performed in the electrochemical environment. Measurements were also performed using 1,2-bis(4-pyridyl)ethylene, which exhibits similar trends to 44BP based molecular junctions (see Supporting Information).

Our results are corroborated by DFT-based calculations of the conductance that were performed using the nonequilibrium Green's function method in the GPAW code.³² The DFT energies were corrected to account for self-interaction errors and missing image charge screening.¹⁶ The linear conductance was calculated from the Landauer formula,³³ and the effect of the electrochemical gate was simulated in a non-self-consistent way by shifting the energy levels of the molecular orbitals by a constant V_G . We also performed extensive many-body GW calculations³⁴ for the nongated linear and tilted Au junctions. The GW calculations are in good agreement with the DFT-based results, which further validates the use of the DFT-based transport scheme (see Supporting Information). Further details of the theoretical methods are described in the Supporting Information. Figure 4 shows the relevant electron transmission curves calculated using DFT-based methods for Au-44BP-Au and Ni-44BP-Ni junctions at various different values of gate voltage. These transmission curves show how the probability of an electron to be transmitted through the junction varies as a function of electron energy. Conductances calculated from such transmission curves are compared to the measured values in Figure 5. The potential difference between the Ni or Au

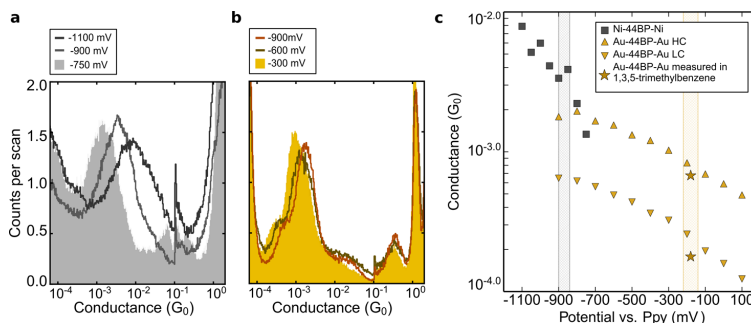


Figure 3. Conductance histograms obtained for Ni-44BP-Ni (a) and Au-44BP-Au (b) single-molecule junctions under various different potentials applied to the substrate. (c) Mean conductance values measured for Ni-44BP-Ni and Au-44BP-Au junctions under electrochemical control are plotted as a function of substrate potential. The conductance values measured for Au-44BP-Au junctions in 1,3,5-trimethylbenzene solvent are plotted at the potential of zero charge (PZC) of Au electrodes in a nonspecifically adsorbing HClO_4 electrolyte, which is -0.18 V vs the PPy scale.³¹ The PZCs for Ni (-0.87 V vs PPy³¹) and Au electrodes in HClO_4 are indicated by the gray and gold shaded regions, respectively. (PPy = $+0.31$ V vs SCE).

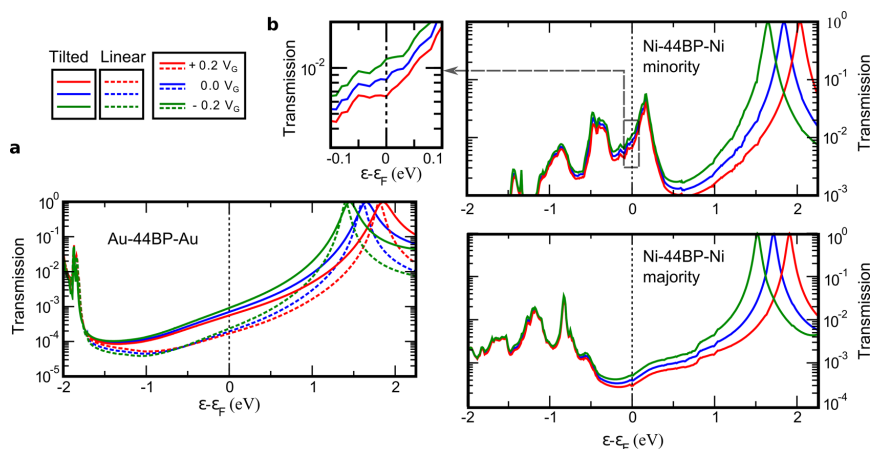


Figure 4. Transmission functions calculated at different gate voltages for (a) Au-44BP-Au junctions in the tilted configuration (solid lines), the linear configuration (dashed lines), and (b) spin-polarized Ni-44BP-Ni junctions in the tilted configuration. The upper panel shows the Ni minority spin channel, and the lower panel shows the majority channel. The inset shows a zoomed-in area of the transmission curves around the Fermi energy for the tilted configuration (see Supporting Information).

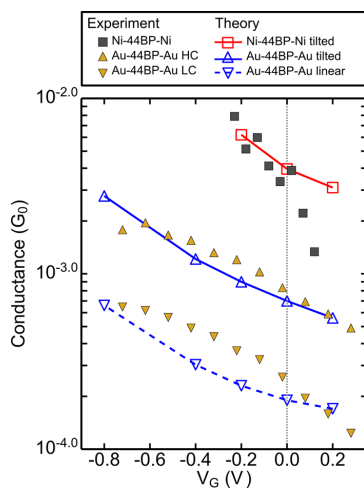


Figure 5. Comparison of the conductance calculated for Au-44BP-Au junctions and spin-polarized Ni-44BP-Ni junctions in the tilted configuration with experimentally measured values. The experimental data has been plotted so that measurements at the PZC of Ni (-0.87 V vs PPy³¹) and Au (-0.18 V vs PPy³¹) electrodes are located at $V_G = 0$.

electrodes and the reference electrode is equal to V_G plus an offset that depends on the choice of reference electrode. We assume that $V_G = 0$ corresponds to the PZC of each electrode (see previous text and Supporting Information). Using this assumption in Figure 5 provides good agreement between the calculations and the measurements performed in the electrochemical environment.

For the Au-44BP-Au transmission curves (Figure 4a), the tail of the LUMO resonance dominates the transmission at ϵ_F . In agreement with previous work, the stronger electronic coupling

of the tilted configuration broadens the LUMO resonance, leading to higher transmission compared with the linear configuration at the same gate voltage.¹⁰ As V_G is increased, ϵ_F is shifted closer to the LUMO resonance, and the transmission increases. In Figure 5, the DFT calculations predict that the conductance of Au-44BP-Au junctions continues to rise at negative potentials, whereas experimentally the conductance reaches a plateau at around $V_G = -0.6$ V. A possible explanation is that the LUMO becomes pinned to ϵ_F at negative potentials due to charge transfer to the molecule from the electrodes leading to increased Coulomb repulsion. This pinning may prevent further gating of the Au devices and limit their potential as single-molecule transistors. The effect of this pinning is not captured in our DFT-based calculations because the gating effect is simulated by shifting the molecule levels rigidly, rather than by a self-consistent approach incorporating charge transfer between metal and molecule. Another explanation of this plateau (limitation of the gate voltage due to saturation of the charge in the electrochemical double layer) was ruled out by performing measurements in various different solutions (see Supporting Information).

Due to the ferromagnetic nature of the Ni electrodes, the spin degeneracy of the electron transport is lifted. Therefore, the transmission curves calculated for Ni junctions (Figure 4b) are separated into contributions from the minority and majority spin channels. Non-spin-polarized DFT-based calculations were also carried out but these did not reproduce the experimentally observed conductance. Unlike spin-polarized calculations, the non-spin-polarized calculations predict a large increase in the conductance of a Ni-44BP-Ni junction going from the tilted to the linear geometry (see Supporting Information), which is not observed experimentally (see Figure 2). This shows the importance of including spintronic effects when simulating single-molecule junctions with ferromagnetic contacts.

In Figure 4b, the transmission curves calculated for Ni-44BP-Ni junctions exhibit additional peaks close to the LUMO. These are due to the strong hybridization of the Ni d band with the LUMO of the molecule (see Supporting Information). For

the minority spin channel, ϵ_{F} lies on this peak which leads to a high transmission at ϵ_{F} and the experimentally observed increase in conductance between Ni-44BP-Ni and Au-44BP-Au junctions. The spin-split hybridization of the Ni d band with the LUMO of the molecule is similar to that recently reported for Ni-benzenedithiol-Ni single-molecule junctions.²² Note that for the majority channel, the peak due to the hybridization is much lower in energy and correspondingly contributes much less to the total transmission at ϵ_{F} . This is extremely important, because it implies that the current through the Ni-44BP-Ni junction is highly spin-polarized, in apparent contrast to Ni-benzenedithiol-Ni.²²

As the gate voltage applied to the Ni-44BP-Ni junctions is increased, ϵ_{F} is shifted closer to the LUMO and the hybridization of the LUMO with the Ni d band increases. As a result, the peak due to hybridization for the minority channel is enhanced and the conductance goes up. This gating mechanism is qualitatively different to that active in the case of Au contacts.

In summary, we have established that single-molecule junctions with oxide-free Ni contacts can be fabricated under electrochemical control. Our method could easily be extended to other base metals which are of interest as contacts for single-molecule devices. The Ni-44BP-Ni junctions show promise as single-molecule transistors, as they exhibit larger conductance and stronger gating than Au devices. Furthermore, DFT calculations strongly suggest that the current across the junction is highly spin-polarized due to spin-dependent hybridization of the Ni d band with the LUMO of 44BP. This indicates that Ni-44BP-Ni junctions are good candidates for single-molecule spintronic applications.

■ ASSOCIATED CONTENT

Supporting Information

Additional information on theoretical and experimental methods and supporting results and figures. This material is available free of charge via the Internet at <http://pubs.acs.org/>.

■ AUTHOR INFORMATION

Corresponding Authors

*E-mail: thygesen@fysik.dtu.dk.

*E-mail: w.schwarzacher@bristol.ac.uk.

Notes

The authors declare no competing financial interest.

■ ACKNOWLEDGMENTS

We thank Prof. Simon Higgins for useful discussions. W.S., R.J.B., and D.S.S. thank the U.K. Engineering and Physical Sciences Research Council (EPSRC) for financial support under grants EP/H002227/1 and EP/H001980/1, as well as the Bristol Centre for Nanoscience and Quantum Information for their support. W.S., R.J.B., and D.S.S. also thank Adrian Crimp and Josh Hugo for constructing equipment. K.S.T. and C.J. thank the Danish Council for Independent Research's Sapere Aude Program for financial support through Grant No. 11-1051390. The Center for Nanostructured Graphene is sponsored by the Danish National Research Foundation, Project DNR58.

■ REFERENCES

(1) Song, H.; Kim, Y.; Jang, Y. H.; Jeong, H.; Reed, M. A.; Lee, T. *Nature* **2009**, *462*, 1039–43.

- (2) Kay, N. J.; Higgins, S. J.; Jeppesen, J. O.; Leary, E.; Lycoops, J.; Ulstrup, J.; Nichols, R. J. *J. Am. Chem. Soc.* **2012**, *134*, 16817–26.
- (3) Xu, B.; Xiao, X.; Yang, X.; Zang, L.; Tao, N. *J. Am. Chem. Soc.* **2005**, *127*, 2386–7.
- (4) Haiss, W.; van Zalinge, H.; Higgins, S. J.; Bethell, D.; Höbenreich, H.; Schiffrin, D. J.; Nichols, R. J. *J. Am. Chem. Soc.* **2003**, *125*, 15294–5.
- (5) Li, C.; Mishchenko, A.; Wandlowski, T. *Top. Curr. Chem.* **2012**, *313*, 121–88.
- (6) Capozzi, B.; Chen, Q.; Darancet, P.; Kotiuga, M.; Buzzeo, M.; Neaton, J. B.; Nuckolls, C.; Venkataraman, L. *Nano Lett.* **2014**, *14*, 1400–4.
- (7) Lörtscher, E. *Nat. Nanotechnol.* **2013**, *8*, 381–4.
- (8) Quek, S. Y.; Kamenetska, M.; Steigerwald, M. L.; Choi, H. J.; Louie, S. G.; Hybertsen, M. S.; Neaton, J. B.; Venkataraman, L. *Nat. Nanotechnol.* **2009**, *4*, 230–4.
- (9) Kamenetska, M.; Quek, S. Y.; Whalley, A. C.; Steigerwald, M. L.; Choi, H. J.; Louie, S. G.; Nuckolls, C.; Hybertsen, M. S.; Neaton, J. B.; Venkataraman, L. *J. Am. Chem. Soc.* **2010**, *132*, 6817–21.
- (10) Kim, T.; Darancet, P.; Widawsky, J. R.; Kotiuga, M.; Quek, S. Y.; Neaton, J. B.; Venkataraman, L. *Nano Lett.* **2014**, *14*, 794–8.
- (11) Marqués-González, S.; Yufit, D. S.; Howard, J. A. K.; Martn, S.; Osorio, H. M.; Garca-Suárez, V. M.; Nichols, R. J.; Higgins, S. J.; Cea, P.; Low, P. J. *Dalton Trans.* **2013**, *42*, 338–41.
- (12) Hong, W.; Manrique, D. Z.; Moreno-Garca, P.; Gulcur, M.; Mishchenko, A.; Lambert, C. J.; Bryce, M. R.; Wandlowski, T. *J. Am. Chem. Soc.* **2012**, *134*, 2292–304.
- (13) Parameswaran, R.; Widawsky, J. R.; Vazquez, H.; Park, Y. S.; Boardman, B. M.; Nuckolls, C.; Steigerwald, M. L.; Hybertsen, M. S.; Venkataraman, L. *J. Phys. Chem. Lett.* **2010**, *1*, 2114–2119.
- (14) Arroyo, C. R.; Leary, E.; Castellanos-Gómez, A.; Rubio-Bollinger, G.; González, M. T.; Agrat, N. *J. Am. Chem. Soc.* **2011**, *133*, 14313–9.
- (15) Ie, Y.; Hirose, T.; Nakamura, H.; Kiguchi, M.; Takagi, N.; Kawai, M.; Aso, Y. *J. Am. Chem. Soc.* **2011**, *133*, 3014–22.
- (16) Mowbray, D. J.; Jones, G.; Thygesen, K. S. *J. Chem. Phys.* **2008**, *128*, 111103.
- (17) Park, Y. S.; Whalley, A. C.; Kamenetska, M.; Steigerwald, M. L.; Hybertsen, M. S.; Nuckolls, C.; Venkataraman, L. *J. Am. Chem. Soc.* **2007**, *129*, 15768–9.
- (18) Quek, S. Y.; Venkataraman, L.; Choi, H. J.; Louie, S. G.; Hybertsen, M. S.; Neaton, J. B. *Nano Lett.* **2007**, *7*, 3477–82.
- (19) Sanvito, S. *Nat. Phys.* **2010**, *6*, 562–564.
- (20) Rocha, A. R.; Garca-Suárez, V. M.; Bailey, S. W.; Lambert, C. J.; Ferrer, J.; Sanvito, S. *Nat. Mater.* **2005**, *4*, 335–9.
- (21) Kawahara, S. L.; Lagoute, J.; Repain, V.; Chacon, C.; Girard, Y.; Rousset, S.; Smogunov, A.; Barreateau, C. *Nano Lett.* **2012**, *12*, 4558–63.
- (22) Lee, S. K.; Ohto, T.; Yamada, R.; Tada, H. *Nano Lett.* **2014**, *14*, 5276–5280.
- (23) Xu, B.; Tao, N. *J. Science* **2003**, *301*, 1221–3.
- (24) Ghilane, J.; Hapiot, P.; Bard, A. J. *Anal. Chem.* **2006**, *78*, 6868–72.
- (25) Cavallini, M.; Biscarini, F. *Rev. Sci. Instrum.* **2000**, *71*, 4457.
- (26) Lopes, M.; Toury, T.; de La Chapelle, M. L.; Bonaccorso, F.; Gucciardi, P. G. *Rev. Sci. Instrum.* **2013**, *84*, 073702.
- (27) Suzuki, T.; Yamada, T.; Itaya, K. *J. Phys. Chem.* **1996**, *100*, 8954–8961.
- (28) Kiguchi, M.; Konishi, T.; Murakoshi, K. *Appl. Phys. Lett.* **2005**, *87*, 043104.
- (29) Kiguchi, M.; Konishi, T.; Miura, S.; Murakoshi, K. *Nanotechnology* **2007**, *18*, 424011.
- (30) Kim, T.; Vázquez, H.; Hybertsen, M. S.; Venkataraman, L. *Nano Lett.* **2013**, *13*, 3358–64.
- (31) Holze, R. In *Electrochemical Thermodynamics and Kinetics*; Lechner, M., Ed.; Landolt-Börnstein — Group IV Physical Chemistry; Springer: Berlin, 2007; Vol. 9A; pp 223–272.
- (32) Enkovaara, J.; Rostgaard, C.; Mortensen, J. J.; Chen, J.; Duak, M.; Ferrighi, L.; Gavnholt, J.; Glinsvad, C.; Haikola, V.; Hansen, H. A.;

Kristoffersen, H. H.; Kuisma, M.; Larsen, A. H.; Lehtovaara, L.; Ljungberg, M.; Lopez-Acevedo, O.; Moses, P. G.; Ojanen, J.; Olsen, T.; Petzold, V.; Romero, N. A.; Stausholm-Møller, J.; Strange, M.; Tritsaris, G. A.; Vanin, M.; Walter, M.; Hammer, B.; Häkkinen, H.; Madsen, G. K. H.; Nieminen, R. M.; Nørskov, J. K.; Puska, M.; Rantala, T. T.; Schiøtz, J.; Thygesen, K. S.; Jacobsen, K. W. *J. Phys.: Condens. Matter* **2010**, *22*, 253202.

(33) Meir, Y.; Wingreen, N. *Phys. Rev. Lett.* **1992**, *68*, 2512–2515.

(34) Strange, M.; Rostgaard, C.; Häkkinen, H.; Thygesen, K. S. *Phys. Rev. B: Condens. Matter Mater. Phys.* **2011**, *83*, 115108.

Paper IV**Dynamical image-charge effect in molecular tunnel junctions: Beyond energy level alignment**

C. Jin, K. S. Thygesen

Physical Review B **89**, 041102(R) (2014)

Dynamical image-charge effect in molecular tunnel junctions: Beyond energy level alignment

Chengjun Jin and Kristian S. Thygesen

Center for Atomic-scale Materials Design (CAMD), Department of Physics, Technical University of Denmark, DK-2800 Kgs. Lyngby, Denmark

(Received 11 October 2013; revised manuscript received 18 December 2013; published 6 January 2014)

When an electron tunnels between two metal contacts it temporarily induces an image charge (IC) in the electrodes which acts back on the tunneling electron. It is usually assumed that the IC forms instantaneously such that a static model for the image potential applies. Here we investigate how the finite IC formation time affects charge transport through a molecule suspended between two electrodes. For a single-level model, an analytical treatment shows that the conductance is suppressed by a factor Z^2 , where Z is the quasiparticle renormalization factor, compared to the static IC approximation. We show that Z can be expressed either in terms of the plasma frequency of the electrode or as the overlap between electrode wave functions corresponding to an empty and filled level, respectively. First-principles GW calculations for benzene-diamine connected to gold electrodes show that the dynamical corrections can reduce the conductance by more than a factor of two when compared to static GW or density functional theory where the molecular energy levels have been shifted to match the exact quasiparticle levels.

DOI: 10.1103/PhysRevB.89.041102

PACS number(s): 85.65.+h, 31.70.Dk, 71.10.-w, 73.20.-r

The effect of image forces on tunneling electrons was first studied by Sommerfeld and Bethe [1] and Holm [2] in the 1930s, and later refined by Simmons [3] to a form, which still today is widely used. In Simmons model, the effect of image forces is described by a simple $1/z$ correction to the tunneling barrier. Its range of validity has recently been critically examined on basis of *ab initio* calculations and experimental data for (sub-)nanometer-sized tunneling junctions [4–8].

Image charge (IC) forces also have important consequences for electron transport at metal-molecule interfaces because they influence the position of the molecular energy levels relative to the metal Fermi level [9–14]. Because the interaction with the image charge lowers the energy cost of adding an electron/hole to a molecular orbital, the occupied energy levels are shifted upwards, while the empty levels are shifted downwards in energy as the molecule approaches a metal surface.

Theoretically, the image forces are challenging to describe because they are created by the electron on which they act. To properly include such correlation effects one must go beyond standard single-particle theories like Hartree-Fock and density functional theory (DFT) [15,16]. For transport in molecular junctions, this has been done previously using the GW approximation to the electron self-energy both in the steady state [17–20] and time-dependent [21] regimes. Due to the computational complexity of such many-body methods, simple *ad hoc* correction schemes have been developed which shift the energy of the molecular orbitals by an amount estimated from a classical image charge model [22,23]. Such correction schemes, generally termed DFT + Σ , have been shown to improve the agreement with experiments compared to the uncorrected DFT result [24]. An interesting question is then whether such a level correction scheme captures all the effects of the IC on electron transport if the corrections are chosen to reproduce the exact level alignment for the frontier orbitals. It was recently shown that the IC not only influences the energy of the molecular orbitals but also their *spatial shape* [25]. A change in orbital shape will change the hybridization with the metal states and thereby affect the tunneling rate.

This effect is beyond the DFT + Σ schemes, but should be significant only for highly polarizable molecules.

Except for the few many-body calculations, all previous attempts to model the IC effect in molecular transport junctions have been based on the assumption that the IC forms instantaneously such that a static IC model applies. On the other hand, it is intuitively clear that the role of the IC depends on the time it takes to polarize the electrode compared to the time the electron spends on the molecule. The former is given roughly by the inverse plasmon frequency of the electrode, $\tau_p \approx 1/\omega_p$, while a simple expression for the latter follows from the time-energy uncertainty relation, $\tau_{\text{tun}} \approx \hbar/|E_F - \varepsilon_a|$, where ε_a is the energy of the molecular orbital closest to the Fermi level. We note that the related problem of how a finite plasmon frequency influences the spatial form of the image potential at a metal surface has been studied by several authors in the past [26–28].

In this Rapid Communication we show, using both a simple one-level model and first-principles many-body calculations, that the finite electrode response time always suppresses the conductance of a molecular junction compared to the result of a noninteracting model with the exact same level alignment (static IC approximation). Formally this is a consequence of the reduction of the quasiparticle weight of the molecular resonance from 1 to $Z < 1$ due to the electron-electron interactions which shift spectral weight from the single-particle excitation to other excitations (in particular plasmons). In the off-resonance tunneling regime, the conductance of the one-level model is suppressed by Z^2 compared to the static result. We provide two complementary physical explanations for this reduction. In a dynamical picture, it can be related to the ratio between the characteristic IC formation time τ_p and the dwell time of the electron on the molecule expressing the reduced screening of the electron due to the “lagging behind” of the IC. In a picture of hopping between many-body states, Z can be expressed as an overlap of the electrode wave function with and without the IC and thus explains the origin of the reduced tunneling rate as a mismatch between the initial and final states of the electrode. *Ab initio* GW calculations for benzene-diamine (BDA) connected to gold electrodes shows

a conductance reduction of almost a factor 3 compared to the static approximation (noninteracting transport through optimally tuned energy levels), demonstrating the importance of dynamical corrections for realistic systems.

We consider the problem of electron transport through a single electronic level $|a\rangle$ coupled to left (L) and right (R) electrodes. Due to the hopping matrix elements between $|a\rangle$ and the states of the electrodes, the level is broadened into a resonance with a finite spectral width γ , which we take to be energy independent for simplicity. We assume that the level is unoccupied, i.e., $\varepsilon_a > E_F + \gamma$, however, the case of an occupied level is treated completely analogously. The time-ordered Green's function of the localized level can be written

$$G_a(\omega) = \frac{1}{[\omega - \varepsilon_a - \text{Re} \Sigma_a(\omega)] + i[\gamma - \text{Im} \Sigma_a(\omega)]}, \quad (1)$$

where the self-energy $\Sigma_a(\omega) = \langle a | \hat{\Sigma}(\mathbf{r}, \mathbf{r}', \omega) | a \rangle$ accounts for the Coulomb interaction between electrons in the electrodes and an electron in $|a\rangle$. To lowest order in the interaction, the self-energy contains the Hartree and exchange potentials of Hartree-Fock theory. These terms do not contribute to the image charge effect and are therefore absorbed in ε_a . Thus Σ includes only the higher order terms (correlation effects).

The screening from the electrodes shifts the pole of the GF from ε_a to the quasiparticle (QP) energy

$$\varepsilon_a^{\text{QP}} = \varepsilon_a + \Delta\varepsilon_{\text{ic}}, \quad \Delta\varepsilon_{\text{ic}} = Z\Sigma_a(\varepsilon_a), \quad (2)$$

where $\Delta\varepsilon_{\text{ic}}$ denotes the image charge shift and $Z = [1 - d\Sigma_a(\varepsilon_a)/d\omega]^{-1}$ is the renormalization factor to be discussed later.

Within the GW approximation [29], the self-energy takes the form

$$\Sigma(\mathbf{r}, \mathbf{r}', \omega) = \frac{i}{2\pi} \int G_0(\mathbf{r}, \mathbf{r}', \omega + \omega') \bar{W}(\mathbf{r}, \mathbf{r}', \omega') d\omega', \quad (3)$$

where $\bar{W} = W - v$, and W is the dynamically screened Coulomb interaction. We have subtracted the bare Coulomb interaction $v = 1/|\mathbf{r} - \mathbf{r}'|$ from W to avoid double counting of the exchange energy which is already contained in ε_a . The unperturbed Green's function, is given by

$$G_0(\mathbf{r}, \mathbf{r}', \omega) = \frac{\psi_a(\mathbf{r})\psi_a(\mathbf{r}')^*}{\omega - \varepsilon_a + i\gamma} + \sum_k \frac{\psi_k(\mathbf{r})\psi_k(\mathbf{r}')^*}{\omega - \varepsilon_k + i0^+ \text{sgn}(\varepsilon_k - E_F)}. \quad (4)$$

In terms of the density response function of the metal electrode χ , we have (suppressing the integration over spatial variables) $\bar{W}(\omega) = v\chi(\omega)v$. Neglecting the spatial overlap between $|a\rangle$ and the metal states, the relevant matrix element of the screened interaction $\langle a | \bar{W}(\omega) | a \rangle$ becomes

$$\bar{W}_a(\omega) = \int \int V_a(\mathbf{r})\chi(\mathbf{r}, \mathbf{r}', \omega)V_a(\mathbf{r}')d\mathbf{r}d\mathbf{r}', \quad (5)$$

where $V_a(r)$ is the potential created by an electron in the state $|a\rangle$,

$$V_a(\mathbf{r}) = \int \frac{|\psi_a(\mathbf{r}')|^2}{|\mathbf{r} - \mathbf{r}'|} d\mathbf{r}'. \quad (6)$$

A Feynman diagram of the self-energy is shown in Fig. 1.

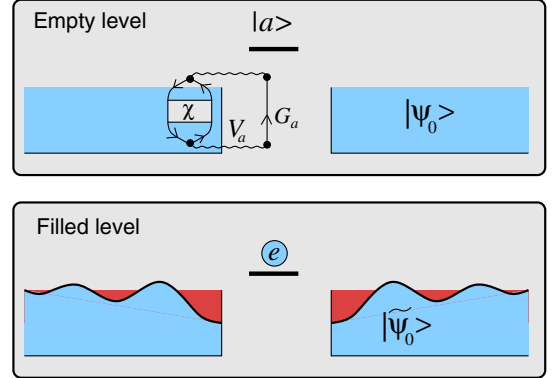


FIG. 1. (Color online) Upper panel: When the localized level $|a\rangle$ is empty, the charge distribution corresponding to the electrode ground state, $|\Psi_0\rangle$, is homogeneous (no image charge). Lower panel: When the level is occupied, the potential from the localized electron, $V_a(r)$, induces an image charge in the electrode ground state, $|\tilde{\Psi}_0\rangle$. A Feynman diagram for the self-energy describing the IC effect is shown in the upper panel.

Using a plasmon pole approximation (PPA) for the response function,

$$\bar{W}_a(\omega) = A \left(\frac{1}{\omega - \omega_p + i\gamma_p} - \frac{1}{\omega + \omega_p - i\gamma_p} \right), \quad (7)$$

the self-energy can be evaluated using complex contour integration

$$\Sigma_a(\omega) = \frac{A}{\omega - \varepsilon_a - \omega_p + i(\gamma + \gamma_p)}, \quad (8)$$

where ω_p and γ_p are the characteristic plasmon energy and spectral width, respectively. It follows that the imaginary part of Σ_a is a Lorentzian of width $\Gamma = \gamma + \gamma_p$ centered at $\omega_p + \varepsilon_a$. In the rest of the Rapid Communication we assume, for simplicity, that $\Gamma \ll \omega_p$. Since we are only interested in $\Sigma_a(\omega)$ in the range between E_F and ε_a , this means we can set $\Gamma = 0$ in Eq. (8). The constant A can be fixed by invoking the condition $\Delta\varepsilon_{\text{ic}} = Z\Sigma_a(\varepsilon_a)$, which results in

$$A = \frac{\Delta\varepsilon_{\text{ic}}\omega_p^2}{\omega_p - \Delta\varepsilon_{\text{ic}}}. \quad (9)$$

Close to equilibrium, i.e., for small bias voltages, the conductance is given by Landauer's formula $G = \frac{2e^2}{h}T(E_F)$ [30]. For the single-level model, the transmission at the Fermi level can be written

$$T(E_F) = \frac{\gamma^2}{(E_F - \varepsilon_a^{\text{eff}})^2 + \gamma^2}, \quad (10)$$

where we have defined the effective energy level seen by the tunneling electron as

$$\begin{aligned} \varepsilon_a^{\text{eff}} &= \varepsilon_a + \text{Re} \Sigma_a(E_F) \\ &= \varepsilon_a + \Delta\varepsilon_{\text{ic}} \left(\frac{\omega_p}{|E_F - \varepsilon_a| + \omega_p} \right). \end{aligned} \quad (11)$$

In the above expression we have assumed, for simplicity of the expression, that $\Delta\varepsilon_{ic} \ll \omega_p$. The transmission through the interacting level is thus equivalent to transmission through a noninteracting level with energy $\varepsilon_a^{\text{eff}}$. When the image charge formation is fast compared to the average time spent by the electron on the molecule, i.e., when $\omega_p \gg |E_F - \varepsilon_a|$, the effective level equals $\varepsilon_a^{\text{QP}}$ and the static image charge approximation is valid. In the opposite regime where the tunneling time is short compared with the image charge formation, i.e., $\omega_p \ll |E_F - \varepsilon_a|$, the self-energy vanishes and the tunneling electron “sees” the unscreened level ε_a .

In Eq. (10) we have embedded the effect of the finite electrode response time into an effective level position. Although this seems like a reasonable consequence of a partial image charge screening, it does not reflect the correct physics, since the pole of the Green’s function, and thus the spectral peak, remains at $\varepsilon_a^{\text{QP}}$. What is affected is the renormalization factor Z . Using Eqs. (8) and (9) it follows that

$$Z = 1 - \frac{\Delta\varepsilon_{ic}}{\omega_p}. \quad (12)$$

Within the quasiparticle approximation, one expands $\Sigma(\omega)$ to first order around ε_a which yields the transmission function

$$T^{\text{QP}}(\omega) = \frac{(Z\gamma)^2}{(\omega - \varepsilon_a^{\text{QP}})^2 + (Z\gamma)^2}. \quad (13)$$

This shows that the transmission resonance remains at $\varepsilon_a^{\text{QP}}$, but is narrowed by a factor of Z compared to the noninteracting result. In the off-resonant tunneling regime where $|E_F - \varepsilon_a^{\text{QP}}| \gg \gamma$ it follows that the conductance is suppressed by a factor Z^2 compared to the static approximation which sets $\Sigma_a(\omega) = \Delta\varepsilon_{ic}$.

The Green’s function formalism describes the propagation of one electron with the effect of all other electrons of the system embedded into the self-energy. Alternatively, one can describe the transport process in terms of transitions between many-body states with a different number of electrons on the level. For noninteracting electrons this involves only the hopping matrix elements between the state $|a\rangle$ and the single-particle states of the electrodes, $|k\rangle$. However, within such a picture we neglect the fact that all the other electrons in the electrode also feel a change in potential when the occupation of the localized level changes. To account for this effect, the single-particle transition matrix element must be multiplied by the overlap between the initial and final many-body states of the electrode, $\langle\Psi_0|\tilde{\Psi}_0\rangle$. The situation is sketched in Fig. 1.

Using first order perturbation theory to treat the effect of an electron on the molecule, the change in the electrode ground state becomes

$$|\Psi_0^{(1)}\rangle = \sum_{s \neq 0} \frac{\langle\Psi_s|\hat{V}|\Psi_0\rangle}{E_s - E_0} |\Psi_s\rangle, \quad (14)$$

where $\hat{V} = \int \hat{n}(r)V_a(r)dr$ with $V_a(r)$ defined in Eq. (6), is the operator describing the potential created by the electron on the level.

Using the Lehmann representation for the response function in Eq. (5), performing the integration in Eq. (3), and taking the

derivative at $\omega = \varepsilon_a$, one obtains

$$Z = \left(1 + \sum_{s \neq 0} \frac{|\langle\Psi_s|\hat{V}|\Psi_0\rangle|^2}{(E_s - E_0)^2}\right)^{-1}. \quad (15)$$

Noting that the *normalized* final state is $|\tilde{\Psi}_0\rangle = (|\Psi_0\rangle + |\Psi_0^{(1)}\rangle)/(1 + \langle\Psi_0^{(1)}|\Psi_0^{(1)}\rangle)^{1/2}$, and comparing with Eq. (14), it follows that

$$Z = |\langle\tilde{\Psi}_0|\Psi_0\rangle|^2. \quad (16)$$

In fact, this also follows from a more general result stating that Z is the squared norm of the QP state $|a\rangle$ (see, e.g., Ref. [25]). Equation (16) shows that the origin of the Z^2 conductance suppression expressed by Eq. (13) (at least in the cotunneling regime where $|E_F - \varepsilon_a^{\text{QP}}| \gg \gamma$), can be understood as a mismatch of the initial and final states of the electrodes. Here we note the similarity with the phenomenon known as Franck-Condon blockade where transport through a molecule is suppressed/blocked due to reduced overlap between the initial and final vibronic states of the molecule [31]. According to Eq. (16) the magnitude of Z is determined by the relative weight of the component $|\Psi_0^{(1)}\rangle$ in the final state $|\tilde{\Psi}_0\rangle$. We can relate the norm of $|\Psi_0^{(1)}\rangle$ to the response time of the electrode by noting that the terms in Eq. (14) have an $E_s - E_0$ denominator. Within the PPA the dominant terms come from the plasmon excitations for which $E_s - E_0 \approx \omega_p$. Thus a faster electrode response, i.e., larger ω_p , is equivalent to a smaller perturbation of the ground state and thus Z closer to unity. This is again consistent with Eq. (12).

To test the role of dynamical screening under more realistic conditions, we have performed first-principles GW calculations for the benchmark system of BDA connected to gold electrodes (see inset of Fig. 2). The details of the calculation follow Ref. [18]. In brief, the Green’s function of the contacted molecule is obtained by solving the Dyson equation self-consistently including both lead coupling self-energies and the GW self-energy. We use a basis of numerical atomic orbitals

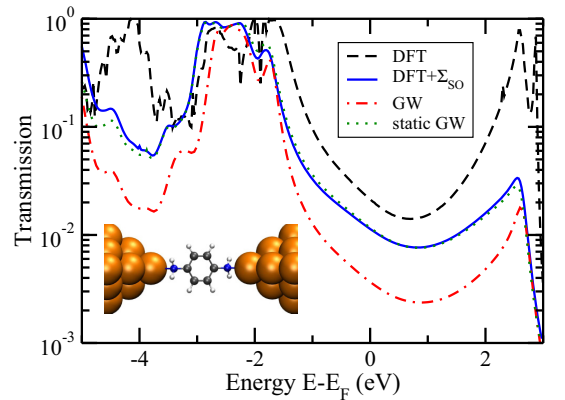


FIG. 2. (Color online) The transmission function of the gold/BDA junction calculated using four different methods (see text). For the static GW calculations we employed the xc potential of Eq. (18).

at the double- ζ plus polarization level for the gold electrodes and double- ζ for the BDA. The GW self-energy is evaluated in a spatial region containing the molecule and the four closest Au atoms on each side of the molecule. For the considered junction geometry this is sufficient because the IC is essentially confined to the tip Au atoms [18].

In Fig. 2 we show the transmission function calculated using four different methods. In addition to the GW result we show the transmission obtained from DFT with the standard Perdew-Burke-Ernzerhof exchange-correlation (xc) functional [32]. Not surprisingly the latter yields a higher conductance due to the well-known underestimation of the molecular energy gap. To isolate the role of dynamical effects we have used a “scissors operator” to adjust the energies of the molecular orbitals in the DFT calculation to those obtained with GW:

$$\Sigma_{\text{SO}} = \sum_{\nu \in \text{mol}} \Delta \varepsilon_{\nu} |\psi_{\nu}\rangle \langle \psi_{\nu}|. \quad (17)$$

The molecular orbitals $|\psi_{\nu}\rangle$ are obtained by diagonalizing the DFT Hamiltonian within the subspace spanned by the basis functions of the BDA. In practice, the energy shift ($\Delta \varepsilon_{\nu}$) of the three highest occupied and three lowest unoccupied orbitals are fitted to match the positions of the main peaks in the GW transmission spectrum. As a fourth method we followed the QPscGW scheme of Schilfgaard *et al.* to construct a static and Hermitian xc potential from the GW self-energy using the expression [33]

$$V^{\text{xc}} = \frac{1}{2} \sum_{\nu\mu \in \text{mol}} |\psi_{\nu}\rangle \text{Re}\{[\Sigma(\varepsilon_{\nu}^{\text{QP}})]_{\nu\mu} + [\Sigma(\varepsilon_{\mu}^{\text{QP}})]_{\nu\mu}\} \langle \psi_{\mu}| \quad (18)$$

with the QP energies $\varepsilon_{\nu}^{\text{QP}}$ obtained from the full GW calculation. As can be seen from Fig. 2, the QPscGW and DFT + Σ_{SO} methods yield very similar transmission spectra. This is because the off-diagonal matrix elements of V^{xc} from Eq. (18) are essentially zero, meaning that the DFT and QP molecular orbitals coincide. (This is not surprising given the low polarizability of BDA [25].) We thus conclude that the observed difference in transmission between full GW on the one hand and DFT + Σ_{SO} or QPscGW on the other hand, is neither due to differences in energy level alignment nor in the spatial shape of orbitals, but originates from the frequency dependence of the GW self-energy.

In Fig. 3 we show the Hartree-Fock (HF) and GW results for the spectral function of the BDA highest occupied molecular orbital (HOMO) together with the imaginary and real parts of the GW self-energy $\langle \psi_H | \hat{\Sigma}(\omega) | \psi_H \rangle$. From this it follows that the GW self-energy shifts the HOMO up in energy by 1.9 eV. The corresponding self-energy shift for BDA in the gas phase, caused by intramolecular screening, is found to be 1.0 eV. From this we conclude that the size of the IC shift, caused by the metallic screening, is 0.9 eV. It is clear from the almost linear behavior of $\text{Re } \Sigma(\omega)$, that the linear expansion of Σ leading to Eq. (13) is well justified. Furthermore, the

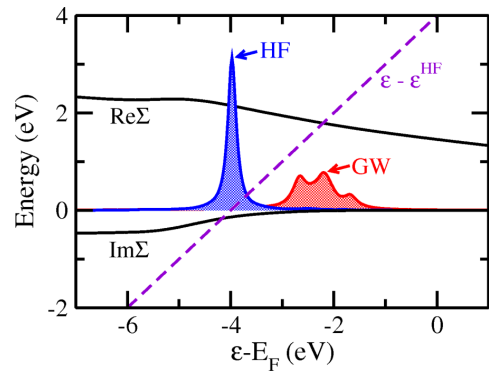


FIG. 3. (Color online) The spectral function of the HOMO of the contacted BDA molecule calculated with Hartree-Fock (blue) and GW (red). The real and imaginary parts of the GW self-energy are also shown (black curves).

imaginary part of the GW self-energy vanishes for energies above ε_H in agreement with the one-level model. The width of the spectral functions in Fig. 3 is given by the imaginary part of the coupling self-energy (not shown). The energy variation of this broadening follows the density of states at the gold tip atom. This explains the larger broadening of the GW resonance compared to the HF resonance which is situated below the gold d band.

From the slope of $\text{Re } \Sigma$ we obtain the renormalization factor of $Z = 0.84$. Based on the one-level model this should lead to a conductance suppression by a factor $Z^2 = 0.71$ which is, however, not sufficient to explain the observed difference between the GW and static GW result (see Fig. 2). The reason for this is that the BDA junction is not well described by a one-level model. While the unoccupied states play a minor role for the conductance, the HOMO-2, which is an antibonding version of the HOMO, must be included to obtain a realistic model. This points to a nontrivial interplay between the dynamical effects on different transport channels.

In conclusion, our results demonstrate that the role of electron-electron interactions in charge transport across a metal-molecule interface goes beyond the well-established effect on the energy level alignment. In general, the image charge dynamics renormalizes the level broadening (or equivalently the tunneling rate) by an amount that depends on the plasmon frequency of the electrode. Since the former can be tuned, e.g., by nanostructuring or electrostatic gating, this could provide a basis for experimental investigations of the dynamical image charge effect.

The authors acknowledge support from the Danish Council for Independent Research’s Sapere Aude Program through Grant No. 11-1051390.

[1] A. Sommerfeld and H. Bethe, *Handbüch der Physik*, Geiger und Scheel (Julius Springer-Verlag, Berlin, 1933), Vol. 24/2, p. 450.

[2] R. Holm and B. Kirschstein, *Z. Tech. Phys.* **16**, 488 (1935).

[3] J. G. Simmons, *J. Appl. Phys.* **34**, 1793 (1963).

- [4] E. H. Huisman, C. M. Guedon, B. J. van Wees, and S. J. van der Molen, *Nano Lett.* **9**, 3909 (2009).
- [5] M. L. Trouwborst, N. C. A. Martin, R. H. M. Smit, C. M. Guedon, T. A. Baart, S. J. van der Molen, and J. M. van Ruitenbeek, *Nano Lett.* **11**, 614 (2011).
- [6] K. L. Wu, M. L. Bai, S. Sanvito, and S. M. Hou, *Nanotechnology* **24**, 025203 (2013).
- [7] J. M. Beebe, B. S. Kim, J. W. Gadzuk, C. D. Frisbie, and J. G. Kushmerick, *Phys. Rev. Lett.* **97**, 026801 (2006).
- [8] J. Chen, T. Markussen, and K. S. Thygesen, *Phys. Rev. B* **82**, 121412 (2010).
- [9] J. Repp, G. Meyer, S. M. Stojkovic, A. Gourdon, and C. Joachim, *Phys. Rev. Lett.* **94**, 026803 (2005).
- [10] X. Lu, M. Grobis, K. H. Khoo, S. G. Louie, and M. F. Crommie, *Phys. Rev. B* **70**, 115418 (2004).
- [11] A. Kahn, N. Koch, and W. Gao, *J. Polym. Sci., B Polym. Phys.* **41**, 2529 (2003).
- [12] S. Kubatkin, A. Danilov, M. Hjort, J. Cornil, J.-L. Brédas, N. Stuhr-Hansen, Per Hedegård, and Thomas Bjørnholm, *Nature (London)* **425**, 698 (2003).
- [13] M. L. Perrin *et al.*, *Nat. Nanotechnol.* **8**, 282 (2013).
- [14] K. Kaasbjerg and K. Flensberg, *Nano Lett.* **8**, 3809 (2008).
- [15] J. B. Neaton, Mark S. Hybertsen, and Steven G. Louie, *Phys. Rev. Lett.* **97**, 216405 (2006).
- [16] J. M. Garcia-Lastra, C. Rostgaard, A. Rubio, and K. S. Thygesen, *Phys. Rev. B* **80**, 245427 (2009).
- [17] K. S. Thygesen and A. Rubio, *Phys. Rev. B* **77**, 115333 (2008).
- [18] M. Strange, C. Rostgaard, H. Hakkinen, and K. S. Thygesen, *Phys. Rev. B* **83**, 115108 (2011).
- [19] X. Wang, C. D. Spataru, M. S. Hybertsen, and A. J. Millis, *Phys. Rev. B* **77**, 045119 (2008).
- [20] T. Rangel, A. Ferretti, P. E. Trevisanutto, V. Olevano, and G. M. Rignanese, *Phys. Rev. B* **84**, 045426 (2011).
- [21] P. Myöhänen, R. Tuovinen, T. Korhonen, G. Stefanucci, and R. van Leeuwen, *Phys. Rev. B* **85**, 075105 (2012).
- [22] S. Y. Quek *et al.*, *Nano Lett.* **7**, 3477 (2007).
- [23] D. J. Mowbray, G. Jones, and K. S. Thygesen, *J. Chem. Phys.* **128**, 111103 (2008).
- [24] S. Y. Quek, H. J. Choi, S. G. Louie, and J. B. Neaton, *Nano Lett.* **9**, 3949 (2009).
- [25] M. Strange and K. S. Thygesen, *Phys. Rev. B* **86**, 195121 (2012).
- [26] R. Ray and G. D. Mahan, *Phys. Lett. A* **42**, 301 (1972).
- [27] M. Sunjic, G. Toulouse, and A. A. Lucas, *Solid State Commun.* **11**, 1629 (1972).
- [28] M. Jonson, *Solid State Commun.* **33**, 743 (1980).
- [29] L. Hedin, *Phys. Rev.* **139**, A796 (1965).
- [30] R. Landauer, *IBM J. Res. Dev.* **1**, 233 (1957).
- [31] J. Koch and F. von Oppen, *Phys. Rev. Lett.* **94**, 206804 (2005).
- [32] J. P. Perdew, K. Burke, and M. Ernzerhof, *Phys. Rev. Lett.* **77**, 3865 (1996).
- [33] M. van Schilfgaarde, T. Kotani, and S. Faleev, *Phys. Rev. Lett.* **96**, 226402 (2006).

Paper V**Simultaneous description of conductance and thermopower in single-molecule junctions from many-body ab initio calculations**

C. Jin, T. Markussen, K. S. Thygesen

Physical Review B **90**, 075115 (2014)

Simultaneous description of conductance and thermopower in single-molecule junctions from many-body *ab initio* calculations

Chengjun Jin, Troels Markussen, and Kristian S. Thygesen*

Center for Atomic-scale Materials Design, Department of Physics, Technical University of Denmark, DK-2800 Kgs. Lyngby, Denmark

(Received 28 June 2014; revised manuscript received 28 July 2014; published 11 August 2014)

We investigate the electronic conductance and thermopower of a single-molecule junction consisting of bis-(4-aminophenyl) acetylene (B4APA) connected to gold electrodes. We use nonequilibrium Green's function methods in combination with density-functional theory (DFT) and the many-body *GW* approximation. To simulate recent break junction experiments, we calculate the transport properties of the junction as it is pulled apart. For all junction configurations, DFT with a standard semilocal functional overestimates the conductance by almost an order of magnitude, while the thermopower is underestimated by up to a factor of 3, except for the most highly stretched junction configurations. In contrast, the *GW* results for both conductance and thermopower are in excellent agreement with experiments for a wide range of electrode separations. We show that the *GW* self-energy not only renormalizes the molecular energy levels but also the coupling strength. The latter is a consequence of the finite response time associated with the electronic screening in the metal electrodes.

DOI: [10.1103/PhysRevB.90.075115](https://doi.org/10.1103/PhysRevB.90.075115)

PACS number(s): 73.63.-b, 73.40.Gk, 85.65.+h

I. INTRODUCTION

Molecular junctions consisting of a single molecule connected to metallic electrodes via atomically well-defined chemical bonds represent unique benchmark systems for the study of charge, spin, and heat transport at the nanoscale [1]. Fascinating quantum phenomena such as giant magnetoresistance [2], Kondo effects [3,4], and quantum interference [5,6] have recently been reported for single-molecule junctions. Moreover, these systems allow for detailed studies of charge transfer and energy level alignment at metal-molecule interfaces of great relevance to, e.g., organic electronic devices and dye-sensitized solar cells [7–10].

As an addition to standard charge transport experiments, thermopower measurements have recently been advanced as a powerful spectroscopic tool for single-molecule junctions [11–16]. The thermopower is directly related to the slope of the transmission function at the Fermi level and thus can be used to infer the carrier type, i.e., whether transport is *n*- or *p*-type (semiconductor language) or whether the transport takes place via the highest occupied molecular orbital (HOMO) or the lowest unoccupied molecular orbital (LUMO) (chemical language).

Both the conductance and thermopower are highly sensitive to the position and width of the molecular resonances in the junction. This poses a challenge for *ab initio* modeling of single-molecule junctions since a proper description of the level alignment at metal-molecule interfaces is known to be highly problematic within the popular framework of density functional theory (DFT) [17,18]. While it is in principle possible to obtain the correct conductance or thermopower of a single-molecule junction from a calculation with an incorrect level alignment (i.e., obtain the correct result for the wrong reason), it is much less plausible that a simultaneously good description of conductance and thermopower can be achieved unless the energy level alignment and level broadening are

correctly described. Thus simultaneous modeling of the conductance and thermopower should represent a highly stringent test of the quality of the underlying electronic structure calculation.

Over the past decade, it has become clear that predictive and quantitatively accurate modeling of electronic energy level alignment and charge transport in metal-molecule junctions must be based on methods that go beyond the single-particle DFT description. The (self-consistent) *GW* approximation represents an accurate, although computationally demanding, alternative to DFT yielding quasiparticle (QP) energies in much better agreement with experiments. The improved description of the level positions is the main reason for the excellent agreement found between *GW* transport calculations and experiments on molecular junctions. However, in addition to the level alignment, the *GW* approximation accounts for two other effects, both of which are beyond the single-particle theories and which can have significant effects on the calculated transport properties. One is the change of the molecular wave functions arising from the interaction between the tunneling electron and its image charge in the electrode. This effect tends to contract the frontier orbitals toward the metal surface, and is stronger for molecules with large polarizability [19]. The second effect stems from the finite formation time of the image charge in the electrode represented roughly by the inverse of the plasmon frequency. This means that the image charge is “lacking behind” the tunneling electron and results in a reduction of the effective metal-molecule coupling strength [20]. Both of these effects are fully accounted for by the *GW* calculations presented in the present work, although only the latter is significant due to the relatively low polarizability of the bis-(4-aminophenyl) acetylene molecule (B4APA) studied here.

We have recently demonstrated that an excellent description of both the conductance and thermopower of benzenediamone (BDA) and benzenedicarbonitrile (BDCN) molecular junctions can be obtained using the *GW* method [21]. In contrast, standard DFT deviates from experiments by up to two orders of magnitude for these systems. Our previous work was based

*thygesen@fysik.dtu.dk

on a single (idealized) junction geometry, and the experimental data were taken from four independent experiments of conductance and thermopower for the two molecules, respectively. To establish a more faithful and consistent benchmarking of the GW approximation for electronic transport calculations, it is necessary to consider various junction geometries and preferentially compare to experiments where the conductance and thermopower were measured simultaneously. This is the motivation for the work reported in this paper.

Simultaneous measurements of conductance and thermopower of gold/B4APA were reported by Widawsky *et al.* [15]. The positive sign of the thermopower indicated that the electron transport through B4APA is hole-mediated, and this was supported by DFT-based transport calculations. It was shown that a correction of the DFT molecular energy levels was necessary in order to obtain a conductance and thermopower in agreement with experiments [15].

In this paper, we show that the conductance and thermopower of the gold/B4APA junction calculated with the GW approximation are in excellent agreement with the break junction experiments of Widawsky *et al.* Importantly, the good agreement is found for a wide range of stretching conditions. In contrast, DFT with a semilocal functional overestimates the conductance by a factor of 6 for all electrode separations while the thermopower is generally underestimated, except for very particular and highly stretched junction geometries. Secondly, we address the dynamical aspects of the image charge screening of the conductance and thermopower. Our calculations show that the finite response time of the electrode not only renormalizes the molecular energy levels, but also reduces the coupling strength between the molecule and the electrode. This effect reduces the conductance by almost a factor of 2 while the thermopower is essentially unaffected (in a one-level model, the thermopower is independent of the coupling strength).

II. METHODS

All the calculations were performed with the GPAW code [22] using the projector-augmented wave method. A bis-(4-aminophenyl) acetylene molecule (B4APA) is sandwiched between two Au tips attached to the Au(111) surface as illustrated in Fig. 1(a). The supercell contained eight 4×4 Au(111) atomic layers. The geometry of the molecule and Au tips was optimized until the residual force on every atom was below 0.02 eV/\AA . For the structure optimization, we used the Perdew-Burke-Ernzerhof (PBE) exchange-correlation (xc) functional [23], and the first Brillouin zone was sampled on a $4 \times 4 \times 1$ k -point mesh.

The DFT and GW transport calculations were performed following the method described in Refs. [24,25]. The transmission function was calculated from the Landauer formula [26,27]

$$\mathcal{T}(E) = \text{Tr}[G^r(E)\Gamma_L(E)G^a(E)\Gamma_R(E)], \quad (1)$$

where the retarded Green's function was obtained from

$$G^r(E) = [(E + i\eta)S - H_0 + V_{xc} - \Delta V_H[G] - \Sigma'_L(E) - \Sigma'_R(E) - \Sigma_{xc}[G](E)]^{-1}, \quad (2)$$

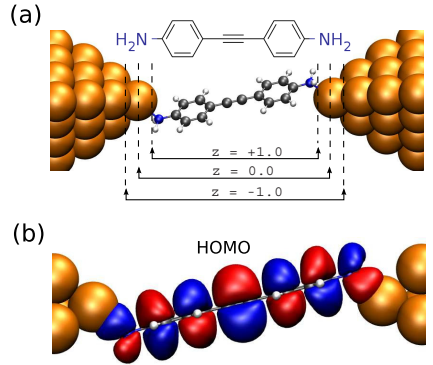


FIG. 1. (Color online) (a) A single bis-(4-aminophenyl) acetylene molecule (B4APA) is sandwiched between two Au tips attached to the Au(111) surface. The three different image plane positions used in the DFT+ Σ method are indicated, namely $z = +1.0, -1$ \AA relative to the Au tip atom. (b) Contour plot of the highest occupied molecular orbital (HOMO) of the B4APA molecule in the junction.

where S , H_0 , and V_{xc} are the overlap matrix, the Kohn-Sham Hamiltonian matrix, and the PBE xc potential in the atomic orbital basis [28], respectively. η is a numerical positive infinitesimal which is set to 0.02 eV in the calculations. $\Sigma'_{L/R}$ are the retarded lead self-energies and ΔV_H is the deviation of the Hartree potential from the equilibrium DFT-PBE value. Σ_{xc} is the many-body xc self-energy. For the HF and GW , Σ_{xc} is the nonlocal exchange potential and the GW self-energy, respectively. These self-energies are evaluated self-consistently. A standard non-equilibrium Green's function combined with density function theory (NEGF-DFT) calculation is recovered when Σ_{xc} is taken as the Kohn-Sham xc potential, V_{xc} . The self-consistent cycle is performed by a linear mixing of the Green functions. The energy-dependent quantities are represented on an energy grid ranging from -160 to 160 eV with an energy-grid spacing of 0.01 eV .

In the DFT+ Σ method [21,29,30], the DFT energy levels of the molecule in the junction are corrected by two terms. First, a correction is added to the occupied and unoccupied orbitals, respectively, to account for the self-interaction error in the DFT energy levels of the isolated molecule. These corrections are obtained for the isolated molecule as the difference between Kohn-Sham HOMO and LUMO eigenvalues and the ionization potential and electron affinity (obtained as total energy differences), respectively. Secondly, a classical image charge model is used to correct the energy levels for screening by the electrodes. Note that the classical image charge model is based on electrostatics and thus neglects any dynamical aspects of the screening process [20].

In the DFT+ Σ_{SO} calculations, the DFT energy levels of the molecule in the junction are corrected so as to match the QP energy levels obtained from the GW calculations by a scissor operator (SO):

$$\Sigma_{SO} = \sum_{\nu \rightarrow \text{mol}} \Delta \varepsilon_{\nu} |\psi_{\nu}\rangle \langle \psi_{\nu}|, \quad (3)$$

where the molecular orbitals $|\psi_i\rangle$ are obtained by diagonalizing the DFT Hamiltonian within the subspace spanned by the basis functions of the B4APA. This approach is presented in order to illustrate the effects of the GW self-energy that are beyond the level alignment correction. In this paper, we focus on the dynamical aspects of the screening, which are represented mathematically by the frequency dependence of the GW self-energy.

The transport calculations employ a double ζ with polarization (DZP) basis for all Au atoms, and a double- ζ (DZ) basis for the molecule. We use rather diffuse basis functions for Au corresponding to an energy shift of 0.01 eV. This is necessary to obtain a good description of the surface dipole, which is essential for a correct alignment of molecular energy levels. With the present basis set, we obtain a work function of 5.4 eV for the flat Au(111) surface, in good agreement with the experimental value of 5.3 eV [31].

The conductance and thermopower were calculated from

$$G = e^2 \mathcal{L}_0(E_F) \quad (4)$$

and

$$S = \frac{\mathcal{L}_1(E_F)}{eT\mathcal{L}_0(E_F)} = -\frac{\pi^2 k_B^2 T}{3e} \left. \frac{\partial \ln[\mathcal{T}(E)]}{\partial E} \right|_{E=E_F}. \quad (5)$$

Here $\mathcal{L}_m(\mu)$ is defined as

$$\mathcal{L}_m(\mu) = \frac{2}{h} \int_{-\infty}^{\infty} dE \mathcal{T}(E) (E - \mu)^m \left(-\frac{\partial f(E, \mu, T)}{\partial E} \right), \quad (6)$$

where $f(E, \mu, T)$ is the Fermi-Dirac distribution function. The last expression in S assumes that the transmission is slowly varying around E_F [11]. T is the average temperature of the left and right electrodes. We note that the thermopower in Eq. (5) is defined within linear response, and is thus applicable when $\Delta T/T$ is small. The nonlinear effects are expected to be of minor importance, since the experiments were done with $T \approx 300$ K and $|\Delta T| < 30$ K. Moreover, the measured thermoelectric current is linearly dependent with small ΔT in the experiments, indicating that the linear response formula is adequate.

III. RESULTS AND DISCUSSION

A. Break junction simulation

To mimic the experimental break junction setup, we stretch the molecular junction by displacing the two Au electrodes in steps of 0.25 Å. The junction is optimized at each displacement step. Figure 2(a) shows the change of the total energy as the junction is stretched. The minimum energy is reached around the configuration S_0 , which represents the zero-stress configuration in the experiments. As shown in Figs. 2(b) and 2(c), the Au-N bond length varies from 2.4 to 2.8 Å, while the angle $\alpha_{\text{Au-N-C}}$ between the Au-N-C atoms changes from 120° to 135°.

The evolution of the conductance and thermopower calculated from DFT and GW is shown in Figs. 2(d) and 2(e), respectively. The DFT conductance remains almost constant, except for the highly stretched configurations. Comparing the DFT conductances with the statistically most probable

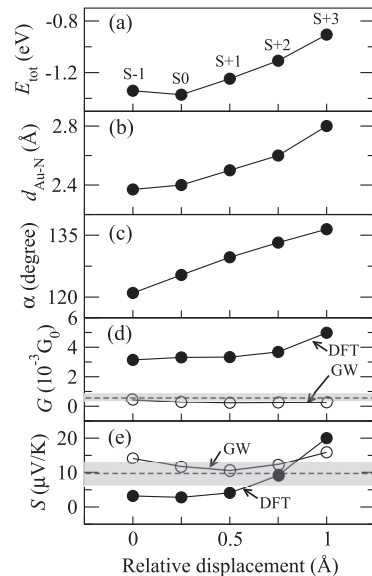


FIG. 2. The effect of stretching the Au/B4APA junction on (a) the total energy, (b) the Au-N bond length $d_{\text{Au-N}}$, (c) the angle $\alpha_{\text{Au-N-C}}$ between the Au-N-C atoms, (d) the conductance, and (e) the thermopower. The statistically most likely conductance 0.57 ± 0.2 ($10^{-3} G_0$) and thermopower 9.7 ± 3 ($\mu\text{V/K}$) from the break junction experiment are indicated by the gray bars [15]. Each configuration is labeled by $S - 1$ to $S + 3$ as shown in (a). The relative displacement is scaled to the configuration $S - 1$.

experimental conductance indicated by the gray bar, it is clear that the factor of 6 discrepancy cannot be explained by the junction geometry (stretching). For the zero-stress configuration S_0 , the DFT thermopower of 2.8 $\mu\text{V/K}$ is a factor of 3 smaller than the experimental thermopower indicated by the gray bar. The DFT thermopower increases up to 20 $\mu\text{V/K}$ from the configuration S_0 to the configuration $S + 3$. We note that although the DFT thermopower of the configuration $S + 2$ is very close to the experimental value, this configuration is considered unlikely in the statistical break junction experiment. Moreover, the DFT conductance of the configuration $S + 2$ is a factor of 6 larger than the experimental value. We thus conclude that the large deviation of both the DFT conductance and thermopower from the experimental values cannot be explained to arise from variations in the junction structure.

In contrast to the DFT calculations, the conductance obtained from GW is close to the experimental conductance over a large range of electrode separations. Moreover, the GW thermopower is in overall good agreement with the experimental values, in particular for the low stress configurations.

The variation of the DFT conductance and thermopower during the stretching simulation can be explained by the variation in the HOMO and LUMO positions with respect to the Fermi level. The transmission functions calculated from DFT for the configuration S_0 to the configuration $S + 3$ are shown in Fig. 3. Because the HOMO couples directly to the

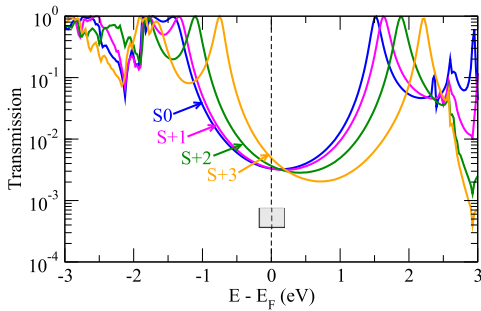


FIG. 3. (Color online) Transmission functions calculated from DFT for the configuration $S0$ to the configurations $S + 3$. The gray box indicates the experimental conductance $0.57 \pm 0.2 (10^{-3}G_0)$, and the Fermi level indicated by the dashed line is set to 0 eV [15].

electrodes shown in Fig. 1(b), the coupling strength is reduced when stretching the junction. On the one hand, the reduction of the coupling narrows the HOMO spectral peak from 0.09 to 0.05 eV, fitted from Fig. 3. On the other hand, the charge transfer from the N lone pair to the undercoordinated Au tip atom decreases upon stretching. This effect lowers the magnitude of the local dipole field and shifts the potential on the molecule and thus the molecular energy levels upward in energy.

As the DFT energies of the HOMO and LUMO resonances do not overlap with the characteristic features in the local density of states of the Au $5d$ states around -2 and 2.5 eV, we quantify the change in conductance and thermopower using a simple Lorentzian model [32]. In the case in which the HOMO clearly mediates the transport around E_F , we have

$$\mathcal{T}(E) = \frac{\Gamma^2}{(E - \varepsilon_H)^2 + \Gamma^2} \quad (7)$$

and the thermopower is

$$S_H = -\frac{\pi^2 k_B^2 T}{3e} \frac{2\varepsilon_H}{\varepsilon_H^2 + \Gamma^2} \approx -\frac{\pi^2 k_B^2 T}{3e} \frac{2}{\varepsilon_H}. \quad (8)$$

Here Γ is the energy-independent tunneling width and ε_H is the HOMO energy. The last expression assumes that $\varepsilon_H \gg \Gamma$, which is indeed the case as $\varepsilon_H \approx -1$ eV and $\Gamma \approx 0.1$ eV. The thermopower is thus seen to be independent of Γ . This is contrary to the conductance, which approximately is $\mathcal{G} \approx \Gamma^2/\varepsilon_H^2 G_0$, and thus is sensitive to variations in Γ . When stretching the junction, Γ is reduced while the HOMO level moves toward E_F leading to the almost constant conductance seen in Fig. 2(d).

In the case in which both the HOMO and LUMO contribute to the transport, the thermopower is approximately

$$S_{H+L} \approx -\frac{\pi^2 k_B^2 T}{3e} \left(\frac{2}{\varepsilon_H} + \frac{2}{\varepsilon_L} \right). \quad (9)$$

In the DFT calculations, the low thermopower values are simply due to the fact that the Fermi energy is approximately midway between the HOMO and LUMO energies, i.e., $\varepsilon_H \approx -\varepsilon_L$. For the stretched configuration $S + 3$, all the molecular levels are shifted up in energy, and the HOMO is clearly dominating the transport resulting in a higher thermopower.

TABLE I. The HOMO and LUMO energies of the B4APA molecule in the gas phase and in the junction, respectively, calculated from DFT-PBE Kohn-Sham eigenvalues (PBE-eig), GW , HF, and DFT-PBE total energy differences (PBE-tot). Units are eV.

Molecule	Orbital	PBE-eig	GW	HF	PBE-tot
Gas phase	HOMO	-4.4	-5.9	-6.9	-6.3
	LUMO	-1.6	1.2	2.5	0.4
	H-L gap	2.8	7.1	9.4	6.7
Junction	HOMO	-1.4	-2.1	-3.3	N/A
	LUMO	1.5	4.5	6.2	N/A
	H-L gap	2.9	6.6	9.5	N/A

B. Energy levels of molecule in the gas phase

Before investigating the level alignment in the junction, we consider the energy levels in the gas phase. In Table I, the HOMO and LUMO levels in the gas phase are calculated from the PBE Kohn-Sham eigenvalues (PBE-eig), GW , HF, and PBE total energy differences between the neutral and charged molecule (PBE-tot). We have not been able to find experimental data for the ionization potentials or electron affinities of the B4APA. Instead we use PBE total energy differences as a reference, as this approach was found to have an accuracy of around 0.2 eV for the ionization potential of small molecules [33]. Several benchmark studies have established that the accuracy of self-consistent GW for the frontier orbitals of small to intermediate size molecules is 0.3–0.4 eV [33,34].

For the B4APA, the DFT HOMO level is overestimated by 1.9 eV while the DFT LUMO is underestimated by 2.0 eV compared to the PBE-tot. The DFT HOMO-LUMO gap is therefore underestimated by 3.9 eV. These errors are mainly due to the self-interaction errors in the DFT-PBE functional. By using the self-interaction free HF, the gap is opened up to 9.4 eV, which is about 2.7 eV larger than the PBE-tot value. The inclusion of correlation effects at the GW level reduces the HF gap to 7.1 eV, in reasonable agreement with the PBE-tot value of 6.7 eV. In line with the general tendency of self-consistent GW to underestimate molecular ionization potentials [33,34], we find that the HOMO level from the GW calculation lies 0.4 eV above the PBE-tot value.

C. GW transport calculations

In Fig. 4, we compare the transmission functions obtained from DFT, GW , and HF for the zero-stress configuration $S0$. In all calculations, the Fermi level is crossing the tail of the HOMO level signaling a HOMO mediated tunneling process. The transmission features around -2 and 2.5 eV are characteristic features of the local density of states of the Au tip atom. Since the Au atoms are described at the DFT level in all the methods (the self-energy corrections are added only on the molecular subspace), these features are present in all three transmission curves.

The conductances obtained from DFT, GW , and HF are listed in Table II. While DFT (HF) overestimates (underestimates) the conductance by a factor of 6 (26), GW brings the conductance in agreement with the experimental value.

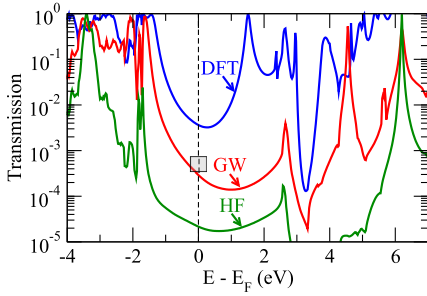


FIG. 4. (Color online) Transmission functions for the zero-stress Au/B4APA junction configuration (S0) calculated from DFT-PBE, GW, and HF. The gray box indicates the experimental conductance $0.57 \pm 0.2 (10^{-3} G_0)$, and the Fermi level indicated by the dashed line is set to zero eV [15].

This is a direct result of the more accurate level alignment with respect to the Au Fermi energy. The HOMO and LUMO levels in the junction are listed in the Table I. Due to hybridization, the HOMO-LUMO (H-L) gap in both the DFT and HF calculations is increased by 0.1 eV compared to the gas-phase results. However the H-L gap from GW is reduced by 0.5 eV. This reduction of the H-L gap is a consequence of the image charge effect, which is absent in both DFT and HF [17,18].

The thermopowers obtained from DFT, GW, and HF are also shown in Table II. While both DFT and HF underestimate the experimental value by a factor of 3 and 2, respectively, the GW thermopower is in excellent agreement with the experimental value. As noted earlier, the low thermopower obtained from DFT is a consequence of the fact that the Fermi level is positioned in the middle of the HOMO-LUMO gap; see Eq. (9).

D. Dynamical screening

To isolate the role of dynamical effects, we have used a scissors operator to adjust the energies of the molecular orbitals in the DFT calculation to those obtained from GW, see Sec. II. In practice, the energy shifts ($\Delta\varepsilon_v$) of the lowest three unoccupied and highest three occupied molecular orbitals are fitted to match the main peaks in the GW transmission spectrum.

In Fig. 5(a), we compare the transmission functions calculated with GW and DFT+ Σ_{SO} . It is seen that the full GW transmission is suppressed inside the HOMO-LUMO gap compared to the level matched DFT+ Σ_{SO} transmission. At the

TABLE II. Conductance and thermopower for the zero-stress Au/B4APA junction configuration (S0) calculated from DFT-PBE, GW, and HF. The experimental values are listed in the last column [15].

	DFT-PBE	GW	HF	Expt.
$\mathcal{G} (10^{-3} G_0)$	3.31	0.29	0.022	0.57 ± 0.2
$\mathcal{S} (\mu\text{V}/\text{K})$	2.8	11.6	5.4	9.7 ± 0.3

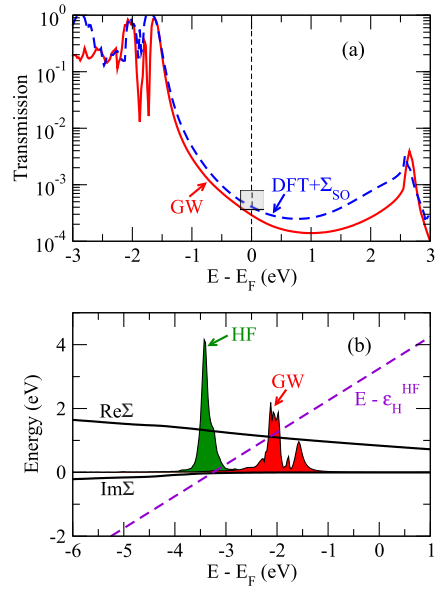


FIG. 5. (Color online) (a) Transmission functions calculated from GW and DFT+ Σ_{SO} for the zero-stress Au/B4APA junction configuration (S0). In the DFT+ Σ_{SO} method, the DFT molecular levels are rigidly shifted to match the GW levels. The gray box indicates the experimental conductance $0.57 \pm 0.2 (10^{-3} G_0)$, and the Fermi level indicated by the dashed line is set to 0 eV [15]. (b) The spectral function of the HOMO of the contacted molecule calculated from HF and GW. The real and imaginary parts of the GW self-energy are also shown as black curves.

Fermi level, the GW transmission is a factor of 0.73 lower than the DFT+ Σ_{SO} transmission, while the thermopower from the two methods is essentially identical. The reduction of the GW transmission is related to the quasiparticle renormalization factor of the HOMO level, $Z = [1 - d \text{Re} \Sigma_H(\varepsilon_H)/dE]^{-1}$. The real part of $\langle \psi_H | \Sigma(E) | \psi_H \rangle$ is shown in Fig. 5(b). The renormalization factor Z describes how well the many-body state representing the molecule with one electron removed from the HOMO can be described as a single particle removed from the neutral ground state. Since the removal of an electron from the molecule will couple to electronic excitations in the electrode via the Coulomb interaction, the stationary states representing the ionized molecule in the junction will contain components where the electrode is in an excited state. For a metal, it is usually valid to describe the response to external fields by a single effective excitation (plasmon pole approximation). The coupling to the plasmon excitation reduces the spectral weight of the HOMO peak, leading to a renormalization factor Z less than unity. For a more detailed discussion of these issues, we refer the reader to Ref. [20].

In the presence of a self-energy, Σ , describing electron-electron interactions, the transmission through a single electronic level coupled to wide band leads can be

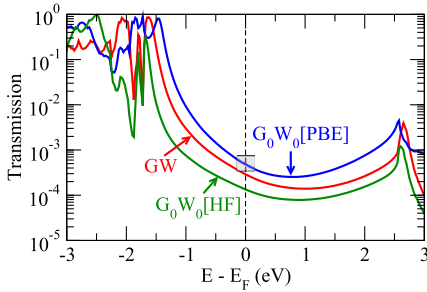


FIG. 6. (Color online) Transmission functions for the zero-stress Au/B4APA junction configuration (S_0) calculated from G_0W_0 (PBE), self-consistent GW , and G_0W_0 (HF). The gray box indicates the experimental conductance 0.57 ± 0.2 ($10^{-3}G_0$), and the Fermi level indicated by the dashed line is set to 0 eV [15].

written

$$\mathcal{T}^{\text{QP}}(E) = \frac{(Z\Gamma)^2}{(E - \varepsilon_a^{\text{QP}})^2 + (Z\Gamma)^2}, \quad (10)$$

where Γ is the (energy-independent) tunneling width and Z is the renormalization factor, and $\varepsilon_a^{\text{QP}}$ is the QP energy level representing the pole of the interacting Green's function. In the off-resonance tunneling regime ($|E - \varepsilon_a^{\text{QP}}| \gg \Gamma$), the conductance becomes

$$G^{\text{QP}} \approx \frac{(Z\Gamma)^2}{\varepsilon_a^{\text{QP}2}} G_0, \quad (11)$$

which is suppressed by a factor of Z^2 from the level matched noninteracting result. For the HOMO level of 4BAPA in the junction, we find $Z^2 = 0.74$, which agrees almost exactly with the ratio between the conductance obtained from GW and DFT+ Σ_{S_0} .

For the one-level model in the off-resonance regime, the thermopower becomes

$$S^{\text{QP}} \approx -\frac{\pi^2 k_B^2 T}{3e} \frac{2}{\varepsilon_a^{\text{QP}}}, \quad (12)$$

i.e., independent of Z . This is again consistent with the fact that we find essentially the same thermopower with GW and DFT+ Σ_{S_0} .

E. One-shot G_0W_0 calculations

To examine the role of self-consistency in the GW calculations, we have performed one-shot G_0W_0 calculations using

TABLE III. The conductance and thermopower for the zero-stress Au/B4APA junction configuration (S_0) calculated using G_0W_0 (PBE), GW , and G_0W_0 (HF). The experimental values are listed in the last column [15].

	G_0W_0 (PBE)	GW	G_0W_0 (HF)	Expt.
G ($10^{-3}G_0$)	0.48	0.29	0.13	0.57 ± 0.2
S ($\mu\text{V}/\text{K}$)	12.9	11.6	9.3	9.7 ± 0.3

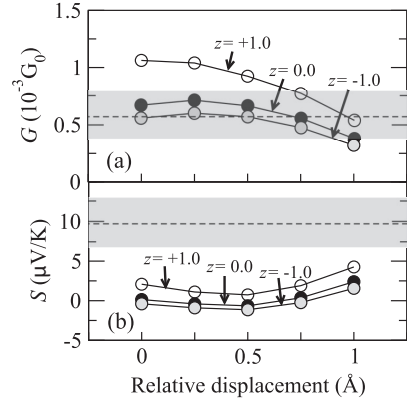


FIG. 7. The effect of stretching the Au/B4APA junction on (a) the conductance and (b) the thermopower, calculated from the DFT+ Σ method using three different image plane positions, namely $z = +1.0, -1$ Å relative to the Au tip atom. The statistically most likely conductance 0.57 ± 0.2 ($10^{-3}G_0$) and thermopower 9.7 ± 3 ($\mu\text{V}/\text{K}$) from the break junction experiment are indicated by the gray bars [15]. The relative displacement is scaled to the configuration $S - 1$.

either DFT-PBE or HF as starting point. The transmission functions obtained from the one-shot G_0W_0 (PBE) and G_0W_0 (HF) calculations are shown in Fig. 6 and the conductances and thermopowers are listed in Table III. Compared to GW , G_0W_0 (PBE) overestimates both the conductance and thermopower while G_0W_0 (HF) underestimates both quantities. These trends can be explained by noting that using DFT-PBE and HF as initial G_0 , respectively, overestimates and underestimates the effect of screening (compared to self-consistent GW , which yield energy gaps in between DFT-PBE and HF). As a consequence, the HOMO level is higher with G_0W_0 (PBE) and lower with G_0W_0 (HF). The change in both the conductance and thermopower then follows directly from Eqs. (11) and (12).

F. DFT+ Σ calculations

Finally, the effect of stretching the Au/B4APA junction on the conductance and thermopower is addressed by using the DFT+ Σ method, as shown in Fig. 7. We have employed three different image plane positions, namely $z = +1.0, -1$ Å relative to the Au tip atom. While the conductances are greatly improved over the uncorrected DFT results, the thermopowers

TABLE IV. Conductance and thermopower for the zero-stress Au/B4APA junction configuration (S_0) calculated using the DFT+ Σ method with three different image plane positions, namely $z = +1.0, -1$ relative to the Au tip atom. The experimental values are listed in the last column [15].

	+1 Å	0 Å	-1 Å	Expt.
G ($10^{-3}G_0$)	1.04	0.71	0.60	0.57 ± 0.2
S ($\mu\text{V}/\text{K}$)	1.1	-0.4	-0.9	9.7 ± 0.3

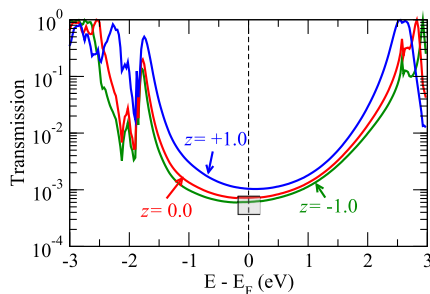


FIG. 8. (Color online) The transmission function for the zero-stress Au/B4APA junction configuration ($S0$) calculated from the DFT+ Σ method using three different image plane positions, namely $z = +1, 0, -1$ Å relative to the Au tip atom. The gray box indicates the experimental conductance 0.57 ± 0.2 ($10^{-3}G_0$), and the Fermi level indicated by the dashed line is set to 0 eV [15].

are not improved; in fact they are worsened (see Table IV for the zero-stress configuration).

Contrary to the DFT calculations, where the conductance remains almost constant during the stretching, the conductances are decreased in the DFT+ Σ calculations. This is because the image charge effect is reduced when the molecule is moving away from the electrode. As noted earlier, the low thermopowers close to zero are a consequence of the highly symmetric position of the HOMO and LUMO peaks with respect to E_F (see the transmission functions of the zero-stress configuration in Fig. 8).

We note that the DFT + Σ calculations presented in Ref. [15] show an improvement of DFT and a good agreement

with the experimental values for both conductance and thermopower. However our configuration $S + 3$ reproduces the DFT and DFT + Σ results reported in Ref. [15], indicating that those calculations were performed for a stretched junction configuration.

IV. CONCLUSIONS

In conclusion, we have demonstrated that the (self-consistent) GW approximation to the electron self-energy provides a quantitatively accurate description of both conductance and thermopower in a gold/bis-(4-aminophenyl) acetylene single-molecule junction. By performing calculations as the junction is pulled apart, it was shown that while the GW approximation yields good agreement with experimental break junction experiments for a large range of electrode separations, the standard DFT description overestimates conductance and underestimates thermopower for all but the most stretched junction geometries. The main reason for the improved GW description is a better level alignment. However, it was also found that the frequency dependence of the GW self-energy, which accounts for the dynamics of the image charge screening, can have a significant impact on the conductance by reducing the effective metal-molecule coupling strength.

ACKNOWLEDGMENT

The authors acknowledge support from the Danish Council for Independent Research, **FTP Sapere Aude** Grant No. 11-1051390.

- [1] S. V. Aradhya and L. Venkataraman, *Nat. Nano.* **8**, 399 (2013).
- [2] S. Schmaus, A. Bagrets, Y. Nahas, T. K. Yamada, A. Bork, M. Bowen, E. Beaurepaire, F. Evers, and W. Wulfhekkel, *Nat. Nano.* **6**, 185 (2011).
- [3] J. Park, A. N. Pasupathy, J. I. Goldsmith, C. Chang, Y. Yaish, J. R. Petta, M. Rinkoski, J. P. Sethna, H. D. Abruna, P. L. McEuen *et al.*, *Nature (London)* **417**, 722 (2002).
- [4] W. Liang, M. P. Shores, M. Bockrath, J. R. Long, and H. Park, *Nature (London)* **417**, 725 (2002).
- [5] P. Sautet and C. Joachim, *Chem. Phys. Lett.* **153**, 511 (1988).
- [6] C. M. Guedon, H. Valkenier, T. Markussen, K. S. Thygesen, J. C. Hummelen, and S. J. van der Molen, *Nat. Nanotech.* **7**, 305 (2012).
- [7] B. O'Regan and M. Grätzel, *Nature (London)* **353**, 737 (1991).
- [8] M. Grätzel, *Nature (London)* **414**, 338 (2001).
- [9] J.-L. Brdas, J. E. Norton, J. Cornil, and V. Coropceanu, *Acc. Chem. Res.* **42**, 1691 (2009).
- [10] K. B. Ørnsø, J. M. Garcia-Lastra, and K. S. Thygesen, *Phys. Chem. Chem. Phys.* **15**, 19478 (2013).
- [11] M. Paulsson and S. Datta, *Phys. Rev. B* **67**, 241403 (2003).
- [12] P. Reddy, S.-Y. Jang, R. A. Segalman, and A. Majumdar, *Science* **315**, 1568 (2007).
- [13] K. Baheti, J. A. Malen, P. Doak, P. Reddy, S.-Y. Jang, T. D. Tilley, A. Majumdar, and R. A. Segalman, *Nano Lett.* **8**, 715 (2008).
- [14] J. A. Malen, P. Doak, K. Baheti, T. D. Tilley, R. A. Segalman, and A. Majumdar, *Nano Lett.* **9**, 1164 (2009).
- [15] J. R. Widawsky, P. Darancet, J. B. Neaton, and L. Venkataraman, *Nano Lett.* **12**, 354 (2012).
- [16] W. Lee, K. Kim, W. Jeong, L. A. Zotti, F. Pauly, J. C. Cuevas, and P. Reddy, *Nature (London)* **498**, 209 (2013).
- [17] J. B. Neaton, M. S. Hybertsen, and S. G. Louie, *Phys. Rev. Lett.* **97**, 216405 (2006).
- [18] J. M. Garcia-Lastra, C. Rostgaard, A. Rubio, and K. S. Thygesen, *Phys. Rev. B* **80**, 245427 (2009).
- [19] M. Strange and K. S. Thygesen, *Phys. Rev. B* **86**, 195121 (2012).
- [20] C. Jin and K. S. Thygesen, *Phys. Rev. B* **89**, 041102 (2014).
- [21] T. Markussen, C. Jin, and K. S. Thygesen, *Physica Status Solidi B* **250**, 2394 (2013).
- [22] J. Enkovaara, C. Rostgaard, J. J. Mortensen, J. Chen, M. Duak, L. Ferrighi, J. Gavnholt, C. Glinsvad, V. Haikola, H. A. Hansen *et al.*, *J. Phys.: Condens. Matter* **22**, 253202 (2010).
- [23] J. P. Perdew, K. Burke, and M. Ernzerhof, *Phys. Rev. Lett.* **77**, 3865 (1996).
- [24] M. Strange, C. Rostgaard, H. Häkkinen, and K. S. Thygesen, *Phys. Rev. B* **83**, 115108 (2011).
- [25] K. S. Thygesen and A. Rubio, *Phys. Rev. B* **77**, 115333 (2008).
- [26] Y. Meir and N. S. Wingreen, *Phys. Rev. Lett.* **68**, 2512 (1992).
- [27] K. S. Thygesen, *Phys. Rev. B* **73**, 035309 (2006).

- [28] A. H. Larsen, M. Vanin, J. J. Mortensen, K. S. Thygesen, and K. W. Jacobsen, *Phys. Rev. B* **80**, 195112 (2009).
- [29] D. J. Mowbray, G. Jones, and K. S. Thygesen, *J. Chem. Phys.* **128**, 111103 (2008).
- [30] S. Y. Quek, L. Venkataraman, H. J. Choi, S. G. Louie, M. S. Hybertsen, and J. B. Neaton, *Nano Lett.* **7**, 3477 (2007).
- [31] H. B. Michaelson, *J. Appl. Phys.* **48**, 4729 (1977).
- [32] T. Kim, P. Darancet, J. R. Widawsky, M. Kotiuga, S. Y. Quek, J. B. Neaton, and L. Venkataraman, *Nano Lett.* **14**, 794 (2014).
- [33] C. Rostgaard, K. W. Jacobsen, and K. S. Thygesen, *Phys. Rev. B* **81**, 085103 (2010).
- [34] X. Blase, C. Attaccalite, and V. Olevano, *Phys. Rev. B* **83**, 115103 (2011).